Improving Global Tide and Storm Surge Forecasts with Parameter Estimation

Wang, X.

DOI
10.4233/uuid:5f26edc8-f50c-4302-8142-4cf78ff73902

Publication date
2022

Document Version
Final published version

Citation (APA)
Wang, X. (2022). *Improving Global Tide and Storm Surge Forecasts with Parameter Estimation*. [Dissertation (TU Delft), Delft University of Technology]. https://doi.org/10.4233/uuid:5f26edc8-f50c-4302-8142-4cf78ff73902

Important note
To cite this publication, please use the final published version (if applicable).
Please check the document version above.

Improving Global Tide and Storm Surge Forecasts with Parameter Estimation

Xiaohui Wang

Improving Global Tide and Storm Surge Forecasts with Parameter Estimation

Improving Global Tide and Storm Surge Forecasts with Parameter Estimation

Dissertation

for the purpose of obtaining the degree of doctor
at Delft University of Technology,
by the authority of the Rector Magnificus Prof.dr.ir. T.H.J.J. van der Hagen,
chair of the Board for Doctorates,
to be defended publicly on
Tuesday 25 January 2022 at 10:00 o'clock

by

Xiaohui WANG

Master of Engineering in Instrument Science and Technology,
National University of Defense Technology, China,
born in Jiangsu, China.

This dissertation has been approved by:

Promotor: Prof.dr.ir. H.X. Lin
Promotor: Prof.dr.ir. M. Verlaan

Composition of the doctoral committee:

Rector Magnificus,	chairperson
Prof.dr.ir. H.X. Lin,	Delft University of Technology, promotor
Prof.dr.ir. M. Verlaan,	Delft University of Technology, promotor
Independent members:	
Prof.dr.ir. A.W. Heemink	Delft University of Technology
Prof.dr. -Ing. habil R. Klees	Delft University of Technology
Prof.dr. J.D. Pietrzak	Delft University of Technology
Prof.dr.ir. A.H. Weerts	Wageningen University and Research
Prof.dr. habil.T. Janjic Pfander	KU Eichstätt-Ingolstadt, Germany

Keywords: Global parameter estimation, global tide and surge model, bathymetry, bottom friction coefficient, water level forecast
Printed by: ProefschriftMaken
Cover design by: Sihang Qiu, Xiaohui Wang

Author email: wangxiaohui11@hotmail.com

ISBN 978-94-6423-637-8

An electronic version of this dissertation is available at
http://repository.tudelft.nl/.

Contents

Summary

Coastal flooding is threatening the personal safety, property, and social development of the low-lying land around the coast worldwide. Storm surge is one of the main sources of coastal flooding. Tide and surge models can provide timely water level forecasts for coastal management with the early warning of flooding. Although a regional model can be used to study effects of climate change in a specific area, global water level modeling provides some advantages, such as the long-term response of the extreme sea level and coastal flooding due to global warming and comparison of global surge differences between regions. Global hydrodynamic modeling is becoming an increasingly important research topic. Nowadays, with ever increasing resolution, neglected physical processes and parameter uncertainties due to the inaccurate input or empirical values is becoming more and more dominating the model accuracy. At the same time, measurements like the satellite altimeter and the in-situ tide gauges are able to monitor the water level changes, which offers the possibility to estimate uncertain parameters. In this thesis, we develop a parameter estimation scheme and implement it to a global tide and surge model, and subsequently, apply to improve the water level forecast skill.

The main challenges for large-scale parameter assimilation for tide models are in assessing parameter uncertainties, large computational demand, large memory requirement and insufficient observations. In this thesis, we explore these challenges using an application to the Global Tide and Surge Model (GTSM). A computationally efficient and low memory usage iterative estimation scheme is designed and applied to GTSM for bathymetry and bottom friction coefficient calibration. In addition, we study how to make the best use of spatial sparse distributed observations.

First, we consider the physical processes included in the global tide modeling. Parameter uncertainties in the deep ocean and shallow waters are analyzed separately. The bathymetry in the model is based on a combination of the GEBCO and EMODnet gridded datasets that have large uncertainties caused by the unsurveyed values. Bottom friction is responsible for three quarters of the global tide energy dissipation but the friction parameterization is empirical. Therefore, we select bathymetry and bottom friction as the parameters necessary to be estimated.

We design a parameter estimation scheme that couples a calibration algorithm called DUD (Does not use derivatives) from OpenDA with GTSM. To make the global scale estimation experiments feasible, the computational demands of the methods must be reduced. This demand is proportional to the duration of a single model simulation multiplied by the parameter dimension. Two techniques, a coarse-to-fine strategy that simu-

lates the model in a lower resolution and a sensitivity analysis, have been implemented to reduce the computational cost. This results in a reduction of the computation time of a single model run to one-third and a reduction of parameter dimension of bathymetry from $O(10^6)$ to $O(10^2)$.

The first experiment works and results in a significant improvement, but the simulation time covering 14 days (one spring-neap cycle) makes the calibration results to a bit over-fit the observations. Extension of time-span covered to such as 1 month can solve this problem but results in larger and infeasible memory requirements because all the measurements in the spatial and temporal fields are assimilated in one batch. Model order reduction inspired by the Proper Orthogonal Decomposition algorithm is applied to the temporal patterns of the model output and observations. This results in a reduction of memory requirement by a factor of 22 with a negligible loss of estimation accuracy. We also add outer-loop iterations to further improve the estimation accuracy. This method is similar to Incremental 4D-Var where model increments are simulated in a lower resolution in the inner-loop and updated with the fine grid model in the outer loop. With the combination of these methods, we formulate a new and computationally efficient scheme with a much reduced memory usage and a high estimation accuracy and successfully apply it for bathymetry estimation.

Finally, we extend the estimation to multiple parameters (bathymetry, bottom friction coefficient) and extend our domain of interest to include coastal seas. Even though bottom friction mostly affects the model performance near the coast, time-series in the nearby deep ocean are also impacted to some extent. With the added estimation of bottom friction, the model results are much more accurate compared to the estimation of bathymetry only, especially in the shallow waters. Observations from the FES2014 dataset are well distributed, while tide gauge data from CMEMS, UHSLC datasets, and Arctic stations have an irregular and sparse distribution in some areas. We develop three strategies to make good use of the available observations. The three methods were tested for the European Shelf, Hudson Bay/Labrador, and other coastal areas with large energy dissipation. Experiment results show that model performance is significantly improved both for the deep ocean and shallow waters, and estimation accuracy benefits from the direct use of tide gauge data where available.

Samenvatting

Overstromingen in kustgebieden vormen wereldwijd een bedreiging voor de persoonlijke veiligheid, eigendommen en sociale ontwikkeling van de gemeenschappen die wonen in de laaggelegen kustgebieden. Stormvloed is een van de belangrijkste oorzaken van kustoverstromingen. Getij- en golfslagmodellen worden ingezet om waterstanden te voorspellen zodat er tijdig gewaarschuwd kan worden voor overstromingen. Regionale modellen kunnen worden gebruikt om de effecten van klimaatverandering in een specifiek gebied te bestuderen. Mondiale modellen hebben als voordeel dat ze een langetermijn voorspelling kunnen geven van extreme zeewaterstanden en overstromingen als gevolg van klimaatverandering. Er wordt veel onderzoek gedaan naar globale hydrodynamische modellen. Door de steeds hogere resolutie van de modellen wordt de modelnauwkeurigheid nu vooral bepaald door de verwaarloosde fysische processen en parameter onzekerheden (als gevolg van onnauwkeurige invoer of empirische waarden). Tegelijkertijd is er steeds meer en meer data beschikbaar. Satellietbeelden (altimeter) en in-situ metingen van waterstanden monitoren veranderingen in waterstanden, dit biedt de mogelijkheid om onzekere parameters te schatten. In dit proefschrift ontwikkelen we een parameterkalibratieschema om de parameters te schatten en implementeren we dit in een wereldwijd getijden- en golfslagmodel, om zo de waterstandsvoorspellingen te verbeteren.

De belangrijkste uitdagingen voor grootschalige data assimilatie bij het parameter schatten voor getijdemodellen zijn het bepalen van de parameter onzekerheden, de grote behoefte aan rekenkracht, het benodigde geheugen en onvoldoende waarnemingen. In dit proefschrift onderzoeken we deze uitdagingen aan de hand van het Global Tide and Surge Model (GTSM). Een efficiënt assimilatieschema dat weinig geheugen gebruikt is ontworpen en toegepast op het GTSM voor bathymetrie- en bodemwrijvingscoëfficiëntkalibratie. Daarnaast kijken we hoe we het best gebruik kunnen maken van de ruimtelijk schaars verdeelde waarnemingen.

Eerst bekijken we de fysische processen die in de globale getijdenmodellering zijn opgenomen. Parameteronzekerheden in de diepe oceaan en ondiepe wateren worden afzonderlijk geanalyseerd. De bathymetrie in het model is gebaseerd op een combinatie van twee datasets, GEBCO en EMODnet. Deze datasets hebben grote onzekerheden als gevolg van de niet-onderzochte waarden. Bodemwrijving is verantwoordelijk voor driekwart van de totale dissipatie van getijdenenergie, deze wordt nu vaak geschat met een empirische vergelijking. Wij kiezen om deze reden de bathymetrie en bodemwrijving als parameters die geschat moeten worden met de ontwikkelde methode.

Een parameterkalibratieschema is ontworpen die het kalibratiealgoritme DUD (Does not use derivatives) van OpenDA koppelt aan het GTSM. Om de experimenten op wereldschaal mogelijk te maken, moeten de rekeneisen van de methoden worden verminderd. Deze rekeneis is gelijk aan de duur van een enkele modelsimulatie vermenigvuldigd met de parameterdimensie. Twee technieken zijn toegepast om de rekentijd te verminderen. De eerste techniek is een grof-naar-fijn strategie waarbij het model in een lagere resolutie wordt gesimuleerd, de tweede techniek is het reduceren van de parameterdimensie door middel van een gevoeligheidsanalyse. Hiermee is de rekentijd van een enkele modelrun verminderd tot een derde, en de parameterdimensie van de bathymetrie verkleind van $O(10^6)$ tot $O(10^2)$.

Het eerste experiment was succesvol en resulteerde in een aanzienlijke verbetering, echter waren de kalibratieresultaten bij een simulatietijdspanne van 14 dagen (duur getijdecyclus) overgefit op de waarnemingen. Uitbreiding van de tijdspanne tot bijvoorbeeld 1 maand kan dit probleem oplossen, maar dit resulteert in grotere en onhaalbare geheugenvereisten omdat alle metingen in de ruimtelijke en temporele velden in één batch worden geassimileerd.

Modelreductie geïnspireerd door het Proper Orthogonal Decomposition algoritme is toegepast op de temporele patronen van de modeluitvoer en de waarnemingen. Dit resulteerde in een vermindering van het geheugengebruik met een factor 22, met een verwaarloosbaar verlies aan schattingsnauwkeurigheid. Verder zijn er outer-loop iteraties toegevoegd om de nauwkeurigheid verder te verbeteren. Deze methode is vergelijkbaar met het Incremental 4D-Var waarbij de model incrementen worden gesimuleerd in een lagere resolutie in de inner-loop en worden ge-update met het fine-grid model in de outer-loop. De combinatie van deze methoden heeft geleid tot een nieuw en rekenkundig efficiënt schema voor kalibratie met een hogere nauwkeurigheid, en is met succes toegepast voor bathymetrische schattingen.

Aan het eind schatten we meerdere parameters (bathymetrie, bodemwrijvings coëfficiënt) en breiden we ons interessegebied uit tot kustzeeën. Hoewel bodemwrijving de modelprestaties het meest beïnvloedt nabij de kust, worden modelresultaten van de nabijgelegen diepe oceaan ook tot op zekere hoogte beïnvloed. Met de toegevoegde schatting van bodemwrijving zijn de modelresultaten veel nauwkeuriger in vergelijking met de schatting van alleen de bathymetrie, vooral in de ondiepe wateren. Waarnemingen uit de FES2014 dataset zijn goed verdeeld. Dit geldt niet voor de getijniveaumetingen van CMEMS, UHSLC en Arctische stations, die in sommige gebieden een onregelmatige en schaarse verdeling hebben. Wij hebben daarom drie strategieën ontwikkeld om goed gebruik te maken van de beschikbare observaties. De drie methoden zijn getest voor het Europese continentaal plat, Hudson Bay/Labrador, en andere kustgebieden waar veel energiedissipatie plaatsvindt. De resultaten tonen aan dat de modelprestaties aanzienlijk zijn verbeterd, zowel voor de diepe oceaan als voor ondiepe wateren. Dit laat zien dat de modelnauwkeurigheid verbeterd kan worden door gebruik te maken van beschikbare in-situ metingen van getij, wanneer deze beschikbaar zijn.

Chapter 1

Introduction

Coastal flooding presents a severe threat to people's safety, property, and social development in the coastal zones worldwide. Global hydrodynamic tide and surge models have been identified as the start-of-the-art approach to provide water level forecasts for early flooding warnings. However, model accuracy is affected by some parameters with significant uncertainties that strongly impact the model performance. Parameter estimation can potentially help to reduce parameter uncertainties and is a hot research topic to improve global water-level forecasting skills by increasing the consistency of available observations and model-derived water-level outputs.

1

1.1 Motivation: Storm Surge and Coastal Flooding

Coastal flooding poses a severe threat to many people living in coastal zones throughout the world (Jongman et al., 2012; Muis et al., 2017); over 600 million people living in these regions are affected by this devastating risk (Kron, 2012; McGranahan et al., 2007). For example, the 1953 flood, which caused 2000 deaths, was the most devastating in western Europe in 100 years in terms of loss of life, as captured in Figure 1.1. Another recent disaster is the flooding of New Orleans in 2005 where around 1100 people died (Rappaport, 2014).

Figure 1.1: The North Sea flood of 1953. Source: https://en.wikipedia.org/wiki/North_Sea_flood_of_1953

Coastal flooding is often caused by the combined occurrence of high tide and a severe storm surge. A storm surge is an episodic rise in sea level because of the low atmospheric pressure and shoreward wind-driven water circulation (Muis et al., 2016). The most extreme events are caused by tropical cyclones, which are rapid rotating storms originating over tropical oceans, resulting in extreme wind and rain, and driving extreme sea levels. In interaction, extreme sea-levels significantly intensify wind waves and storm surges (Needham et al., 2015). Wind waves, or wind-generated waves, occur when wind with energy blows over a free surface. The size of wind waves can reach up to 30 m (Mentaschi et al., 2017). In addition, extreme events also occur when extra tropical cyclones, a type of storm system formed in middle or high latitudes, coincide with a high tide. Extratropical cyclones form outside the tropics and have a much larger spatial scale, in contrast to tropical cyclones (Pugh, 1996).

Some researchers have reported that global exposure to flooding has been showing

an upward trend in recent years (Hallegatte et al., 2013; Oppenheimer et al., 2019; Wahl et al., 2017). For example, the global sea level is currently rising at $3-4$mm/year, and the 10-20 cm sea-level rise will lead to more than double the frequency of coastal flooding before the year 2050 (Vitousek et al., 2017). It is estimated that without any adaptation, 0.2–4.6% of the global population will be flooded annually in 2100 with global mean sea-level rising about 25–123 cm (Hinkel et al., 2014). The drivers of increasing risk are the population and economic growth (Jongman et al., 2012), land subsidence (Syvitski et al., 2009), climate change (Nicholls & Cazenave, 2010) and sea level rise (Hallegatte et al., 2013; Rasmussen et al., 2018). Bouwer (2011) reported that social development with the increased exposure and value of capital at risk is still the main driver for coastal flooding. However, climate change, resulting in sea-level rise, will significantly intensify coastal flooding risk (Rasmussen et al., 2018). For instance, changes to storm surge and wind waves are induced by global warming (Jevrejeva et al., 2016; Little et al., 2015), which also affects cyclones (Peduzzi et al., 2012). In recent years, the global mean sea level (GMSL) has been rising rapidly and is expected to continue to accelerate further in the following decades (Chen et al., 2017; Fasullo et al., 2016; Hay et al., 2015; Kopp et al., 2014; Mengel et al., 2016). The GMSL simulation with the fast disintegration of the polar ice sheets is expected to rise up to 5m by 2150 (Eionet, 2021). The rising of mean sea level will also affect tide amplitudes and phases (Idier et al., 2017). The further global sea-level rise has to be studied urgently because of coastal flooding.

1.2 Tide and Surge Models

Timely coastal management, such as flood defences globally and early warnings (Hallegatte et al., 2013) can greatly reduce these risks. Hydrodynamic models are very useful tools for estimating flood risks by providing sea-level forecasts, especially extreme forecasts, and simulating the possible effects of climate changes on tides and extreme sea levels. For example, Jongman et al. (2012) estimated that in 2010, 217 million people were living below the 1/100-year exposure line worldwide according to the analysis of sea-level data from DIVA model (Vafeidis et al., 2008). This number is expected to grow by about 25% by 2050. Muis et al. (2017) used the GTSM to estimate the present day 1/100-year exposure at 158 to 218 million people. The differences in these last two estimates are caused by two different estimates of the extreme sea levels used in their computations, showing that sea-level estimates significantly impact the exposure estimates. Therefore, the reliability of risk identification heavily depends on the model forecast accuracy concerning the tide representations and surge simulation related to climate changes (Ward et al., 2015).

However, most hydrodynamic models cannot simulate tide and surge together. Table 1.1 gives a summary of different kinds of global tide models. Empirical tide models provide tide constituents based on the analysis of data records from satellite altimeter, tide gauges, and/or adopted prior models. An example is GOT4.8 (Ray, 2013), which was developed at the Goddard Space Flight Center. It results from an empirical harmonic analysis of satellite altimetry related to an adopted prior model with a resolution of 0.5°. These tide models can simulate historical tides accurately, but most cannot be used for scenario studies. Purely hydrodynamic forward tide models simulate tides

Table 1.1: Global tide models classification and resolution

Type	Model	Resolution
Empirical tide Models	GOT4.8 (Ray, 2013)	1/2°
	OSU12 (Fok, 2012)	1/4°
	DTU16 (Cheng & Andersen, 2017)	1/8°
	EOT20 (Hart-Davis et al., 2021)	1/8°
	CSR3.0 (Eanes & Bettadpur, 1996)	1°
Purely hydrodynamic models	HYCOM (Arbic et al., 2010)	1/12.5°
	HIM (Arbic et al., 2008)	1/8°
	STORMTIDE (Müller et al., 2012)	1/10°
Hydrodynamic model with data assimilation	HAMTIDE (Taguchi et al., 2013)	1/8°
	FES2014 (Lyard et al., 2021)	1/16°
	TPOX09 (Egbert & Erofeeva, 2002)	1/30°
	NSWC (Schwiderski, 1981)	1°

based on the tidal potential forcing without data constraints. Hydrodynamic tide models with data constraints combine the use of tidal dynamic equations with data assimilation to improve the model accuracy. A detailed comparison of these models is given by Stammer et al. (2014) who concluded that assimilative models are more accurate than non-assimilative models.

In contrast to tides, there are very few global surge models, and most surge simulations are based on regional models. For example, Zijl et al. (2013) developed the Dutch Continental Shelf Model (DCSMv6) for the northwestern European Shelf, which provides a superior representation of tide and surge compared to the previous version. Sea, Lake, and Overland Surges from Hurricanes (SLOSH) is a 2D numerical model developed by the National Weather Service (NWS) of United States; it can be seen as a global model because it can be used to quickly create a regional model everywhere, but its main application is to the entire United States, the Atlantic, and the Gulf of Mexico coastlines (Jelesnianski et al., 1992).

A few global storm surge models do already exist. The Advanced Circulation (ADCIRC) model (Luettich & Westerink, 2004) is a widely used coastal ocean model with the function of forecasting coastal flooding results from extreme events such as hurricanes and tsunamis. Kodaira et al. (2016) developed a global 3D storm-surge model based on Nucleus for European Modeling of the Ocean (NEMO) framework (Madec et al., 2017) and showed the potential benefit of including baroclinic processes in the simulation. Arbic et al. (2010) extended the global 3D HYCOM model with tides. However, these 3D models are computationally quite demanding. Carrère and Lyard (2003a) developed a 2D model MOG2D that is used extensively to correct instantaneous sea surface heights obtained from satellite altimetry. The GTSM (Global Tide and Surge Model) (Verlaan et al., 2015) is a 2D combined global tide and surge model developed by Deltares. Although the behavior of tides and surges is quite linear for the deep ocean and steep coasts, there

may be significant non-linear interaction between tides and surges on the coastal shelf. Both MOG2D and GTSM use an unstructured grid to apply a higher resolution near the coast where the spatial scales are smaller. In addition, global water level can be produced by the combination use of FES2014 and Dynamic Atmospheric Correction (DAC). DAC is computed as the combination on high-frequency elevations from Mog2D/T-UGOm 2D model (Carrère & Lyard, 2003b), but FES2014 and DAC are the gridded datasets without the ability to forecast.

Comparing with regional surge models, global storm surge modeling takes advantage of (1) Providing real-time assessment for coastal flooding with global surge modeling, combining with the refinement in shallow waters; (2) Studying the long-term response of the extreme sea level and coastal flooding resulting from the global climate changes; (3) Comparing and analyzing the surge difference globally; and (4) Researching the interaction between the coastal surge and water level in the deep ocean. For example, the first global reanalysis of storm surges and extreme sea levels called Global tide and Surge Reanalysis (GTSR) is presented based on the GTSM (Muis et al., 2016). GTSR consists of the world's coastlines, time series of tides, surges, and extreme sea-level estimates. GTSR can be applied to assess flood risk and the impacts of climate change (Muis et al., 2017). In addition, global tide and surge models have many other applications, ranging from providing boundary conditions for coastal models (Zijl et al., 2013) or in the processing of satellite gravity data (Dahle et al., 2019).

In this thesis, we begin with an analysis of the model performance of the GTSM and investigate strategies to improve the model accuracy by parameter estimation, particularly aiming at higher level of accuracy in water-level prediction, especially in coastal regions.

1.3 Parameter Estimation Applications for Tide and Surge Models

Even though existing models are continuously under development with improvements in the descriptions of physical processes and the grid resolution, several sources of model errors remain: the approximation of the physical processes, uncertainty in the parameters, that are not known accurately, such as bathymetry, bottom friction and internal tides friction. Parameter estimation is a promising approach for reducing parameter uncertainties with available data, e.g., altimeter and tide gauge measurements.

Parameter estimation can be seen as finding the best values of parameters using a numerical model and data assimilation or other similar techniques. Data assimilation is a technique where observation data are combined with the results from numerical models, optimizing the evolving state variables of the system. Kalnay (2002) defined data assimilation as "a statistical combination of observations and short-range forecasts". It can also be understood as "the computation of the probability density function of model solution conditioned on the measured observations" (Evensen, 2006). A data assimilation system consists of a set of observations, a dynamic model, and a data assimilation scheme, as Figure 1.2 shows. In data assimilation, it is assumed that both models and observations contain uncertainties. Observations have errors ranging from instrumental

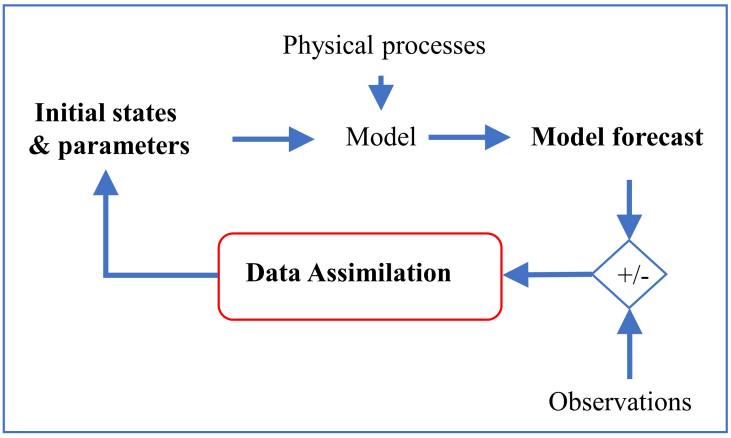

Figure 1.2: Data assimilation flow chart

noise and representation errors. A model contains uncertainties from the approximate physical parameterization, inaccurate input information, and low resolution.

Data assimilation algorithms can be classified as sequential and variational methods (Evensen & van Leeuwen, 2000; Talagrand, 1997). Sequential data assimilation such as the Kalman filter estimates unknown variables (state and parameters) by estimating a joint probability distribution of the analyses and forecasts. Variational data assimilation, such as 4D-Var, is a powerful method to optimize the initial states, boundary, or model input, aiming to obtain the posterior (model output from the optimization) that optimally fits all the observations over an assimilative time window. It provides a powerful approach to update or estimate the initial states and parameters of a dynamic model.

In various earth science disciplines, including meteorology (Navon, 2009), oceanography (Edwards et al., 2015), and hydrology, data assimilation is being applied as one of the core techniques for modern forecasting. Parameter estimation is one possible application of data assimilation that focuses on tuning parameter values for good model performance. Here we will consider parameters such as bathymetry, bottom friction coefficients and internal tide friction coefficients, that affect the tide model performance globally. If these parameters in the model are incorrect/inaccurate, the model-derived output (water level in tide models) will not be equal to the observed measurements. In a comparison of several assimilative and non-assimilative global tide models, Stammer et al. (2014) also reported that data assimilation/parameter estimation could contribute significantly to the accuracy of global tide models.

Parameter estimation has been widely applied for dynamic ocean tide models (Edwards et al., 2015). In the tide and surge modeling field, both sequential (Altaf et al., 2012; Mayo et al., 2014) and variational (Heemink et al., 2002; Zaron, 2017, 2019) methods have been adopted to estimate the water level representations or parameters with significant uncertainties.

For regional tide models, the main sources of uncertainties are generally assumed to be bathymetry, bottom friction coefficients and water level states in the model grid

boundary. Das and Lardner (1991) showed the feasibility of estimating bottom friction coefficients and water depth for a coastal hydraulic model with periodic tidal observation. Many scientists such as Ten Brummelhuis et al. (1993) and Heemink et al. (2002) have investigated the estimation of harmonic constants in open boundary conditions and parameters such as space varying friction, viscosity, and depth values, for the European Continental Shelf using the adjoint method. Altaf et al. (2012) applied a Proper Orthogonal Decomposition (POD) based calibration approach to calibrate a large-scale shallow-water flow model called the Dutch Continental Shelf Model (DCSM). Zijl et al. (2013) developed and estimated bathymetry and bottom friction coefficients for a new generation DCSMv6 in this region.

Moreover, Zaron (2017) examined and identified the sensitivity of barotropic tides to bottom topography and frictional parameters by variational inverse methods. Zaron (2019) further assimilated CryoSat-2 data into a barotropic tide model with a variational approach. The Kalman filter with ensembles has also been applied for the parameter estimation. For instance, Mayo et al. (2014) proposed the use of the Singular Evaluative Interpolated Kalman filter (SEIK) for estimating Manning's coefficients for an Advanced Circulation (ADCIRC) model at the coast and concluded that accurate estimation is dependent on the sensitivity of the model output to the parameter. Barth et al. (2010) assimilate HF-RADAR current observations with an ensemble smoother to optimize boundary values in the General Estuarine Ocean Model (GETM).

However, so far only a few studies on parameter estimation for a global hydrodynamic model have been reported in the literature (Lyard et al., 2021). Several studies focus on worldwide data assimilation to improve the accuracy of state variables such as tide components in the FES2014 dataset that assimilate satellite altimeter and tide gauge data. The state variable estimation can provide a highly accurate tidal forecast but it is challenging for water level representation and climate change studies.

In the global ocean tide model estimation problem, it is not necessary to estimate boundary conditions because the model is forced by potential tidal forcing. However, bathymetry and bottom friction coefficients and internal tide friction that generate tide energy dissipation in the deep ocean still have to be estimated.

1.4 Observations

Parameter estimation can be implemented only when observations are available. We investigate water level observations at a global scale. Water level can be collected from tide gauge data, satellite altimeter, or reanalysis datasets such as the FES2014 dataset.

1.4.1 Tide Gauge Data

Global sea level records from tide gauges are important sources for monitoring sea level rise (SLR). Gauges are in-situ recorders that cover a long period of time. Most tide gauge locations are distributed around the coastline, which facilitates the study of the tide, surge, and coastal flooding. However, the spatial distribution of the tide gauges is uneven, sometimes resulting in large gaps for some coastal areas. There are several

large collections of tide gauge data available, for example, the PSMSL dataset, the UHSLC dataset, the CMEMS dataset, and Arctic Stations. Here we list the datasets UHSLC, CMEMS and Arctic stations that are used in our study, as Figure 1.3 shows.

- UHSLC dataset: University of Hawaii Sea Level Center dataset

  The University of Hawaii Sea Level Centre (UHSLC) has a global collection of approximately 500 tide gauge time series (Caldwell & Thompson, 2015). The availability of data varies over the years, with the number of locations increasing over time, except for the few most recent years. The distribution of the station locations is somewhat irregular, and most sites are in coastal areas (Figure 1.3a). Two levels of quality control, Fast Delivery (FD) and Research Quality Data (RQD), are provided in the UHSLC dataset. RQD is considered the final science-ready data and is used in this thesis.

- CMEMS dataset: Copernicus Marine Environment Monitoring Service dataset

  CMEMS has a collection of in-situ tide gauges located in the Arctic Ocean, Baltic Ocean, European North-West Shelf Seas, Iberian-Biscay-Ireland regional seas, Black Sea and Mediterranean sea. All the available data are published after data acquisition, quality control, product validation, and product distribution. (Figure 1.3b).

- Arctic Stations (Figure 1.3c):

  Kowalik and Proshutinsky (1994) described approximately 300 tide stations in the Arctic Ocean and studied the tide performance. Four major tide constituents, semidiurnal constituents M2 and S2, and diurnal constituents K1 and O1 are available. We have to note that only four major tide constituents are available, and they cannot fully represent the tide time-series with the analysis of all the components. However, this data is still helpful to evaluate the model performance in the frequency domain.

1.4.2 Satellite Altimeter Data

A satellite altimeter is a unique instrument that measures the time it takes for a radar pulse to travel from a satellite to the surface of the earth and back to the satellite. Physical information from the averaged waveform of a radar altimeter comprises distance to sea surface, back scatter and significant wave height. Sea surface height can be calculated by combining with the precise satellite location. The satellite altimeter can also map the sea surface wind speeds and significant wave heights. A total number of 10 altimeter missions have flown in the past, starting in 1973 (Vignudelli et al., 2019). It is a valuable tool for sea-level monitoring and ocean circulation study. Some researchers have reported that a satellite altimeter has the capability to observe and study storm surge features, e.g., in Hurricane Sandy (Lillibridge et al., 2013). The use of satellite altimeters to improve the storm surge simulation with the data assimilation in the Adriatic Sea and around Venice has been reported in Biancamaria et al. (2016).

However, even though satellite altimeters can provide spatially well-distributed coverage, they have a low temporal resolution. For instance, the relative repeat cycle for

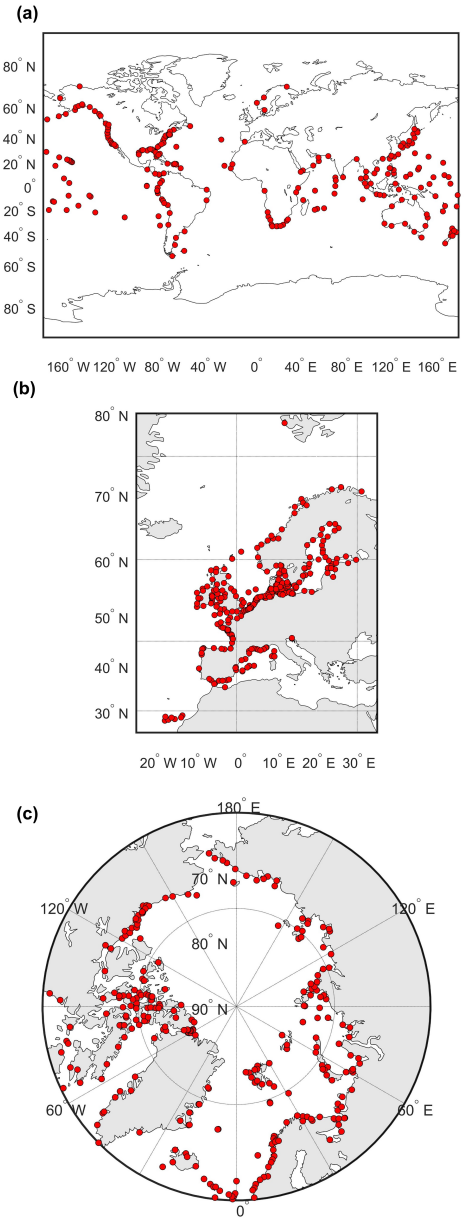

Figure 1.3: Available tide gauge locations (a) UHSLC dataset; (b) CMEMS dataset; (c) Arctic stations.

1

TOPEX / Poseidon is about 10 days with a wide cross-track spacing (350km). Moreover, the higher cross-track spatial resolution always follows with the expense of a longer repeat cycle, e.g., CryoSat-2 has a resolution of 7.5km and a repeat cycle of 365 days. We need a few decades of altimeter for tidal analysis. In addition, only TOPEX/Poseidon and Jason series were designed to be applied to tides. The ground track, as shown in Figure 1.4, cannot cover the poles. Therefore, the utilization of satellite altimeter data for global parameter estimation is still limited because of the long time frame required to obtain full coverage, the complex harmonic tidal analysis, and the high computational cost.

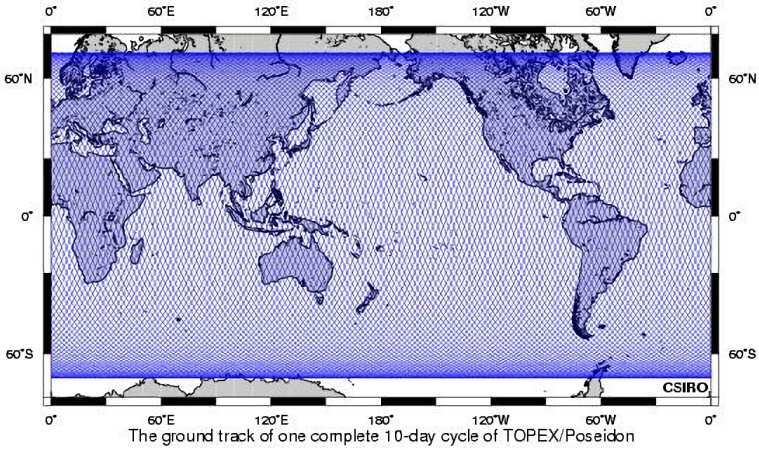

Figure 1.4: Ground track of TOPEX/Poseidon. Source: https://www.cmar.csiro.au/sealevel/sl_meas_sat_alt.html

1.4.3 Gridded Tides: FES2014

The FES2014 dataset was produced by Noveltis, Legos, and CLS and distributed by Aviso+, with support from CNES (https://www.aviso.altimetry.fr/). It comes from the FES (Finite Element Solution) tide model consisting of about 2.9 million nodes. Long altimeter time series (Topex/Poseidon, Jason-1, Jason-2, TPN-J1N, and ERS-1, ERS-2, ENVISAT), tide gauges, improved modeling, and data assimilation techniques have all provided an accurate solution for FES2014 (Carrere et al., 2013; Lyard et al., 2021). Thirty-four tide constituents are included in the FES2014 dataset with a gridded resolution of 1/16°. The main advantage of using a tidal database such as FES2014 is that a tide time series can be obtained for arbitrary periods globally and without complex analysis of the direct usage of satellite altimeter. Stammer et al. (2014) also compared the output of some models with and without data assimilation. FES2012 showed excellent accuracy when compared with tide gauge and satellite altimeter data. FES2014 is the updated version of FES2012.

In summary, tide and surge representations can be obtained from tide gauge data in coastal areas, but there is a spatially-sparse distribution. A satellite altimeter can provide

an excellent spatial coverage except in coastal areas but it has a low temporal resolution. Gridded FES2014 dataset has been identified as high accuracy global observations without time and location limits, but only tide components are available. In this study, we mainly use tide gauge data and FES2014 dataset as observations for the parameter estimation.

1.5 Outline of This Thesis

1.5.1 Aim

From the previous discussion, we can conclude that global sea-level forecasts are urgently required for the assessment of coastal flooding, and that tide and surge models have the capability to provide them. But the forecasting skills of the existing tide and surge models are limited by several parameters with significant uncertainties that heavily affect the model performance. Nevertheless, given a sufficient number of measurements, parameter estimation has the potential to reduce these uncertainties and thus improve the model performance.

Therefore, this thesis aims to develop a global parameter estimation system for tide and surge models. The system allows for estimating multiple global types of parameters and assimilation of observations in the deep ocean and shallow waters with acceptable computational demands.

1.5.2 Research Questions

In this thesis, the research focuses on the combination of global tide surge models and observation, making use of data assimilation to estimate the uncertain parameters in these models. The specific research questions studied in this thesis are:

1. For a successful application of parameter estimation that significantly improves the skill of the model, it is crucial to consider the right parameters and observations. **Rq 1: Which uncertain parameters and other uncertainties determine the accuracy of hydrodynamic global tide and surge models? And which measurements are needed to estimate them?**

   To answer this question, Chapter 3 discusses the relevant physical processes and performs a number of sensitivity experiments for estimation of the parameters related to the deep ocean. Chapter 5 revisits the topic, but now with a focus on coastal seas.

2. In this thesis, we will estimate the parameters through minimization of a cost function that expresses the misfit between the model and observations. The specific definition of the cost function can have a large impact on the final result, but also on the performance. **Rq 2: How to define a cost function for the parameter estimation problem that gives a good fit between the model and observations and that can be optimized with a feasible computational cost?**

Chapter 3 discusses the definition of the cost function and reduction of the size of parameter vector. Chapter 5 extends the approach to the more complex case of coastal seas.

3. A single model run of the GTSM requires about 250 core hours for a 45-day simulation. In addition, we want to use millions of measurements to optimize over a hundred parameters. Thus the minimization of the cost function will only be feasible if the estimation algorithm and it's implementation are very efficient. **Rq 3: How can we minimize the cost function in a way that is sufficiently efficient to make the computations feasible?**

   Chapter 3 introduces the DUD (Doesnot use derivatives) algorithm, which forms the core of the optimization and a number of optimizations. A coarse-to-fine strategy is proposed to reduce the CPU time used for the estimation. Chapter 4 proposes a projection method to reduce the memory needed for the cost function computations, which results in a state-of-art approach dealing effectively with the huge memory requirement. In Chapter 4, we propose an outer-loop iteration to further improve the estimation accuracy, similar to Incremental 4D-Var.

1.5.3 Organization of the Thesis

The thesis is organized as follows:

- Chapter 2: The Global Tide and Surge Model (GTSM) that we use in this thesis is introduced. An analysis of parameter uncertainty for the deep ocean and coastal regions is included, and a sensitivity analysis is performed to study the influence of the most important parameters on the accuracy of the GTSM.
- Chapter 3: A computational-efficient parameter estimation scheme with the coarse-to-fine strategy to reduce the computational cost is developed. It is applied to global bathymetry calibration, resulting in better consistency between the model output and observations.
- Chapter 4: The model order reduction application in the temporal patterns for parameter estimation is described in order to reduce the memory requirement resulting from a large number of measurements and parameters. Combined with outer-loop implementation, similar to Incremental 4D-Var, an estimation scheme with high computation efficiency and low memory requirement is formulated.
- Chapter 5: The parameter estimation scheme for the global estimation of bottom friction coefficient and bathymetry is applied in shallow water and this significantly improves the model performance. We study several strategies to make the best possible use of sparse and unevenly distributed tide gauges.
- Chapter 6: This chapter summarizes the conclusions of this thesis, including a discussion of the research questions and the recommendations for further research.

Bibliography

Altaf, M. U., Verlaan, M., & Heemink, A. W. (2012). Efficient identification of uncertain parameters in a large-scale tidal model of the european continental shelf by proper orthogonal decomposition. *International Journal for Numerical Methods in Fluids*, *68*(4), 422–450. https://doi.org/10.1002/fld.2511

Arbic, B. K., Mitrovica, J. X., MacAyeal, D. R., & Milne, G. A. (2008). On the factors behind large labrador sea tides during the last glacial cycle and the potential implications for heinrich events. *Paleoceanography*, *23*(3). https://doi.org/https://doi.org/10.1029/2007PA001573

Arbic, B. K., Wallcraft, A. J., & Metzger, E. J. (2010). Concurrent simulation of the eddying general circulation and tides in a global ocean model. *Ocean Modelling*, *32*(3), 175–187. https://doi.org/https://doi.org/10.1016/j.ocemod.2010.01.007

Barth, A., Alvera-Azcárate, A., Gurgel, K.-W., Staneva, J., Port, A., Beckers, J.-M., & Stanev, E. V. (2010). Ensemble perturbation smoother for optimizing tidal boundary conditions by assimilation of high-frequency radar surface currents – application to the german bight. *Ocean Science*, *6*(1), 161–178. https://doi.org/10.5194/os-6-161-2010

Biancamaria, S., Lettenmaier, D. P., & Pavelsky, T. M. (2016). The SWOT Mission and Its Capabilities for Land Hydrology. *Surveys in Geophysics*, *37*(2), 307–337. https://doi.org/10.1007/s10712-015-9346-y

Bouwer, L. M. (2011). Have disaster losses increased due to anthropogenic climate change? *Bulletin of the American Meteorological Society*, *92*(1), 39–46. http://www.jstor.org/stable/26226798

Caldwell, M. A. M., P. C., & Thompson, P. R. (2015). Sea level measured by tide gauges from global oceans – the joint archive for sea level holdings (ncei accession 0019568), version 5.5. *NOAA National Centers for Environmental Information, Dataset*. https://doi.org/10.7289/V5V40S7W

Carrere, L., Lyard, F., Cancet, M., Guillot, A., & Roblou, L. (2013). FES 2012: A New Global Tidal Model Taking Advantage of Nearly 20 Years of Altimetry. *20 Years of Progress in Radar Altimatry*, *710*, Article 13, 13.

Carrère, L., & Lyard, F. (2003a). Modeling the barotropic response of the global ocean to atmospheric wind and pressure forcing - comparisons with observations. *Geophysical Research Letters*, *30*(6). https://doi.org/10.1029/2002GL016473

Carrère, L., & Lyard, F. (2003b). Modeling the barotropic response of the global ocean to atmospheric wind and pressure forcing - comparisons with observations. *Geo-*

physical Research Letters, *30*(6). https://doi.org/https://doi.org/10.1029/2002GL016473

Chen, X., Zhang, X., Church, J., Watson, C., King, M. A., Monselesan, D., Legrésy, B., & Harig, C. (2017). The increasing rate of global mean sea-level rise during 1993–2014. *Nature Climate Change*, *7*, 492–495.

Cheng, Y., & Andersen, O. B. (2017). Towards further improving dtu global ocean tide model in shallow waters and polar seas, ostst. *Proceedings of the Ocean Surface Topography Science Team (OSTST) Meeting, Miami, FL, USA, 23–27 October 2017*.

Dahle, C., Murböck, M., Flechtner, F., Dobslaw, H., Michalak, G., Neumayer, K., Abrykosov, O., Reinhold, A., König, R., Sulzbach, R., & et al. (2019). The gfz grace rl06 monthly gravity field time series: Processing details and quality assessment. *Remote Sensing*, *11*(18), 2116. https://doi.org/10.3390/rs11182116

Das, S. K., & Lardner, R. W. (1991). On the estimation of parameters of hydraulic models by assimilation of periodic tidal data. *Journal of Geophysical Research: Ocean*, *96*, 15. https://doi.org/10.1029/91JC01318

Eanes, R., & Bettadpur, S. (1996). *The csr 3.0 global ocean tide model: Diurnal and semidiurnal tides from topex/poseidon altimetry*. Center for Space Research. https://books.google.nl/books?id=RibBPgAACAAJ

Edwards, C. A., Moore, A. M., Hoteit, I., & Cornuelle, B. D. (2015). Regional ocean data assimilation [PMID: 25103331]. *Annual Review of Marine Science*, *7*(1), 21–42. https://doi.org/10.1146/annurev-marine-010814-015821

Egbert, G. D., & Erofeeva, S. Y. (2002). Efficient inverse modeling of barotropic ocean tides. *Journal of Atmospheric and Oceanic Technology*, *19*(2), 183–204. https://doi.org/10.1175/1520-0426(2002)019<0183:EIMOBO>2.0.CO;2

Eionet. (2021). *Global and european sea level rise*. Retrieved November 18, 2021, from https://www.eea.europa.eu/ims/global-and-european-sea-level-rise

Evensen, G. (2006). *Data assimilation: The ensemble kalman filter*. Springer-Verlag.

Evensen, G., & van Leeuwen, P. J. (2000). An Ensemble Kalman Smoother for Nonlinear Dynamics. *Monthly Weather Review*, *128*(6), 1852–1867. https://doi.org/10.1175/1520-0493(2000)128<1852:AEKSFN>2.0.CO;2

Fasullo, J. T., Nerem, R. S., & Hamlington, B. (2016). Is the detection of accelerated sea level rise imminent? *Scientific Reports*, *6*(1). https://doi.org/10.1038/srep31245

Fok, H. S. (2012). Ocean tides modeling using satellite altimetry. *Geodetic Science Rep. No.501*.

Hallegatte, S., Green, C., Nicholls, R., & Corfee-Morlot, J. (2013). Future flood losses in major coastal cities. *Nature Climate Change*, (3), 802–806. https://doi.org/10.1038/nclimate1979

Hart-Davis, M. G., Piccioni, G., Dettmering, D., Schwatke, C., Passaro, M., & Seitz, F. (2021). Eot20: A global ocean tide model from multi-mission satellite altimetry. *Earth System Science Data*, *13*(8), 3869–3884. https://doi.org/10.5194/essd-13-3869-2021

Hay, C. C., Morrow, E., Kopp, R. E., & Mitrovica, J. X. (2015). Probabilistic reanalysis of twentieth-century sea-level rise. *Nature*, *517*(7535), 481–484. https://doi.org/10.1038/nature14093

Heemink, A., Mouthaan, E., Roest, M., Vollebregt, E., Robaczewska, K., & Verlaan, M. (2002). Inverse 3d shallow water flow modelling of the continental shelf. *Continental Shelf Research*, *22*(3), 465–484. https://doi.org/https://doi.org/10.1016/S0278-4343(01)00071-1

Hinkel, J., Lincke, D., Vafeidis, A. T., Perrette, M., Nicholls, R. J., Tol, R. S. J., Marzeion, B., Fettweis, X., Ionescu, C., & Levermann, A. (2014). Coastal flood damage and adaptation costs under 21st century sea-level rise. *Proceedings of the National Academy of Sciences*, *111*(9), 3292–3297. https://doi.org/10.1073/pnas.1222469111

Idier, D., Paris, F., Cozannet, G., Boulahya, F., & Dumas, F. (2017). Sea-level rise impacts on the tides of the european shelf. *Continental Shelf Research*, *137*, 56–71.

Jelesnianski, C., Chen, J., & Shaffer, W. (1992). Slosh: Sea, lake, and overland surges from hurricanes.

Jevrejeva, S., Jackson, L., Riva, R., Grinsted, A., & Moore, J. C. (2016). Coastal sea level rise with warming above 2 °c. *Proceedings of the National Academy of Sciences*, *113*, 13342–13347.

Jongman, B., Ward, P. J., & Aerts, J. C. (2012). Global exposure to river and coastal flooding: Long term trends and changes. *Global Environmental Change*, *22*(4), 823–835. https://doi.org/https://doi.org/10.1016/j.gloenvcha.2012.07.004

Kalnay, E. (2002). *Atmospheric modeling, data assimilation and predictability*. Cambridge University Press. https://doi.org/10.1017/CBO9780511802270

Kodaira, T., Thompson, K. R., & Bernier, N. B. (2016). The effect of density stratification on the prediction of global storm surges. *Ocean Dynamics*, *66*, 1733–1743.

Kopp, R., Horton, R., Little, C., Mitrovica, J., Oppenheimer, M., Rasmussen, D., Strauss, B., & Tebaldi, C. (2014). Probabilistic 21st and 22nd century sea-level projections at a global network of tide-gauge sites. *Earth's Future*, *2*, 383–406.

Kowalik, Z., & Proshutinsky, A. Y. (1994). The arctic ocean tides. *The polar oceans and their role in shaping the global environment* (pp. 137–158). American Geophysical Union (AGU). https://doi.org/https://doi.org/10.1029/GM085p0137

Kron, W. (2012). Coasts: The high-risk areas of the world. *Natural Hazards*, *66*, 1363–1382.

Lillibridge, J., Lin, M., & Shum, C. (2013). Hurricane sandy storm surge measured by satellite altimetry. *Oceanography*, *26*(2), 8–9.

Little, C. M., Horton, R. M., Kopp, R. E., Oppenheimer, M., Vecchi, G. A., & Villarini, G. (2015). Joint projections of US East Coast sea level and storm surge. *Nature Climate Change*, *5*(12), 1114–1120. https://doi.org/10.1038/nclimate2801

Luettich, R. A., & Westerink, J. J. (2004). *Formulation and numerical implementation of the 2d/3d adcirc finite element model version 44. xx*. Citeseer.

Lyard, F. H., Allain, D. J., Cancet, M., Carrère, L., & Picot, N. (2021). Fes2014 global ocean tide atlas: Design and performance. *Ocean Science*, *17*(3), 615–649. https://doi.org/10.5194/os-17-615-2021

Madec, G., Bourdallé-Badie, R., Bouttier, P.-A., Bricaud, C., Bruciaferri, D., Calvert, D., Chanut, J., Clementi, E., Coward, A., Delrosso, D., et al. (2017). Nemo ocean engine.

Mayo, T., Butler, T., Dawson, C. N., & Hoteit, I. (2014). Data assimilation within the advanced circulation (adcirc) modeling framework for the estimation of manning's friction coefficient. *Ocean Modelling*. http://hdl.handle.net/10754/563473

McGranahan, G., Balk, D., & Anderson, B. (2007). The rising tide: Assessing the risks of climate change and human settlements in low elevation coastal zones. *Environment and Urbanization*, *19*(1), 17–37. https://doi.org/10.1177/0956247807076960

Mengel, M., Levermann, A., Frieler, K., Robinson, A., Marzeion, B., & Winkelmann, R. (2016). Future sea level rise constrained by observations and long-term commitment. *Proceedings of the National Academy of Sciences*, *113*, 2597–2602.

Mentaschi, L., Vousdoukas, M. I., Voukouvalas, E., Dosio, A., & Feyen, L. (2017). Global changes of extreme coastal wave energy fluxes triggered by intensified teleconnection patterns. *Geophysical Research Letters*, *44*(5), 2416–2426. https://doi.org/https://doi.org/10.1002/2016GL072488

Muis, S., Verlaan, M., Nicholls, R. J., Brown, S., Hinkel, J., Lincke, D., Vafeidis, A. T., Scussolini, P., Winsemius, H. C., & Ward, P. J. (2017). A comparison of two global datasets of extreme sea levels and resulting flood exposure. *Earth's Future*, *5*(4), 379–392. https://doi.org/10.1002/2016EF000430

Muis, S., Verlaan, M., Winsemius, H., Aerts, J., & Ward, P. (2016). A global reanalysis of storm surges and extreme sea levels. *Nature Communications*, *7*, 1–12. https://doi.org/10.1038/ncomms11969

Müller, M., Cherniawsky, J. Y., Foreman, M. G. G., & von Storch, J.-S. (2012). Global m2 internal tide and its seasonal variability from high resolution ocean circulation and tide modeling. *Geophysical Research Letters*, *39*(19). https://doi.org/https://doi.org/10.1029/2012GL053320

Navon, I. M. (2009). Data assimilation for numerical weather prediction: A review. In S. K. Park & L. Xu (Eds.), *Data assimilation for atmospheric, oceanic and hydrologic applications* (pp. 21–65). Springer Berlin Heidelberg. https://doi.org/10.1007/978-3-540-71056-1_2

Needham, H. F., Keim, B. D., & Sathiaraj, D. (2015). A review of tropical cyclone-generated storm surges: Global data sources, observations, and impacts. *Reviews of Geophysics*, *53*(2), 545–591. https://doi.org/https://doi.org/10.1002/2014RG000477

Nicholls, R. J., & Cazenave, A. (2010). Sea-level rise and its impact on coastal zones. *Science*, *328*(5985), 1517–1520. https://doi.org/10.1126/science.1185782

Oppenheimer, M., Glavovic, B., Hinkel, J., Wal, R. V. D., Magnan, A., Abd-EIGawad, A., Cai, R., Cifuentes-Jara, M., DeConto, R., Ghosh, T., Hay, J., Isla, F., Marzeion, B., Meyssignac, B., & Sebesvári, Z. (2019). Sea level rise and implications for low lying islands, coasts and communities.

Peduzzi, P., Chatenoux, B., Dao, Q.-H., De Bono, A., Herold, C., Kossin, J., Mouton, F., & Nordbeck, O. (2012). Global trends in tropical cyclone risk [ID: unige:23652]. *Nature Climate Change*, *2*(4), 289–294. https://archive-ouverte.unige.ch/unige:23652

Pugh, D. (1996). *Tides, surges and mean sea-level* [Book out of print - COPYRIGHT OWNED BY AUTHOR]. John Wiley & Sons, Ltd. https://eprints.soton.ac.uk/19157/

Rappaport, E. N. (2014). Fatalities in the United States from Atlantic Tropical Cyclones: New Data and Interpretation. *Bulletin of the American Meteorological Society*, *95*(3), 341–346. https://doi.org/10.1175/BAMS-D-12-00074.1

Rasmussen, D. J., Bittermann, K., Buchanan, M. K., Kulp, S., Strauss, B. H., Kopp, R. E., & Oppenheimer, M. (2018). Extreme sea level implications of 1.5 °c, 2.0 °c, and 2.5

°c temperature stabilization targets in the 21st and 22nd centuries. *Environmental Research Letters*, *13*(3), 034040. https://doi.org/10.1088/1748-9326/aaac87

Ray, R. D. (2013). Precise comparisons of bottom-pressure and altimetric ocean tides. *Journal of Geophysical Research: Oceans*, *118*(9), 4570–4584. https://doi.org/https://doi.org/10.1002/jgrc.20336

Schwiderski, E. W. (1981). Global ocean tides. part ii. the semidiurnal principal lunar tide (m2), atlas of tidal charts and maps.

Stammer, D., Ray, R. D., Andersen, O. B., Arbic, B. K., Bosch, W., Carrère, L., Cheng, Y., Chinn, D. S., Dushaw, B. D., Egbert, G. D., Erofeeva, S. Y., Fok, H. S., Green, J. A. M., Griffiths, S., King, M. A., Lapin, V., Lemoine, F. G., Luthcke, S. B., Lyard, F., … Yi, Y. (2014). Accuracy assessment of global barotropic ocean tide models. *Reviews of Geophysics*, *52*(3), 243–282. https://doi.org/10.1002/2014RG000450

Syvitski, J. P. M., Kettner, A. J., Overeem, I., Hutton, E. W. H., Hannon, M. T., Brakenridge, G. R., Day, J., Vörösmarty, C., Saito, Y., Giosan, L., & Nicholls, R. J. (2009). Sinking deltas due to human activities. *Nature Geoscience*, *2*(10), 681–686. https://doi.org/10.1038/ngeo629

Taguchi, E., Stammer, D., & Zahel, W. (2013). Inferring deep ocean tidal energy dissipation from the global high-resolution data-assimilative HAMTIDE model. *Journal of Geophysical Research: Oceans*, *119*(7), 4573–4592. https://doi.org/10.1002/2013JC009766

Talagrand, O. (1997). Assimilation of observations, an introduction (gtspecial issueltdata assimilation in meteology and oceanography: Theory and practice). *Journal of the Meteorological Society of Japan. Ser. II*, *75*(1B), 191–209. https://doi.org/10.2151/jmsj1965.75.1B_191

Ten Brummelhuis, P. G. J., Heemink, A. W., & van den Boogaard, H. F. P. (1993). Identification of shallow sea models. *International Journal for Numerical Methods in Fluids*, *17*(8), 637–665. https://doi.org/10.1002/fld.1650170802

Vafeidis, A. T., Nicholls, R. J., McFadden, L., Tol, R. S. J., Hinkel, J., Spencer, T., Grashoff, P. S., Boot, G., & Klein, R. J. T. (2008). A new global coastal database for impact and vulnerability analysis to sea-level rise. *Journal of Coastal Research*, *24*(4), 917–924. http://www.jstor.org/stable/40065185

Verlaan, M., De Kleermaeker, S., & Buckman, L. (2015). GLOSSIS: Global storm surge forecasting and information system [online]. *Australasian Coasts & Ports Conference 2015: 22nd Australasian Coastal and Ocean Engineering Conference and the 15th Australasian Port and Harbour Conference.*, 229–234.

Vignudelli, S., Scozzari, A., Abileah, R., Gómez-Enri, J., Benveniste, J., & Cipollini, P. (2019). Chapter four - water surface elevation in coastal and inland waters using satellite radar altimetry. In V. Maggioni & C. Massari (Eds.), *Extreme hydroclimatic events and multivariate hazards in a changing environment* (pp. 87–127). Elsevier. https://doi.org/https://doi.org/10.1016/B978-0-12-814899-0.00004-3

Vitousek, S., Barnard, P., Fletcher, C., Frazer, N., Erikson, L., & Storlazzi, C. (2017). Doubling of coastal flooding frequency within decades due to sea-level rise. *Scientific Reports*, *7*.

Wahl, T., Haigh, I. D., Nicholls, R. J., Arns, A., Dangendorf, S., Hinkel, J., & Slangen, A. B. A. (2017). Understanding extreme sea levels for broad-scale coastal impact and

adaptation analysis. *Nature Communications*, *8*, Article 16075, 16075. https://doi.org/10.1038/ncomms16075

Ward, P., Jongman, B., Salamon, P., Simpson, A., Bates, P., de Groeve, T., Muis, S., Coughlan, E., Rudari, R., Trigg, M., & Winsemius, H. (2015). Usefulness and limitations of global flood risk models. *Nature Climate Change*, *5*, 712–715. https://doi.org/10.1038/nclimate2742

Zaron, E. D. (2017). Topographic and frictional controls on tides in the sea of okhotsk. *Ocean Modelling*, *117*, 1–11. https://doi.org/https://doi.org/10.1016/j.ocemod.2017.06.011

Zaron, E. D. (2019). Simultaneous estimation of ocean tides and underwater topography in the weddell sea. *Journal of Geophysical Research: Oceans*, *124*(5), 3125–3148. https://doi.org/10.1029/2019JC015037

Zijl, F., Verlaan, M., & Gerritsen, H. (2013). Improved water-level forecasting for the northwest european shelf and north sea through direct modelling of tide, surge and non-linear interaction. *Ocean Dynamics*, *63*(7), 823–847. https://doi.org/10.1007/s10236-013-0624-2

Chapter 2

Global Tide and Surge Model

In this chapter, we introduce the Global Tide and Surge model (GTSM) and assess the parameter uncertainties for the deep ocean and shallow water with the sensitivity analysis.

Parts of this chapter have been published in Wang et al. (2021):

Wang, X., Verlaan, M., Apecechea, M. I., and Lin, H. X. (2021). Computation-efficient Parameter Estimation for a High-resolution Global Tide and Surge Model. Journal of Geophysical Research: Oceans, 126, e2020JC016917.

2.1 Global Tide and Surge Model

In this thesis, the Global Tide and Surge Model(GTSM) is used to simulate the ocean tide and surge at a global scale. The GTSM is a depth-averaged hydrodynamic model that forms the core in the Global Storm Surge Information System (GLOSSIS) to provide water level and storm surge forecasts globally. These real-time forecasts can be used for early warning systems and to provide boundary conditions for regional models (Verlaan et al., 2015).

The first release of GTSM was in 2015 (Verlaan et al., 2015) with grid cells of 50 km resolution in the deep ocean and 5 km resolution along the coast. Bathymetry was derived from the General Bathymetric Chart of the Oceans dataset (GEBCO 30 arc-second grid) (Weatherall et al., 2015). The self-attraction and loading (SLA) requires the global integrals of the ocean bottom pressure, resulting in the need to solve integro-differential equations that are considerable complication and time-consuming. Therefore, the approximation of the phenomena by reduction of the horizontal pressure gradient by approximately 10% was applied. But the phase errors is resulted from the approximate SAL representation. It resulted in a relatively poor performance compared to some other tide models like Finite Element Solution (FES) (Carrere et al., 2013). However, a significant benefit of GTSM is its capability to provide global surge estimates. An application is a historic reanalysis of extreme sea levels (GTSR) which is produced with the combination of surge representation from GTSMv1.0 and tide representation from FES2012 (Muis et al., 2016).

In January 2017, GTSM was updated to version 2.0 including a full SAL implementation (Kuhlmann et al., 2011), the parameterized internal wave drag, the higher resolution for the steep depth, and the implementation of the below permanent ice-shelf seas in Antarctic (De Kleermaeker et al., 2017). Throughout 2017 and up to 2019, several improvements were included such as the increased resolution, updated bathymetry datasets and the inclusion of atmospheric tides. A reanalysis dataset derived from the GTSMv3.0 has been demonstrated as the successor of the GTSR (Muis et al., 2020). The main model used in our research is GTSMv3.0, and we give a brief description of it in this Chapter.

2.1.1 Governing Equations

GTSM is based upon the Delft3D Flexible-Mesh hydrodynamics code (Kernkamp et al., 2011). It uses a version of the barotropic shallow water equations in two dimensions (Irazoqui Apecechea et al., 2017). Unlike local models that are forced by open boundary conditions, there are no lateral boundaries for GTSM and tides are forced by a tide-generating potential. The governing equations are:

$$\begin{aligned} &\frac{\partial \boldsymbol{u}}{\partial t} + \frac{1}{h}(\nabla\cdot(h\boldsymbol{u}\boldsymbol{u}) - \boldsymbol{u}\nabla\cdot(h\boldsymbol{u})) + f\times\boldsymbol{u} \\ &= -g\nabla(\zeta-\zeta_{EQ}-\zeta_{SAL}) + \nabla\cdot(\nu(\nabla\boldsymbol{u}+\nabla\boldsymbol{u}^T)) + \frac{\tau_b+\tau_{IT}+\tau_s}{\rho h} \\ &\frac{\partial h}{\partial t} + \nabla(h\boldsymbol{u}) = 0 \end{aligned} \tag{2.1}$$

where h is the total water depth with the global distribution as Figure 2.1a, $\boldsymbol{u}$ represents the depth-averaged horizontal velocity vector, g is the gravitational acceleration, f is the Coriolis force, ρ is the density of water, ν is the horizontal eddy viscosity, ζ is the water level relative to a reference plane, ζ_{EQ} is the equilibrium tide. τ_s is the term related to the wind stress.

The term ζ_{SAL} refers to the self-attraction and loading effect (SAL), which is a phenomenon with a significant impact on the tidal dynamics especially at the global scale. It describes the effects of self-gravitation attraction and deformation of the ocean floor by the water column on top of it and associated changes to the geo-potential. SAL can change the tide amplitudes by approximately 10% or more and phases by 30 degrees (Kuhlmann et al., 2011). It can often be excluded in regional models but is a requirement in a global model. The SAL potential is included in the momentum equation similar to the tidal potential. The SAL term is calculated from the modelled water level at every time-step using a spherical harmonics approach. For a more detailed explanation, see (Irazoqui Apecechea et al., 2017).

The terms τ_b and τ_{IT} denote parameterization of the bottom friction stress and internal tide friction stress, respectively. They are the main drivers of the tide energy dissipation. The bottom friction is given by a quadratic friction law, the form is:

$$\tau_b = -C\rho g||\boldsymbol{u}||\boldsymbol{u} \tag{2.2}$$

where C is the bottom friction coefficient. There are several formulations for this coefficient, such as Chézy, Manning's friction or White-Colebrook formulation (Colebrook et al., 1937; Egbert & Ray, 2000; Manning et al., 1890). In GTSMv3.0, we use the Chézy formula and C is the constant coefficient with the value of $C_D = \sqrt{1/C} = 77(m^{1/2}s^{-1})$. Tide energy dissipation generated by the bottom friction is shown in Figure 2.1b. Blue boxes indicate the main regions with high dissipation and all of them are located in the coastal areas. The regions with the largest tidal dissipation are the Hudson Bay/Labrador, the European Shelf, and the North West of the Australia Shelf.

Moreover, a large amount of the global energy dissipation occurs through bottom stress in relatively localized regions with shallow water. Still, approximately 1 TW, which corresponds to 25 – 30% of the total global dissipation, occurs in the deep ocean through internal wave drag (Figure 2.1c). Therefore, tidal dissipation through internal wave drag has a great impact on the model and cannot be neglected for an accurate representation of tides. In GTSM, it is parameterized as the following equation (Maraldi et al., 2011):

$$\tau_{IT} = -C\rho k^{-1} N(\nabla h \cdot \boldsymbol{u})\nabla h \tag{2.3}$$

where C is the dimensionless coefficient, k is typical topography horizontal wave number, N is the depth-averaged Brunt-Väisälä frequency, and ∇h represents the bathymetry gradient. It was computed using data from the Copernicus marine global reanalysis GLORYS (Garric et al., 2017). In our application, $C_{IT} = Ck^{-1}$ is applied as the user-defined coefficient, with the value of 0.015. It was based on a global estimate of internal tide dissipation and reproduction of tides by the model.

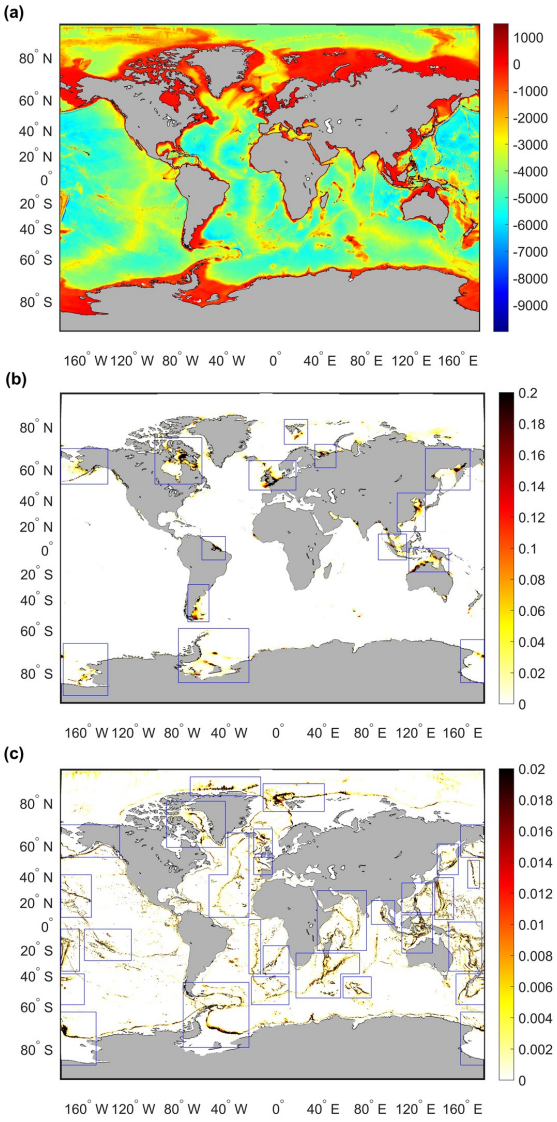

Figure 2.1: Spatial distribution of uncertain parameters. (a): Bathymetry [m]; (b): Tide energy dissipation by bottom friction in [W/m^2]; (c): Tide energy dissipation by internal tides friction. The areas with large tidal energy dissipation are shown in the areas with blue boxes.

2.1.2 Bathymetry

One of the most important parameters in tide modeling is bathymetry. In GTSMv3.0 the bathymetry is derived from the global products General Bathymetric Chart of the Oceans dataset (GEBCO). GEBCO is continually developing its bathymetry datasets to improve the accuracy and the coverage of measured ocean depth. Two versions of GEBCO dataset, GEBCO release 2014 and GEBCO 2019, are available. The comparison of model performance with these two datasets is performed to analyze their impact on tide forecast. GEBCO 2019 provides higher accuracy than the GEBCO 2014 (detailed analysis is in the Chapter 3). In this thesis, GTSMv3.0 with the bathymetry based on the GEBCO 2019 is used as the starting point.

The GEBCO 2019 is used as bathymetry input projecting to the unstructured grid of GTSM through interpolation. It provides global coverage with a 15 arc-second resolution grid of measured and estimated seafloor topography. For Europe, the EMODnet dataset with a resolution of about 250m is used to overwrite the bathymetry in those regions where there are regional bathymetry data available. All bathymetric data is assumed to be relative to the Lowest Astronomical Tide (LAT). Since GTSM uses Mean Sea level (MSL) as its vertical reference, a correction is applied for the LAT-MSL difference. However, even though the techniques developed in the submarine survey and depth are updated regularly, large regions remain still unsurveyed at a global scale. This has a significant impact on the tide reproduction, as we will show later.

2.1.3 Computational Grid

The tidal amplitudes are normally larger at the coast than that in the deep sea while the wave lengths are typically smaller. To model this accurately a high resolution is required in coastal areas, which may lead to a large computational cost. Here, we make use of an unstructured mesh with triangles and quadrilaterals, which makes it possible to provide a much higher resolution in coastal areas and lower resolution in the deep ocean to maintain acceptable computational cost (Kernkamp et al., 2011). Compared to the regular latitude-longitude grid, there are two advantages of the unstructured mesh. Firstly, grids in high latitudes are thinned to counteract the converging meridians. And secondly, some areas that require high resolution, such as coastal areas and continental shelves where much of the dissipation occurs, can be refined.

Two different resolutions of GTSMv3.0 were developed. They are described in Table 2.1 as GTSM with the coarse grid and GTSM with the fine grid. GTSM with coarse grid has a resolution of approximately 50km in the deep ocean and 5km near the coast. The largest grid cells in the fine version of GTSM are 25 km. In the coastal area, the resolution is 1.25km in Europe and 2.5km along coasts elsewhere. The number of grid cells is approximately 4.9 million and the coarse version has about 2 million cells (see Table 2.1).

As a result of efficient parallelization, a model simulation with the GTSM with the fine grid for a period of 45 days only takes approximately 10 hours on a computer with 20 cores, consisting of 5 Intel E3 processors with 4 cores each, and 3 hours for the same simulation for the coarse model. To further reduce the computing time, we moved the computations to the Dutch National Supercomputer Cartesius, where the running time for the same simulation on 200 cores reduced to 70 minutes for the fine model and 25

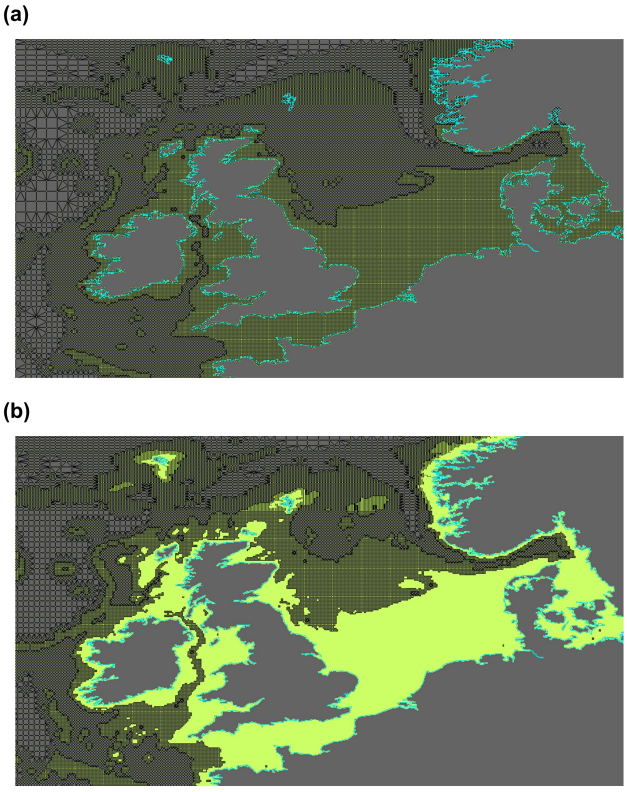

Figure 2.2: Computational grid around the European region (a): coarse grid; (b): fine grid.

Table 2.1: GTSM resolution and computational time for 45 days simulation in Dutch National Supercomputer Cartesius with 200 cores

Model	GTSM with the coarse grid	GTSM with the fine grid
Resolution	deep ocean:50km coastal region:5km;	deep ocean: 25km coastal Europe:1.25km other coastal region: 2.5km;
Cells	2 million	4.9 million
Computational time	25 minutes	70 minutes

minutes for the coarse model. For individual model runs this computing time is acceptable, but for parameter estimation which requires hundreds of model simulations, that will take weeks. Therefore, the parameter estimation scheme should be very efficient.

2.1.4 Surge Modelling

Sea level variation can be divided into tidal components and non-tidal components. The non-tidal component is the residual from the water level removing the regular tides. During storms, the highest water levels typically occur at a combination of tides together with effects from air pressure and surface winds. This additional contribution is usually called surges. In early research, researchers attempted to forecast storm surges by using of empirical relationships between meteorological fields and sea level to forecast the water level (Amin, 1982; Pugh & Woodworth, 2014; Rossiter, 1959). However, with the development of computing power, it is possible to model surge by the numerical tide and surge barotropic models. Surges are generated by the use of wind and air pressure fields as meteorological forcing. In GTSM, meteorological forcings are then applied as time and space varying wind and air pressure. The wind stress is modeled as the following equation:

$$\tau_s = \rho_a C_d ||\boldsymbol{u}_{10}|| \boldsymbol{u}_{10} \tag{2.4}$$

where ρ_a is the density of air, and $\boldsymbol{u}_{10}$ is the term of the wind speed 10 meters above the free surface. In the Charnock formulation (Charnock, 1955), the wind drag coefficient C_d is dependent on the wind speed $\boldsymbol{u}_{10}$ and a user-defined Charnock constant to represent the surface roughness, which is 0.041 in our model.

2.2 Parameter Uncertainty Analysis

The accuracy of global tide models has improved steadily over the past 20 years and the remaining uncertainties are now believed to be caused by the uncertainty of the input parameters (Lyard et al., 2021). For instance, although GTSM has been improved continuously from the perspective of physical process, resolution, and model inputs, over the past few years from version 1.0 to version 3.0, the uncertainties of the model output are still significant and further reduction of these uncertainties would benefit its applications. The main model errors occur in the simplification and parameterization of physical processes, numerical errors, and uncertainties of the model parameters. The first two types of errors are studied as part of ongoing modeling efforts with the model development. Parameter estimation is an approach to optimizing parameters that cannot be measured directly but does have a major influence on the accuracy of the model output. Parameter estimation is a process, whereby the difference between model results and the measurements is reduced by adjusting parameters. Here, we build upon the grid and parameterization of GTSMv3.0.

The main parameters affecting performance are different for the deep ocean with the bathymetry larger than 200m and the shallow waters. As we can observed from the Figure 2.1, bathymetry strongly varies in space (Figure 2.1a). Tide energy dissipation through internal tides friction is globally distributed and related to the bathymetry

change, especially in the mid-ocean ridges and trenches, continental shelves, and island chains (Figure 2.1c). Dissipation by the bottom friction has a much larger influence in the coastal areas (Figure 2.1b). Therefore, we aim to split the calibration into two stages. The first is calibration at the large scales in the deep ocean and the second is to refine the coastal regions with more measurements included locally. The sensitivity has to be analyzed before the estimation experiment.

2.2.1 Parameters to Estimate in the Deep Ocean

Considering the dominant physical processes, we expect that bathymetry and internal tide friction are two main parameters in the deep ocean that affect the model-derived tide representation. We performed a simple experiment to analyze their sensitivity with the comparison of observations. Sensitivity can be analyzed by perturbing single parameters and comparing the relative changes of the cost function to the initial parameters. The cost function is defined as the sum of squares of the difference between the model output and observation, with the formula:

$$J(x) = \frac{1}{2}[y - H(x)]^T R^{-1}[y - H(x)] \tag{2.5}$$

where y is the field observation vector including all times and stations, and the term x is the parameter vector. $H(x)$ is the model output matching the observation locations and times, and R is the observation error covariance. Observations we used are 1973 evenly distributed time series, restricted to deep water, derived from the FES2014 dataset. Because FES2014 represents only tides and not surge, we run GTSM also with only tide forcing included.

We divided the global ocean into seven regions as perturbed parameters to compare the influence of bathymetry and internal tides friction. Parameter in one region is perturbed with one factor, which is the uncertainty of that parameter. For the uncertainty of bathymetry, we select a standard deviation of 5%. Bathymetry is considered uncertain here because only a fraction of the ocean seabed has been surveyed, and the remaining errors are significant. Tozer et al. (2019) mentioned an estimate uncertainty of 150m for deep water and 180m between coastlines and the continental rise for the SRTM15+ dataset. Weatherall et al. (2015) showed in their Figure 6 the percentage of bathymetry changes between GEBCO_2014 and GEBCO_08 (GEBCO 2010 release) grids in the North Sea region with differences of over 5% or even 10% in many places. Moreover, to make the sensitivity test results comparable, we define the 20% perturbation for the internal tides coefficient C_{IT}. The sensitivity is defined as the relative changes of the cost function between the initial model and the model with perturbed parameters. The value of sensitivity with respect to bathymetry (Figure 2.3a) ranges up to 25%. This value is greatly larger than that in internal tides with the value of 3.2% (Figure 2.3b). It means that for these levels of uncertainty, GTSM is more sensitive to bathymetry than to internal tides friction. Selecting only the dominating parameter in the model and ignoring others effectively reduce the parameter dimensions. Therefore, bathymetry is the only type of parameter we selected to estimate for the deep ocean.

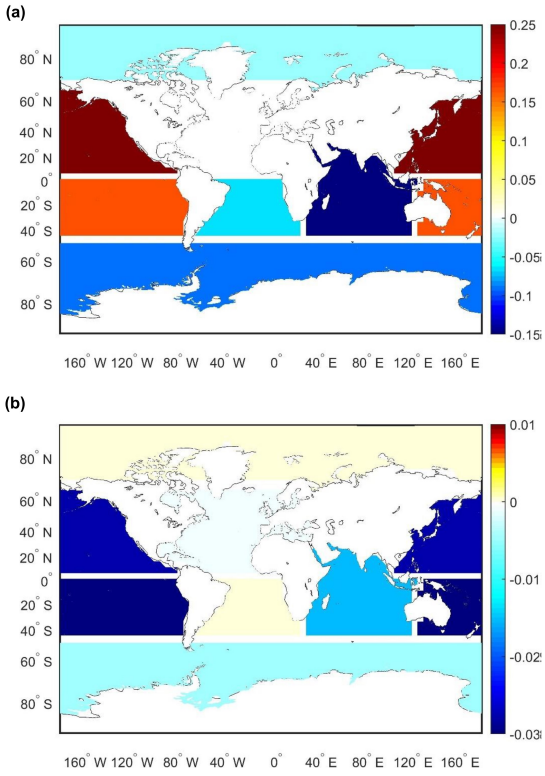

Figure 2.3: Relative changes of cost function between the initial model and the model with perturbed parameter for each region. (a) 5% perturbation is performed to bathymetry in each domain separately. (b) 20% perturbation is performed to internal tides in each domain separately.

2.2.2 Parameters to Estimate in the Shallow Waters

There is no doubt that the bottom friction coefficient is the critical parameter for the accurate simulation of water level in the shallow water (Egbert & Ray, 2001; Fan et al., 2019; Sana & Tanaka, 1997). In coastal water, depths are usually small and tides are often large, which results in much larger bottom friction than in deep water. However, the coefficient is empirically defined (Ludwick, 1975). It affects the model forecast through the generation of energy dissipation and is vital to estimate (Arora & Bhaskaran, 2012). Many parameter estimation applications to regional barotropic tide models are performed to estimate the bottom friction coefficient (Howarth & Souza, 2005; Ludwick, 1975; Xu et al., 2017). We select 20% as the standard deviation of uncertainty for the bottom friction.

The sensitivity of the bottom friction coefficient is related to the tide energy dissipation, as shown in Figure 2.1b, as well as depends on the observation locations we compared. For example, Figure 2.4 reports spatial distribution of Root Mean Square Difference between the initial model and model with perturbed bottom friction coefficient.

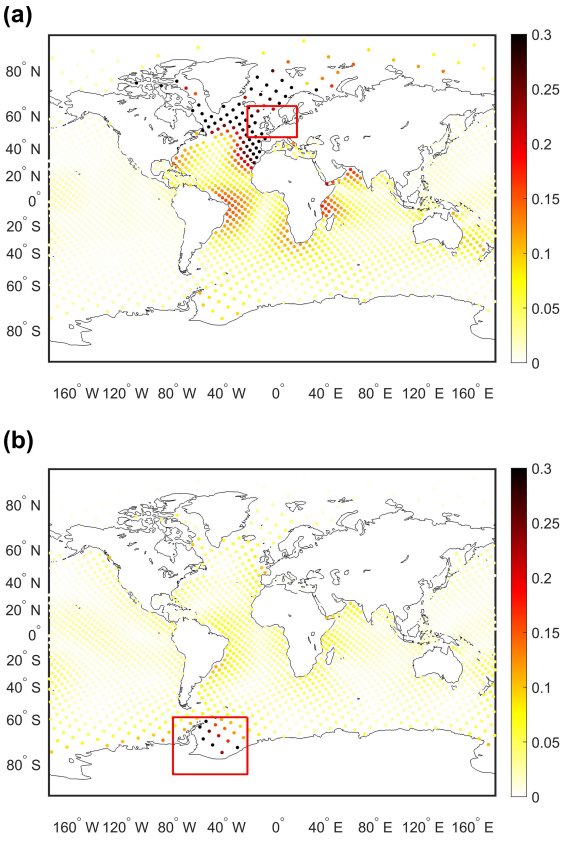

Figure 2.4: RMS of the difference between initial model and model with perturbed bottom friction in the European Shelf (a) and southern ocean (b) in [m]. Bottom friction coefficients in the red boxes are perturbed with 20%. Outside the red box, the bottom friction coefficient is same as the initial model with the constant value shown in Eq. (2.3). Observations are from FES2014 dataset.

Perturbation in the European Shelf (Figure 2.4a) has larger effect to model performance than perturbing part of the southern ocean (Figure 2.4b). This is the same reaction related to the tide energy dissipation distribution. In addition, model performance is significantly affected in the region nearby with bottom friction changes and smaller when it is far away. This will be more obvious if we have more local observations, such as tide gauge data. However, tide gauge data in the shallow water is spatial-sparse distributed globally. Therefore, the detailed analysis related to bottom friction will be performed after the observation analysis in the shallow water, see detailed information in Chapter 5. But we can conclude that the accurate estimation of bottom friction coefficient is vital to the model performance in shallow waters.

In summary, we identify two parameters to estimate, bathymetry for the global deep ocean and bottom friction coefficient for the shallow water. We try to come up with a

two-step strategy for the estimation. The first step is to pay attention to the deep ocean estimation of bathymetry, after that bottom friction coefficient is calibrated in the second stage.

2.3 Conclusions

In this Chapter, we introduce the tide and surge model GTSMv3.0. Parameter error is analyzed from the physical process perspective and by sensitivity test comparison. The deep ocean and shallow water are separately discussed due to the difference of uncertain parameters. Finally, bathymetry and bottom friction coefficient are selected as two parameters for estimation and we propose a tentative strategy for the calibration started from the large scale tidal propagation in the deep ocean (chapters 3 and 4) and continuous with the bottom friction coefficient estimation (Chapter 5).

Bibliography

Amin, M. (1982). On analysis and forecasting of surges on the west coast of Great Britain. *Geophysical Journal International*, *68*(1), 79–94. https://doi.org/10.1111/j.1365-246X.1982.tb06963.x

Arora, C., & Bhaskaran, P. K. (2012). Parameterization of bottom friction under combined wave-tide action in the hooghly estuary, india. *Ocean Engineering*, *43*, 43–55. https://doi.org/https://doi.org/10.1016/j.oceaneng.2011.12.018

Carrere, L., Lyard, F., Cancet, M., Guillot, A., & Roblou, L. (2013). FES 2012: A New Global Tidal Model Taking Advantage of Nearly 20 Years of Altimetry. *20 Years of Progress in Radar Altimatry*, *710*, Article 13, 13.

Charnock, H. (1955). Wind-stress on a water surface. *Quarterly Journal of the Royal Meteorological Society*, *81*(350), 639–640. https://doi.org/10.1002/qj.49708135027

Colebrook, C. F., White, C. M., & Taylor, G. I. (1937). Experiments with fluid friction in roughened pipes. *Proceedings of the Royal Society of London. Series A - Mathematical and Physical Sciences*, *161*(906), 367–381. https://doi.org/10.1098/rspa.1937.0150

De Kleermaeker, S., Verlaan, M., Mortlock, T., Rego, J. L., Apecechea, M. I., Yan, K., & Twigt, D. (2017). Global-to-local scale storm surge modelling on tropical cyclone affected coasts. *In: Australasian coasts ports 2017: Working with nature. barton, act: Engineers australia, pianc australia and institute of professional engineers new zealand, 2017: 358-364*. https://search.informit.org/doi/10.3316/informit.934516484243698

Egbert, G. D., & Ray, R. D. (2000). Significant dissipation of tidal energy in the deep ocean inferred from satellite altimeter data. *Nature*, *405*(6788), 775–778. https://doi.org/10.1038/35015531

Egbert, G. D., & Ray, R. D. (2001). Estimates of m2 tidal energy dissipation from topex/ poseidon altimeter data. *Journal of Geophysical Research: Oceans*, *106*(C10), 22475–22502. https://doi.org/https://doi.org/10.1029/2000JC000699

Fan, R., Zhao, L., Lu, Y., Nie, H., & Wei, H. (2019). Impacts of currents and waves on bottom drag coefficient in the east china shelf seas. *Journal of Geophysical Research: Oceans*, *124*(11), 7344–7354. https://doi.org/https://doi.org/10.1029/2019JC015097

Garric, G., Parent, L., Greiner, E., Drévillon, M., Hamon, M., Lellouche, J.-M., Régnier, C., Desportes, C., Le Galloudec, O., Bricaud, C., Drillet, Y., Hernandez, F., & Le Traon, P.-Y. (2017). Performance and quality assessment of the global ocean

eddy-permitting physical reanalysis GLORYS2V4. *EGU General Assembly Conference Abstracts*, 18776.

Howarth, M., & Souza, A. (2005). Reynolds stress observations in continental shelf seas [Observations and modelling of mixed layer turbulence: Do they represent the same statistical quantities?]. *Deep Sea Research Part II: Topical Studies in Oceanography*, *52*(9), 1075–1086. https://doi.org/https://doi.org/10.1016/j.dsr2.2005.01.003

Irazoqui Apecechea, M., Verlaan, M., Zijl, F., Le Coz, C., & Kernkamp, H. (2017). Effects of self-attraction and loading at a regional scale: A test case for the northwest european shelf. *Ocean Dynamics*, *67*(6), 729–749. https://doi.org/10.1007/s10236-017-1053-4

Kernkamp, H., Van Dam, A., Stelling, G., & de Goede, E. (2011). Efficient scheme for the shallow water equations on unstructured grids with application to the Continental Shelf. *Ocean Dynamics*, 1–14. https://doi.org/10.1007/s10236-011-0423-6

Kuhlmann, J., Dobslaw, H., & Thomas, M. (2011). Improved modeling of sea level patterns by incorporating self-attraction and loading. *Journal of Geophysical Research: Oceans*, *116*(C11). https://doi.org/10.1029/2011JC007399

Ludwick, J. C. (1975). Variations in the boundary-drag coefficient in the tidal entrance to chesapeake bay, virginia. *Marine Geology*, *19*(1), 19–28. https://doi.org/https://doi.org/10.1016/0025-3227(75)90003-1

Lyard, F. H., Allain, D. J., Cancet, M., Carrère, L., & Picot, N. (2021). Fes2014 global ocean tide atlas: Design and performance. *Ocean Science*, *17*(3), 615–649. https://doi.org/10.5194/os-17-615-2021

Manning, R., Griffith, J. P., Pigot, T., & Vernon-Harcourt, L. F. (1890). *On the flow of water in open channels and pipes*.

Maraldi, C., Lyard, F., Testut, L., & Coleman, R. (2011). Energetics of internal tides around the kerguelen plateau from modeling and altimetry. *Journal of Geophysical Research: Oceans*, *116*(C6). https://doi.org/10.1029/2010JC006515

Muis, S., Apecechea, M. I., Dullaart, J., de Lima Rego, J., Madsen, K. S., Su, J., Yan, K., & Verlaan, M. (2020). A high-resolution global dataset of extreme sea levels, tides, and storm surges, including future projections. *Frontiers in Marine Science*, *7*, 263. https://doi.org/10.3389/fmars.2020.00263

Muis, S., Verlaan, M., Winsemius, H., Aerts, J., & Ward, P. (2016). A global reanalysis of storm surges and extreme sea levels. *Nature Communications*, *7*, 1–12. https://doi.org/10.1038/ncomms11969

Pugh, D., & Woodworth, P. (2014). *Sea-level science: Understanding tides, surges, tsunamis and mean sea-level changes*. Cambridge University Press.

Rossiter, J. R. (1959). Research on methods of forecasting storm surges on the east and south coasts of great britain. *Quarterly Journal of the Royal Meteorological Society*, *85*(365), 262–277. https://doi.org/https://doi.org/10.1002/qj.49708536508

Sana, A., & Tanaka, H. (1997). Improvement of the full-range equation for bottom friction under three-dimensional wave-current combined motion. *Coastal Engineering*, *31*(1), 217–229. https://doi.org/https://doi.org/10.1016/S0378-3839(97)00007-0

Tozer, B., Sandwell, D. T., Smith, W. H. F., Olson, C., Beale, J. R., & Wessel, P. (2019). Global bathymetry and topography at 15 arc sec: Srtm15+. *Earth and Space Science*, *6*(10), 1847–1864. https://doi.org/https://doi.org/10.1029/2019EA000658

Verlaan, M., De Kleermaeker, S., & Buckman, L. (2015). GLOSSIS: Global storm surge forecasting and information system [online]. *Australasian Coasts & Ports Conference 2015: 22nd Australasian Coastal and Ocean Engineering Conference and the 15th Australasian Port and Harbour Conference.*, 229–234.

Wang, X., Verlaan, M., Apecechea, M. I., & Lin, H. X. (2021). Computation-efficient parameter estimation for a high-resolution global tide and surge model. *Journal of Geophysical Research: Oceans*, *126*(3), e2020JC016917. https://doi.org/https://doi.org/10.1029/2020JC016917

Weatherall, P., Marks, K. M., Jakobsson, M., Schmitt, T., Tani, S., Arndt, J. E., Rovere, M., Chayes, D., Ferrini, V., & Wigley, R. (2015). A new digital bathymetric model of the world's oceans. *Earth and Space Science*, *2*(8), 331–345. https://doi.org/10.1002/2015EA000107

Xu, P., Mao, X., & Jiang, W. (2017). Estimation of the bottom stress and bottom drag coefficient in a highly asymmetric tidal bay using three independent methods. *Continental Shelf Research*, *140*, 37–46. https://doi.org/https://doi.org/10.1016/j.csr.2017.04.004

Chapter 3

Computation-efficient Parameter Estimation for GTSM

In this Chapter, a computation-efficient parameter estimation scheme for high-resolution global tide and surge models is developed and applied to the GTSMv3.0. The estimation algorithm uses an iterative least-squares method, known as DUD. We use time-series derived from the FES2014 tidal database in the deep ocean as observations to estimate corrections to the bathymetry. Although the model and estimation algorithm run in parallel, directly applying of DUD would not be affordable computationally. To reduce the computational demand, a coarse-to-fine strategy is proposed by using output from a coarser model to replace the fine model. There are two approaches; One is completely replacing the fine model with a coarser model during calibration (Coarse Calibration) and the second is Coarse Incremental Calibration, that replaces the output increments between the initial model and model with modified parameters by coarser grid model simulations. To further reduce the computation time, the parameter dimension is reduced from $O(10^6)$ *to* $O(10^2)$ *based on sensitivity analysis, which greatly reduces the required number of model simulations and storage. In combination, these methods form an efficient optimization strategy. Experiments show that the accuracy of the tidal representation can be improved significantly at affordable cost. Validation for other time-periods and using coastal tide-gauges shows that the accuracy is improved significantly. However, the calibration period of two weeks is short and leads to some over-fitting of the model.*

Parts of this chapter have been published in Wang et al. (2021):

Wang, X., Verlaan, M., Apecechea, M. I., and Lin, H. X. (2021). Computation-efficient parameter estimation for a high-resolution global tide and surge model. Journal of Geophysical Research: Oceans, 126, e2020JC016917.

3.1 Introduction

Parameter estimation started from the first stage, estimating bathymetry in the deep ocean because generally tidal propagation scale in deep ocean is larger than it in shallow waters and we assume that once the large scales for deep ocean are properly calibrated the finer details for coastal regions can be refined in later studies. Bathymetry is selected as the first type of parameter to calibrate based on the sensitivity analysis results shown in Chapter 2. A derivative-free calibration algorithm DUD (Does not use derivative), proposed by Ralston and Jennrich (1978) is available in OpenDA software (*OpenDA User Documentation*, 2016). It is applied to minimize the cost function by comparing the model predictions with data from the FES2014 dataset and iteratively computing increasingly accurate estimations of the model states. Tide gauge data from the UHSLC dataset is used for the model validation.

In this study, we developed a parameter estimation scheme for the high-resolution GTSM. Compared to regional models, a global model covers a much larger area and does not have open boundaries. As a result of these differences, a global tide model has quite different challenges from regional tide models. One of which is that changes to the bathymetry can have effects very far away from the region of the parameter changes. The high computational complexity and storage usage is also a challenge for the high-resolution global model calibration. On the one hand, computer memory may be insufficient to contain the relevant model output for a long simulation; the memory required increases rapidly with the number of parameters and with the number of observations. On the other hand, computing time is very long for calibration of a high-resolution global model even though parallel processing can be applied. For the DUD optimization algorithm, the computing times are roughly proportional to the number of parameters to be estimated. Thus, the reduction in the number of parameters and reduction in the computing time per model simulation plays an essential role in effective parameter estimation. Therefore, the parameter estimation scheme should be computation-efficient with low computational cost and small memory usage. We improve the computation efficiency of parameter estimation in two key aspects. First, a coarse-to-fine strategy is proposed to replace the model with a coarser grid for parameter estimation. Second, a large reduction in parameter dimension is achieved via sensitivity tests.

Chapter 3 is organized as follows. The parameter estimation scheme is described in Chapter 3.2, including a description of the observations used, as well as the coarse-to-fine parameter estimation approaches. Chapter 3.3 shows the sensitivity analysis for the parameter dimension reduction and the parameter estimation results. Validation of the calibrated model is given in Chapter 3.4. Finally, the discussion and conclusions follow in Chapter 5.6.

3.2 Parameter Estimation Scheme

3.2.1 Observation Network

The datasets applied for parameter estimation and validation in this study are deep ocean tides from the FES2014 dataset and the tide gauge data from the University of

Hawaii Sea Level Centre (UHSLC) (Caldwell & Thompson, 2015).

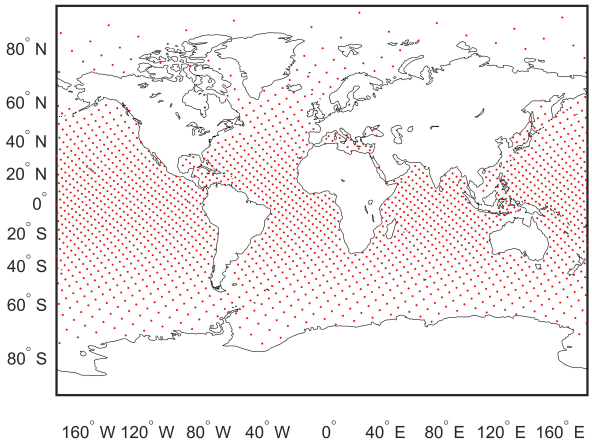

Figure 3.1: Observation locations: 1973 time series from the FES2014 dataset.

The main advantage of using a tidal database such as FES2014 for our deep ocean calibration is that a tide time series can be obtained for arbitrary time periods globally. With direct use of satellite altimetry one would have to cover a much longer time span, due to the relatively long repeat cycle, e.g. 12 days for Sentinel 1. We generated 1973 time series from the FES2014 dataset with 32 tide constituents (excluding long-term constituents SA and SSA) for the calibration of bathymetry in January 2014 with a 10-minute time step. To obtain equally-spaced observation points, firstly, we generated 3000 equally-spaced points on a sphere using Fibonacci and latitude-longitude lattices method (González, 2009), and then we removed the locations on land and in shallow waters with depth smaller than 200m, which finally results in 1973 locations for deep ocean. The observation locations are shown in Figure 3.1.

We retrieved the 283 tide gauge series from the UHSLC dataset that are available from the hourly research quality dataset in the year 2014. Firstly, we separated tide and surge from the measured water level and performed the tide analysis by software TIDEGUI, since our model calibration is based on the tide representation only. Secondly, because the simulation time window for the parameter estimation covers only a short time period, the (solar) annual and semiannual constituents SA and SSA were removed after the tide analysis. We obtained a set of 93 harmonic constituents. After that, the tide and surge representations were visually inspected in comparison to the measured series in the tide analysis procedure. The distribution of the locations is somewhat irregular and most locations are in coastal areas.

Even though the FES2014 dataset has assimilated tide gauge data, the UHSLC dataset can still be seen as independent from our calibration because the FES data used for calibration was limited to deep water, while almost all tide gauges are at the coast. The purpose of using the UHSLC data is to study the impact of the calibration in the coastal

areas.

3.2.2 Parameter Estimation Algorithm

Parameter uncertainty can be reduced via optimization techniques to tune the model output towards the data. Here we use an algorithm called DUD, since it is the default algorithm in the generic data-assimilation toolbox OpenDA and there is a lot of experience with this method. DUD is an algorithm similar to Gauss-Newton algorithm but with a derivative-free method to solve non-linear least squares problems. The algorithm attempts to minimize a cost function in an iterative manner. A brief flow chart of the parameter estimation scheme is shown in Figure 3.2.

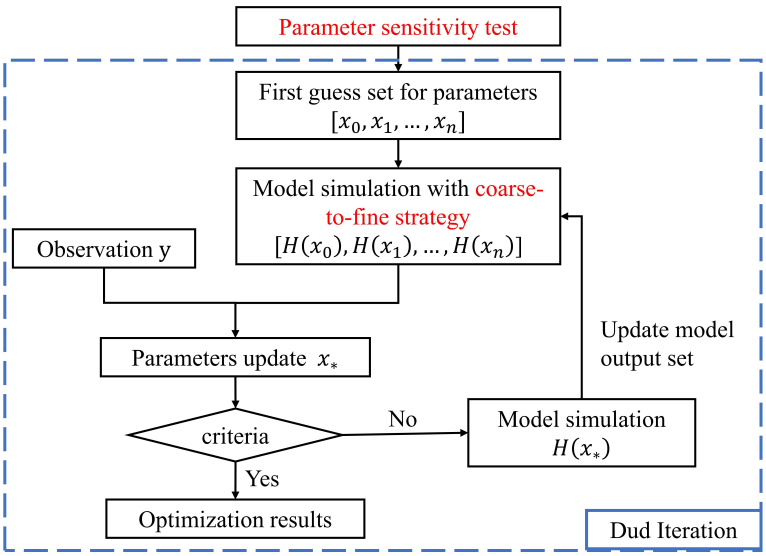

Figure 3.2: Flow chart of parameter estimation scheme

In addition to an observation term, the cost function also contains a weak-constraint or background term in order to constrain changes compared to the initial parameters where the fit to observations does not improve significantly. In the brief description of the DUD algorithm below, the cost function is limited to the observation term only, to keep the description concise. The observation term $J_o(x)$ in the cost function measures the difference between the model output and observations in a time range $t \in [t_1, t_{N_t}]$, which is:

$$J_o(x) = \frac{1}{2}[y - H(x)]^T R^{-1}[y - H(x)] \tag{3.1}$$

where y is the observation vector including all times $t \in [t_1, t_{N_t}]$ and stations $(1, \ldots, N_s)$, and the term x is the parameter vector with the number n. $H(x)$ is the model output

matching the observation locations and times and R is the observation error covariance. The dimension of y and $H(x)$ is $O(N_s N_t)$. The minimization processes are performed with the following steps:

1. Obtain model output $H(x_i)$ with the first guess for all parameters $x_0 = x_b$, as well as n runs each with one perturbed parameter ($x_1 = x_b + \delta e_1, \ldots, x_n = x_b + \delta e_n$).
2. Calculate the cost function $J_o(x_i), i = 0, \ldots, n$ for the $n+1$ simulations.
3. Perform the iterations of the minimization process.
   (a) Reorder the cost function values from the largest value to the smallest as $J_o(x_0) \geq J_o(x_1) \geq \ldots\ldots \geq J_o(x_n)$.
   (b) Create an approximate linear model by interpolation between the $n+1$ model predictions already computed. The linearization equation is:
   $$H(x) \approx H(x_n) + M\Delta(x - x_n) \tag{3.2}$$
   with $M = FP^{-1}$, where the i^{th} column of F and P are $F_i = H(x_i) - H(x_n)$, $P_i = x_i - x_n$
   (c) Solve the linear problem and update the new parameters by:
   $$x_* = x_n + [M^T M]^{-1} M^T [y - H(x_n)] \tag{3.3}$$
   (d) If $J_o(x_*) < J_o(x_n)$, update the parameters and cost function set by using x_* to replace x_0 which has the highest cost function, i.e. we keep the $n+1$ best estimates.
   (e) Otherwise, do a line search until the cost function is improved. Update the parameters in the same way as shown in step (3d).
4. Check the termination criteria in steps (3d) and (3e); if the results do not satisfy any one of the criteria, then return to step (3a), otherwise stop the iterations.

Several constraints are imposed to make the correction factors realistic. One is the weak constraint applied as a background term in the cost function which will reduce the parameter adjustments when the fit to the observations does not improve significantly. Another is we added a hard constraint to all the parameters by limiting changes to 10%. This is because the initial number of simulations in step 1 is $n+1$ and the dimension of matrix M is $N_s N_t \times n$. The computational time increases proportionally to the number of model simulations and running time for each simulation. The parameter dimension has a major impact on the number of simulations and a higher model resolution also increases the computational time for each model simulation. It results in the memory required to store the matrix M ultimately turning out to be a limiting factor in our application. Therefore, we propose two further approximations to speed up the computations and limit the use of memory. Firstly, we propose a coarse-to-fine parameter estimation scheme to reduce the computational time for each simulation in Chapter 3.2.3. Secondly, the parameter dimension is reduced to an acceptable scale by sensitivity analysis, which will be introduced in Chapter 3.3.2.

3.2.3 Coarse-to-fine Parameter Estimation

In this Chapter, two approaches for the coarse-to-fine parameter estimation strategy are proposed that replace part of the simulations with the fine grid GTSM by simulations with a coarser grid. The estimated parameters for the coarse model are reused for the fine model. Two possible approaches are:

1. Approach 1: Coarse Calibration, which completely replaces the fine model with a coarser grid model during the calibration.

2. Approach 2: Coarse Incremental Calibration, which replaces the increments between the output from the initial model and the model with modified bathymetry using a coarser grid. The bias between the coarse model and the fine model is corrected for.

The cost function for Approach 1 is:

$$J_1(x) = \frac{1}{2}[y - H_c(x)]^T R^{-1}[y - H_c(x)] \tag{3.4}$$

where the term $H_f(x)$ and $H_c(x)$ are the model output of the fine and coarse resolution, respectively. In Approach 1, the model simulation runs only on the coarse grid, which results in a large reduction in computational time. However, the minimization of the cost function only involves the coarse model without any direct relationship to the fine model. Since a coarser model is in general less accurate this will lead to a compensation for these errors in the parameter estimates, which still apply to the fine model.

Therefore, we also propose a second approach (Approach 2: Coarse Incremental Calibration) that only replaces the difference between the initial output and the adjusted model output of the fine model. Courtier et al. (1994) firstly proposed an incremental formula to reduce the computational cost of 4D-Var which is widely used in the implementation of data-assimilation for the ECMWF weather model. In our application, the Coarse Incremental Calibration is proposed based on the incremental formula replacement by the coarser grid. Starting from the initial parameters x_b, $H_c(x_b)$ and $H_f(x_b)$ are initial output with the fine and coarse grid without any perturbation. The difference between the initial and adjusted model output of these two resolutions δH_f and δH_c are:

$$\delta H_f = H_f(x) - H_f(x_b), \quad \delta H_c = H_c(x) - H_c(x_b) \tag{3.5}$$

Experiment shows that the difference between increments of coarse grid δH_f and δH_c is on average small compared to the RMS of δH_f and δH_c, 0.68cm compared to 3.26cm (not shown here). Therefore, the increments of fine grid in most regions are well represented by the coarse grid. We assume $\delta H_f \approx \delta H_c$, thus the output of fine GTSM can also be represented as:

$$H_f(x) \approx H_f(x_b) - H_c(x_b) + H_c(x) \tag{3.6}$$

Therefore, a new cost function is generated as:

$$J_2(x) = [y - H_f(x_b) + H_c(x_b) - H_c(x)]^T R^{-1}[y - H_f(x_b) + H_c(x_b) - H_c(x)] \tag{3.7}$$

The new cost function for initial simulation in Approach 2 represents the disagreement between the observations and the fine model predictions. Compared to Approach 1, the new cost function gives a better description of the initial fine model. The computational times of these two approaches are reduced and are almost the same since only one more simulation of the fine model is required in Approach 2. After the estimation, the correction factors of bathymetry are interpolated to the fine model's unstructured grid before simulations with the fine grid.

3.3 Numerical Experiments and Results

This chapter first provides more detail on how the calibration was performed. Next, it explains how we reduced the number of parameters to make the computation times and memory usage manageable. Finally, it describes the results from the calibration experiments.

3.3.1 Experiment Set-up

As discussed in Chapter 3.2.1, the accuracy of the model will be expressed relative to time-series computed from FES2014. Direct use of altimeter data to calibrate the model would require a simulation covering at least several years, which is not feasible computationally in this context. In our experience, time-series from tide gauges should cover between a month and a year to obtain accurate tidal estimates. Unfortunately, it turned out that this did not fit into the memory (32GB) on our cluster. One spring-neap cycle, of about half a month, did fit into the memory and was selected as the best feasible option at this point. The tidal potential used in the model accounts for the tide components with a Doodson number ranging from 57.565 to 375.575. The minimum threshold for the amplitude of the tidal spherical harmonic is 0.03m, which results in a set of 58 tidal generating frequencies. Long-period tide constituents SSA and SA are excluded from the model output and observations, because long-period tides are affected by non-gravitational influences. From the tidal constituents in FES2014 the time-span is not limited to a particular period. Therefore, we selected January 2014, when the most tide gauges were available for validation.

The simulation time is chosen from 1 to 14 January 2014 and the spin-up time for the model is from two weeks before 1 January to make sure that the initial values (zeros) for the sea level and currents no longer have a significant impact on the results. Each time-series, with a time-step of 10 minutes thus has a length of $N_t = 2016$. In total $N_s = 1973$ locations were selected, resulting in an output of $N_s * N_t = 3977568$ values per simulation.

3.3.2 Sensitivity Analysis and Parameter Dimension Reduction

In order to obtain a better initial bathymetry input for GTSM, a comparison of model simulations with bathymetry input from GEBCO release 2014 and GEBCO 2019 was performed.

Table 3.1 shows the RMSE, bias, and standard deviation (SD) for the two grid resolutions and two bathymetry inputs against the time series from FES2014 for seven regions from 1 to 14 January, 2014. The bias between the model output and observations is very small with the maximum value at the millimeter level. It illustrates that the tides computed with the fine grid are more accurate than for the coarse grid using the same bathymetry source in terms of RMSE and SD. Moreover, the model output with GEBCO 2019 bathymetry is more accurate than that with GEBCO 2014. This shows that reducing the uncertainty of bathymetry can significantly improve the model performance. Based on these experiments, we selected GEBCO 2019 as the source for the initial bathymetry.

In principle the bathymetry can be different in every grid node of the model. However, it would be computationally infeasible to treat the bathymetry at every grid node as a degree of freedom in the estimation. Moreover, the content of the information contained in the observations is not enough to estimate so many parameters.

Thus, we attempt to reduce the number of parameters and use a single value to adjust the bathymetry with one correction factor per spatial region $S_i, i = 1, \ldots, n$. For every grid node j in the spatial region we adjust the parameter from D_j to D_j^* according to:

$$D_j^* = (1 + [x]_i) D_j \; for \; j \in S_i \tag{3.8}$$

where $[x]_i$ is the i^{th} element of the reduced parameter vector x and we use the initial estimate $x_b = 0$ (a vector with n zeroes). For instance, if $[x]_1 = 0.10$, the depth in region S_1 will be increased by 10%. In GTSM the number of grid nodes is $O(10^6)$, while the feasible number of independent parameters during the estimation is $O(10^2)$. Thus, we would like to design $O(10^2)$ regions or sub-domains where the response of the model is expected to be similar and the sum of the sensitivities between the regions is of similar magnitude.

Let us first define the sensitivity s_i with respect to region S_i as

$$s_i = \frac{J(x_b + \delta e_i) - J(x_b)}{J(x_b)} \tag{3.9}$$

which is the relative change of cost function when changing the parameter only in the i^{th} region by multiplication with a factor $1 + \delta$.

Spatial Scale

Before the final selection of sub-domains for calibration, we first attempt to create a rough estimate of the spatial length-scale at which one can estimate the bathymetry from the available tidal data. Consider for example the constituent M_2, which is dominant in many places around the world. Figure 3.3a gives an impression of the amplitude of M_2 around our planet. The largest amplitudes are often in coastal areas. The color scale is limited to 1.4m, but there are a few regions where the amplitude is larger.

Now consider the following thought experiment. When the tide propagates from one location to another, a perturbation of the bathymetry between these positions could lead to a water level difference. The water level that arrives by propagation with speed c from a position at distance l can be described as:

$$H(t) = A\cos(\omega(t - \frac{l}{c})) \tag{3.10}$$

Table 3.1: Regional RMSE, bias and SD between model predictions with different bathymetry for two resolutions and the FES2014 data in [cm] from 1 to 14 January, 2014.

Model	GTSM with the coarse grid						GTSM with the fine grid					
Bathymetry	GEBCO 2014			GEBCO 2019			GEBCO 2014			GEBCO 2019		
Region	RMSE	Bias	SD	RMSE	Bias	SD	RMSE	Bias	SD	RMSE	Bias	SD
Arctic Ocean	7.03	0.37	7.02	7.06	0.44	7.04	5.25	0.41	5.22	5.24	0.65	5.18
Indian Ocean	7.94	-0.06	7.94	6.70	-0.11	6.70	6.51	-0.05	6.51	5.57	-0.10	5.57
North Atlantic	8.9	-0.02	8.96	6.89	0.01	6.87	7.89	0.03	7.89	5.41	0.07	5.41
North Pacific	7.41	-0.13	7.41	6.97	-0.12	6.96	6.03	-0.09	6.02	5.69	-0.07	5.69
South Atlantic	5.45	-0.22	5.45	4.76	-0.22	4.76	4.68	-0.20	4.67	4.15	-0.23	4.14
South Pacific	7.59	-0.20	7.58	7.03	-0.21	7.03	5.81	-0.19	5.80	5.57	-0.25	5.56
Southern Ocean	5.86	0.01	5.86	5.35	-0.02	5.34	4.47	-0.09	4.47	4.28	-0.13	4.27
Total	7.28	-0.09	7.27	6.47	-0.10	6.46	5.88	-0.09	5.88	5.23	-0.11	5.22

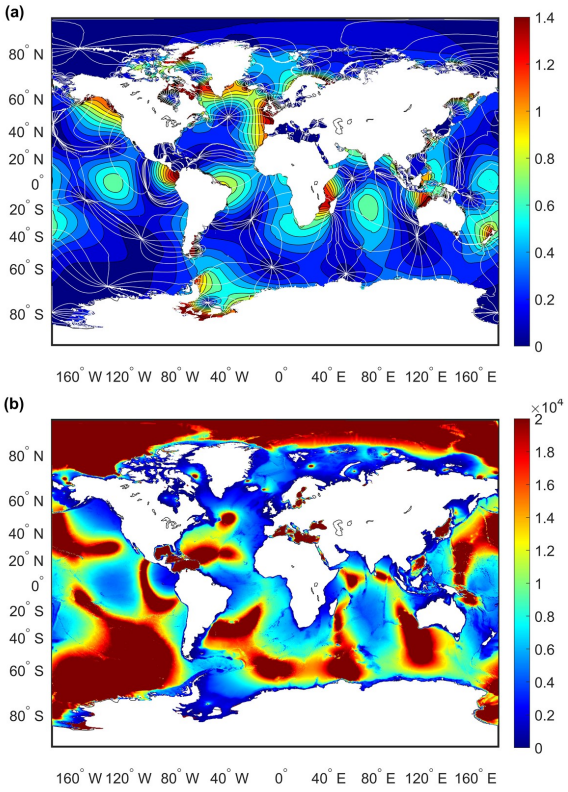

Figure 3.3: (a) Amplitude and cophase lines of M_2 constituent [m]; (b) propagation length based on perturbed bathymetry with M_2 constituent [km]

where l is the propagation length, A and ω denote the amplitude and frequency of M_2 constituent respectively. $H(t)$ is the water level at time t. If the bathymetry is perturbed between these points, this will affect the propagation speed $c = \sqrt{gD}$ and the difference of M_2 tide will be:

$$\Delta H(t) \approx A \sin(\omega(t - \frac{l}{c})) \frac{\omega l g \Delta D}{2c^3} \tag{3.11}$$

To really observe this difference, the change in tide should be larger than the noise in the measurements. Thus for observations with noise σ (standard derivation) one can give a minimum length scale over which changes in bathymetry $\Delta D = \alpha D$ may become visible in the observations:

$$l_c = \frac{2\sigma c^3}{A\omega g \Delta D} = \frac{2\sigma\sqrt{gD}}{\alpha A \omega} \tag{3.12}$$

The propagation length-scale l_c is inversely proportional to the M_2 amplitude and proportional to the square-root of the depth. It is expected that a small M_2 amplitude and a large value of bathymetry lead to a long propagation length and weak sensitivity.

Figure 3.3b provides an overview of propagation length at the global scale with $\sigma = 0.05m$ and 10% perturbation of bathymetry. Small values of propagation length illustrate the larger sensitivity of bathymetry corresponding to M_2 constituents. From this figure, one can conclude that it is probably difficult to estimate the bathymetry corrections for the Arctic and parts of the interior of many oceans, while conditions are much more favorable along the coasts and in shallow areas. The values of l_c should not be taken too literally, since the underlying formulas are only a rough approximation of the dynamics and the estimates for measurement noise and bathymetric uncertainty can be debated. Still, the method nicely illustrates the large differences in potential spatial resolution for estimating bathymetry from tides.

Sensitivity Experiment

We generate 285 10° × 10° sub-domains based on the estimates of propagation length being larger than 10° in most of the oceans. Figure 3.4a shows the sensitivity results in these sub-domains according to Eq. (3.9) with FES2014 tide data. Many sensitive sub-domains are in the coastal areas or regions with a large M_2 amplitude. The sensitivity in all regions is smaller than 2%. Some regions such as the Arctic Ocean have very small sensitivity values. The number of 285 sub-domains is too large for our computational resources, so we merged some neighboring sub-domains to reduce the number of parameters and CPU times.

Neighboring sub-domains are aggregated if they satisfy both criteria: (1) they have the same sensitivity directions (both negative or both positive) and (2) their propagation lengths are large and the sensitivity is small. Correction factor of bathymetry in each sub-domain is applied for every grid cell. A two-degree transition area is applied between neighboring regions. The correction factors in the cell of the transition areas is interpolated by the model, using linear interpolation on a triangulated discretization with the samples defined in the calibration as nodes. The sensitivity analysis results for these 110 aggregated sub-domains are reported in the bottom panel of Figure 3.4. The values of sensitivity are between -0.06 to 0.02. As a result, the parameter dimension has been reduced from $O(10^6)$ originally to 110 through the sensitivity analysis. Also, the size of the matrix H is 110 × 3977568 which is now small enough to deal with, given the constraint of limited computer memory space.

3.3.3 Parameter Estimation Results

We apply the coarse-to-fine parameter estimation method as described in Chapter 3.2.3 with 110 sub-domains. Figure 3.5a illustrates the cost function in each iteration for parameter estimation for the two approaches. It is not easy to observe the difference between the estimated and initial bathymetry from the map. So, we show the final relative change to the bathymetry in Figures 3.5b and 3.5c, which is the correction factor $[x]$ in Eq. (3.8). The final bathymetry estimated by the two approaches has a similar distribution.

In Figure 3.5a, the first 111 iterations are running with perturbed parameters and the result of each of these simulations is independent from each other. After the perturbed simulations, new parameters are iterative estimates based on the previous model output.

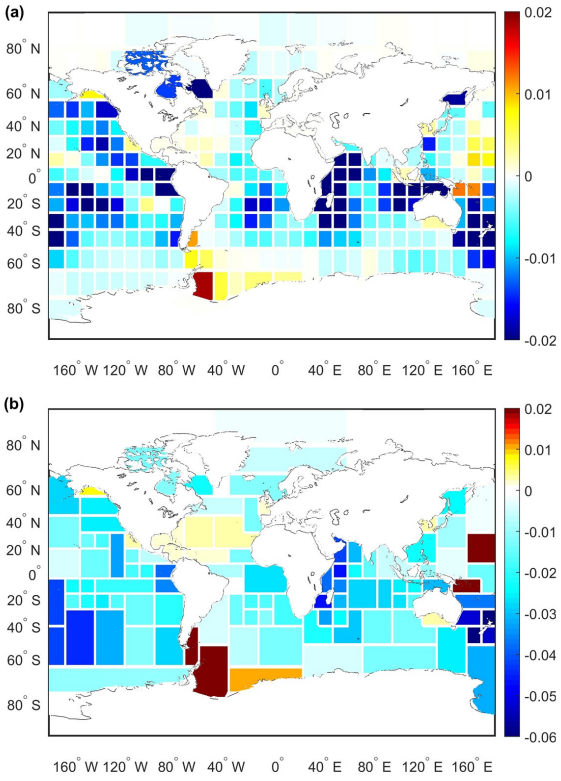

Figure 3.4: Bathymetry sensitivity test in GTSM with the coarse grid: (a) bathymetry perturbation is applied in 285 sub-domains; (b) bathymetry perturbation is applied in 110 sub-domains. Bathymetry in each subdomain is perturbed with 5%.

Therefore, these first 111 simulations can be computed in parallel if enough computing resources are available, after that parallelization has to be sought within a single iteration. The computational cost of the two approaches is similar and Approach 2 required seven more iterations than Approach 1. This is a relatively small difference and could be different with slightly different settings. We compared the values of the cost function of the original GTSM model with two resolutions and FES2014 observations. It is expected that the cost function value of Approach 2 is smaller than that of Approach 1. The values of the cost functions are greatly reduced from 4.56×10^6 to 1.48×10^6 in Approach 1 and from 2.84×10^6 to 1.22×10^6 in Approach 2. The percentage of reduction is approximately 67.5% for Approach 1 and 57% for Approach 2. The cost functions of both approaches show similar behavior with a sharp reduction in the first few estimation iterations and little improvement after that. It should be noted that the lower final cost function value of Approach 2 does not necessarily imply a higher accuracy of the estimated model output, since the methods do not use the same cost function. The cost function in Approach 1, as shown in Eq. (3.4) only includes the coarse grid model results while the cost func-

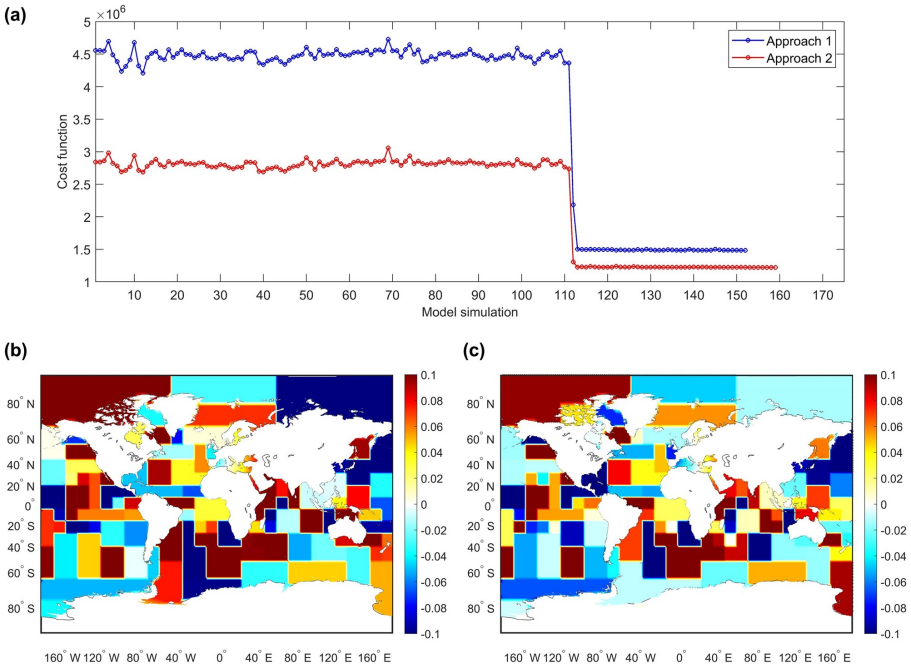

Figure 3.5: (a) Cost function for two approaches; Bathymetry differences in Approach 1 (b) and Approach 2 (c) show the value of $[x]$ in Eq. (3.8).

tion in Approach 2 Eq. (3.7) also includes the initial output from the coarse and fine grid models. Therefore, the cost functions for these two approaches cannot be compared directly and we use the RMSE for comparison instead.

Figure 3.6 shows the RMSE for the final model run with the estimated bathymetry as input from 1 to 14 January 2014. Before the parameter estimation, GTSM with the fine grid (Figure 3.6d) has better performance than the coarse grid model (Figure 3.6a) almost everywhere. The RMSE difference between the model with and without estimation are shown in Figures 3.6b and 3.6c (coarse model) and 3.6e and 3.6f (fine grid). The results in 3.6b and 3.6e are for Approach 1, and 3.6c and 3.6f are for Approach 2.

It can be observed that compared to FES2014 "observations", the estimated model output in most areas has improved significantly. The two approaches show a similar spatial pattern of RMSE. There are also a few areas where the RMSE values are marginally higher than the initial model; see the areas in yellow or red in Figures 3.6b, 3.6c, 3.6e and 3.6f (negative values in the RMSE difference mean the estimated results are worse than the initial results). The most persistent area, with consistently the worst results, between the experiments seems to be in the Bay of Bengal. Perhaps, effects other than bathymetry, play a role here, such as a lack of resolution around the large river delta in the north. In summary, we conclude that the estimated model has improved signifi-

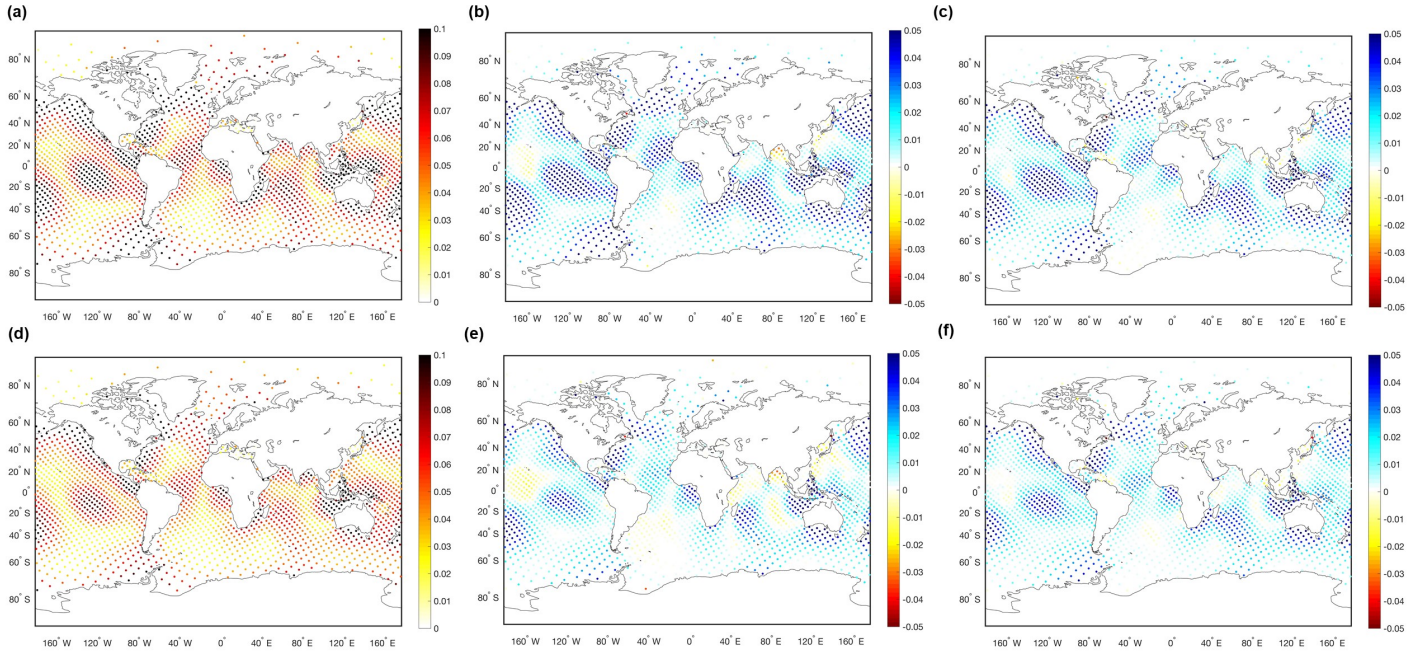

Figure 3.6: Spatial distribution of RMSE for two approaches from 1 to 14 January 2014. The upper panels depict the results for GTSM with the coarse grid and the lower panels are for the fine grid model. (a) and (d) RMSE for initial model; (b) and (e) difference in RMSE between the initial and estimated model in Approaches 1; (e) and (f) RMSE difference in approaches 2. The color blue indicates improvement [unit: m].

Table 3.2: Regional RMSE after bathymetry estimation in GTSM with two resolutions in [cm] from 1 to 14 January, 2014.

RMSE	GTSM with coarse grid			GTSM with fine grid		
	Initial	A1[a]	A2	Initial	A1	A2
Arctic Ocean	7.06	4.55	5.78	5.24	3.98	4.34
Indian Ocean	6.70	3.74	3.89	5.57	4.21	3.62
North Atlantic	6.89	3.90	4.51	5.41	3.47	3.43
South Atlantic	6.97	4.44	4.69	5.69	4.40	3.96
North Pacific	4.76	3.16	3.65	4.15	3.32	3.11
South Pacific	7.03	3.62	4.16	5.57	3.73	3.43
Southern Ocean	5.35	3.16	3.69	4.28	3.04	2.97
Total	6.47	3.76	4.19	5.23	3.78	3.49

[a] A1 and A2 refer to Approach 1 and Approach 2.

cantly on the global scale.

A comparison of spatially averaged RMSE over seven regions for two approaches, the coarse model and the fine model, are shown in Table 3.2. Compared to the initial model output, the accuracy of output after optimization of both the fine and coarse models are improved in every region. For instance, the RMSE has a reduction of 42% and 35% for the model with coarse grid in Approach 1 and 2, respectively, and in the fine model it is also reduced by 28% and 33%, respectively.

Because the coarse model Approach 1 directly optimizes the mean RMSE, so one would expect an improvement. For Approach 2, the cost function used for optimization uses observations that are corrected for differences between the fine and coarse models. Still, Approach 2 improves the performance for all regions compared to the initial model. Finally, both approaches improve the accuracy of the fine model, even though the fine model is already more accurate than the coarse model initially. On average the fine model with the calibrated bathymetry of Approach 1 has an accuracy similar to the coarse model for Approach 1. Thus it does not really benefit from the higher initial accuracy of the fine model. However, Approach 2 does benefit from the higher initial accuracy of the fine model and results in the best performance of all the combinations for the calibration time span. Most regions behave similar to the average, but in the Arctic Approach 1 results in a better fit to the data, than Approach 2.

In summary, both calibrations result in an improved fit to the measurements for both the coarse and the fine model. For the coarse model, approach 1 seems slightly better and for the fine model Approach 2. This is of course comparing to the same data as was used for the estimation. Compared to Approach 1 with only the coarse grid estimation, Approach 2 uses both coarse and fine grid models in the cost function. Approach 2 probably has the advantage to capture some small-scale features independently of the coarser grid. The aim is that for Approach 2 the estimation results are more accurate for the fine grid GTSM.

3.4 Model Validation

In order to validate the model performance more independently from the simulation period and data that we used in the estimation stage, the forecast has been compared against the FES2014 data for the whole of the year 2014. Also, the main tide component M_2 is analyzed with FES2014 data. In addition, the model forecast is also compared to a large number of tide gauges for both tide and surge validation.

3.4.1 Validation with FES2014 Dataset

The year 2014 is chosen as the validation period with the FES2014 dataset to analyze the model performance. Two time period are used as examples for detailed model performance explanation. The first period is chosen from 15 to 31 January 2014, which are the days in January following the estimation stage and this contains the second spring-neap cycle within the first lunar cycle in 2014. The model forecast on 1 to 31 July 2014 is also analyzed here to inspect the model performance in another season.

Figure 3.7 shows the forecast regional RMSE of the fine resolution GTSM with estimated bathymetry by the two approaches in the twelve months of the year 2014. RMSE for all the seven regions has improved significantly for every month with both approaches. Contrary to the calibration period, where Approach 2 performed slightly better for the fine model, here Approach 1 generally shows marginally better results, except for the Indian Ocean.

In Figure 3.7, the RMSE between the model output and the observed value varies from month to month and also within the month. For example, the initial global average of RMSE in the calibration period is 5.23cm, while it is 5.84 cm in the forecast period 15 to 31 January 2014, as Table 3.3 shows. One can observe that accuracy in the period 15 to 31 January, 2014 is lower (higher RMSE) than the calibration period, both before and after calibration and independent of the approach. It fits our existing experience that the interaction between the various tidal constituent changes over time. However, the general conclusion is that the accuracy after the estimation has been greatly improved also for other forecast periods.

Figure 3.8 shows the spatial distribution of RMSE difference for GTSM with the fine grid in 15 to 31 January (a) and July (b) in Approach 1. Approach 2 shows a similar spatial distribution to Approach 1 (not shown here). The spatial distribution of the RMSE difference in Figure 3.8 is similar to that in the calibration period. Most of the regions are improved but output in some regions is marginally worse than that in the initial model, which is even more obvious in the period 15 to 31 January. The similar RMSE distribution in July demonstrates the excellent performance of the calibrated model for the long-term forecast.

In addition, we also evaluate the model performance in the frequency domain. Tidal analysis is based on the model output for the year 2014. The root-mean-square (RMS) between the model and the FES2014 dataset in 1973 locations for major tide constituents are summarized in Table 3.4. For comparison with (Stammer et al., 2014), we use the same formula for the RMSE per tidal constituent:

$$RMS = \sqrt{\overline{(A_m cos(\omega t - \phi_m) - A_o cos(\omega t - \phi_o)]^2}} \tag{3.13}$$

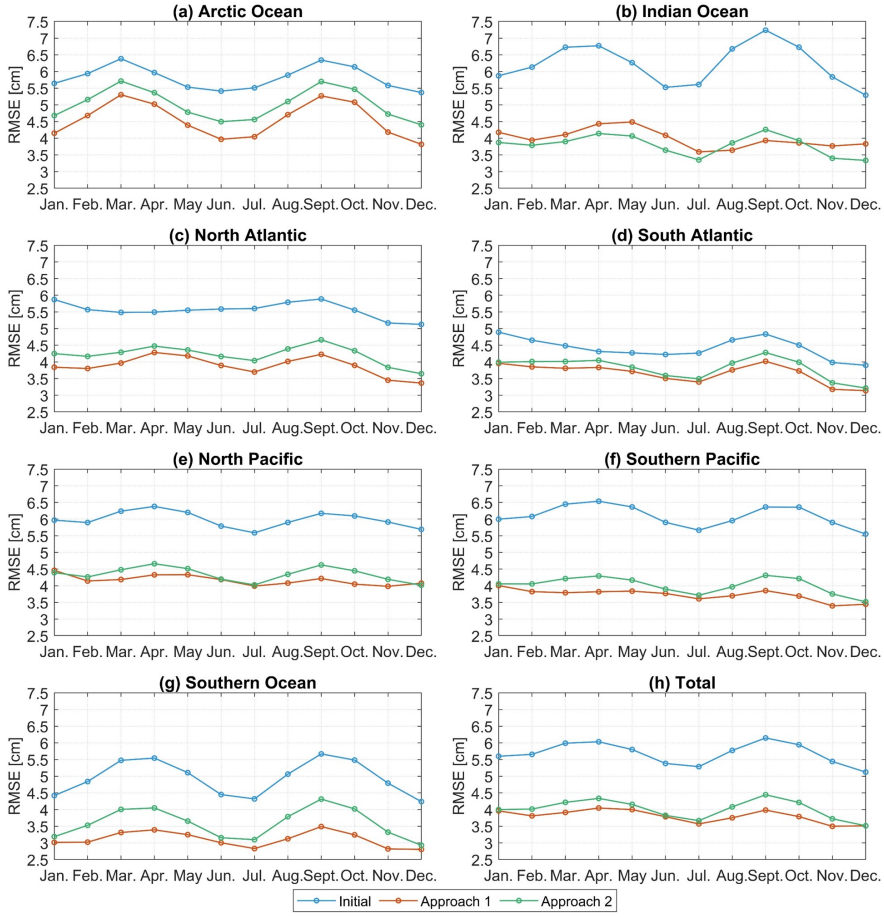

Figure 3.7: Regional RMSE between GTSM with the fine grid in two approaches and FES2014 for the year 2014 [cm].

Table 3.3: Regional forecast RMSE after bathymetry estimation in GTSM with fine grid in [cm] for two periods.

RMSE	1 to 14 January			15 to 31 January		
	Initial	A1[a]	A2	Initial	A1	A2
Arctic Ocean	5.24	3.98	4.34	5.93	4.27	4.92
India Ocean	5.57	4.21	3.62	6.04	4.12	4.01
North Atlantic	5.41	3.47	3.43	6.17	4.08	4.78
South Atlantic	5.69	4.40	3.96	6.14	4.45	4.67
North Pacific	4.15	3.32	3.11	5.42	4.40	4.58
South Pacific	5.57	3.73	3.43	6.30	4.17	4.48
Southern Ocean	4.28	3.04	2.97	4.51	2.97	3.34
Total	5.23	3.78	3.49	5.84	4.05	4.33

[a] A1 and A2 refer to Approach 1 and Approach 2.

Table 3.4: RSS and RMS of 8 major tide components against FES2014 dataset in [cm].

	RMS for all locations								RSS
Components	Q1	O1	P1	K1	N2	M2	S2	K2	
Initial model	0.48	1.12	0.55	1.62	1.01	4.50	2.79	1.76	6.05
Approach 1	0.43	0.89	0.40	1.19	0.69	2.25	1.77	1.18	3.55
Approach 2	0.44	0.96	0.41	1.18	0.66	2.54	1.91	1.46	3.92

where A_m, A_o are the amplitudes from model output and observations. ϕ_m and ϕ_o are terms of phases lag. ω is the tide frequency. The overbar represents the computation over one full cycle of the constituent (e.g.,ωt varying from 0 to 2π), as well as all the locations. A striking feature of the table is the lower RMS for the main components and the Root-Squared-Sum (RSS) over these components after the estimation in both approaches. The M_2 component shows the largest change; it is reduced from 4.50cm in the initial model to 2.25cm and 2.54cm for Approaches 1 and 2, respectively. The significant improvements of tide components for the estimated models demonstrate that they can be used for the long-term forecast.

A tidal analysis is also performed for the observation from Deep-Ocean Bottom Pressure Recorder (BPR) to compare GTSM with the model described by Stammer et al. (2014). We used model output for the full year of 2014 for this comparison. BPR data is available from the Supplement of Ray (2013). As an example, Table 3.5 shows the results from the NSWC (Naval Surface Weapons Center) model, FES2012, initial GTSM before calibration and estimated GTSM with Approach 2. The data of NSWC and FES2012 are from Table 3 in Stammer et al. (2014). In comparison to the seven purely hydrodynamic models in Stammer et al. (2014) (their Table 12), GTSM has an RMS for M2 of 5.17cm which is lower than other models except for the NSWC, which has an RMS of 4.27cm.

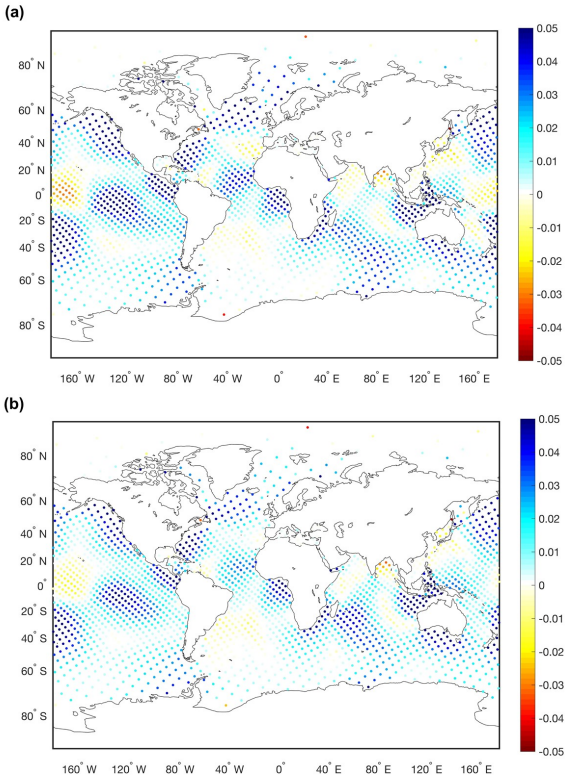

Figure 3.8: Spatial distribution of RMSE difference for GTSM with the fine grid in Approach 1 in the forecast period (a) 15 to 31 January 2014; and (b) 1 to 31 July 2014. The color blue shows improvement [unit: m].

GTSM is further improved by the calibration but does not become as accurate as the modern assimilative tide models described by Stammer et al. (2014). For instance, the RMS of M2 component and RSS for eight major components of the FES2012 model against deep ocean data in Table 3.5 are 0.66cm and 1.12cm, respectively, while GTSM with estimated bathymetry in Approach 2 are 2.55cm and 3.96cm for the RMS of M2 and RSS, respectively. This is one of the reasons why we chose FES2014 dataset to be used as 'observations' for our deep ocean calibration. The main advantage of our calibration approach for GTSM is that it can also be straightforwardly applied for the studies of the effects of sea level rise, since surge can be included in the simulation by adding winds and air pressure to the forcing. For example, the first global reanalysis of storm surges and extreme sea levels (the GTSR dataset) was presented based on the GTSM (Muis et al., 2016). In Chapter 3.4.2, we also applied the one-year sea level forecast to analyze the surge representation.

The amplitude and phase difference of M_2 component between GTSM with the fine grid and FES2014 dataset is illustrated in Figure 3.9. Compared to the FES2014 dataset,

Table 3.5: RSS and RMS of 8 major tide components against BPR dataset in [cm].

	RMS for all locations								RSS
Components	Q1	O1	P1	K1	N2	M2	S2	K2	
NSWC[a]	0.29	0.87	0.64	1.29	1.15	4.27	1.78	0.66	5.11
FES2012	0.22	0.31	0.36	0.47	0.34	0.66	0.41	0.22	1.12
Initial Model	0.56	1.24	0.65	2.10	0.99	5.17	2.36	1.60	6.56
Approach 2	0.48	0.91	0.43	1.49	0.59	2.55	1.82	1.41	3.95

[a] Data of NSWC and FES2012 are from Table 3 in Stammer et al. (2014).

the differences in amplitudes and phases are substantially smaller in the estimated model for both approaches than the initial model. Approach 2 has a slightly better performance in amplitude (Figure 3.9c) than Approach 1 (Figure 3.9b), which is opposite in phases (Figures 3.9e, 3.9f).

3.4.2 Validation with UHSLC Tide Gauge Data

The calibrated models were also compared to UHSLC tide gauge data. Contrary to the selected FES data of the previous chapter, most of these locations are along the coast, and have one average large tidal amplitude with more pronounced local influences. The time periods used are the same set as above. Figure 3.10 shows the spatial distribution of RMSE without estimation (Figure 3.10a) and RMSE difference for the tide output and data from 230 tide gauges for the calibration period from 1 to 14 January, 2014 in Approach 2 (Figure 3.10b). Approach 1 (not shown here) reports a similar distribution to Approach 2. Most of the tide gauges are distributed in the coastal region. The RMSE in these locations (Figure 3.10a) is much larger than in the deep ocean with the comparison of the FES2014 dataset, which is as expected since tide constituents often have larger amplitudes in the coastal regions. The RMSE difference in Approach 1 is similar to that in Approach 2 and the RMSE difference in the coarse model is similar to it in the fine model. The model output from the estimated model is in better agreement with the UHSLC observations than the output from the initial model in the majority of the locations.

GTSM with the fine grid is more accurate than with the coarse grid, both before and after calibration. For example, RMSE in the initial GTSM before calibration with the coarse and fine grids are 17.23cm and 12.98cm, respectively. These are reduced to 13.49cm in coarse grid and 11.12cm in the fine grid after the estimation by Approach1. Approach 2 shows similar results. In a relative sense the improvements in the calibration are quite significant, but less than in deep water. It is possible that resolution and more local influences play a larger role compared to deep water. This can also be seen when one compares the calibrated coarse model results to the initial fine model, where the calibration apparently can not compensate for the lower resolution. Still, both the coarse model and the fine model also benefit at the coast from a calibration that was performed using only data on deep water. The performance of estimated models with the fine grid

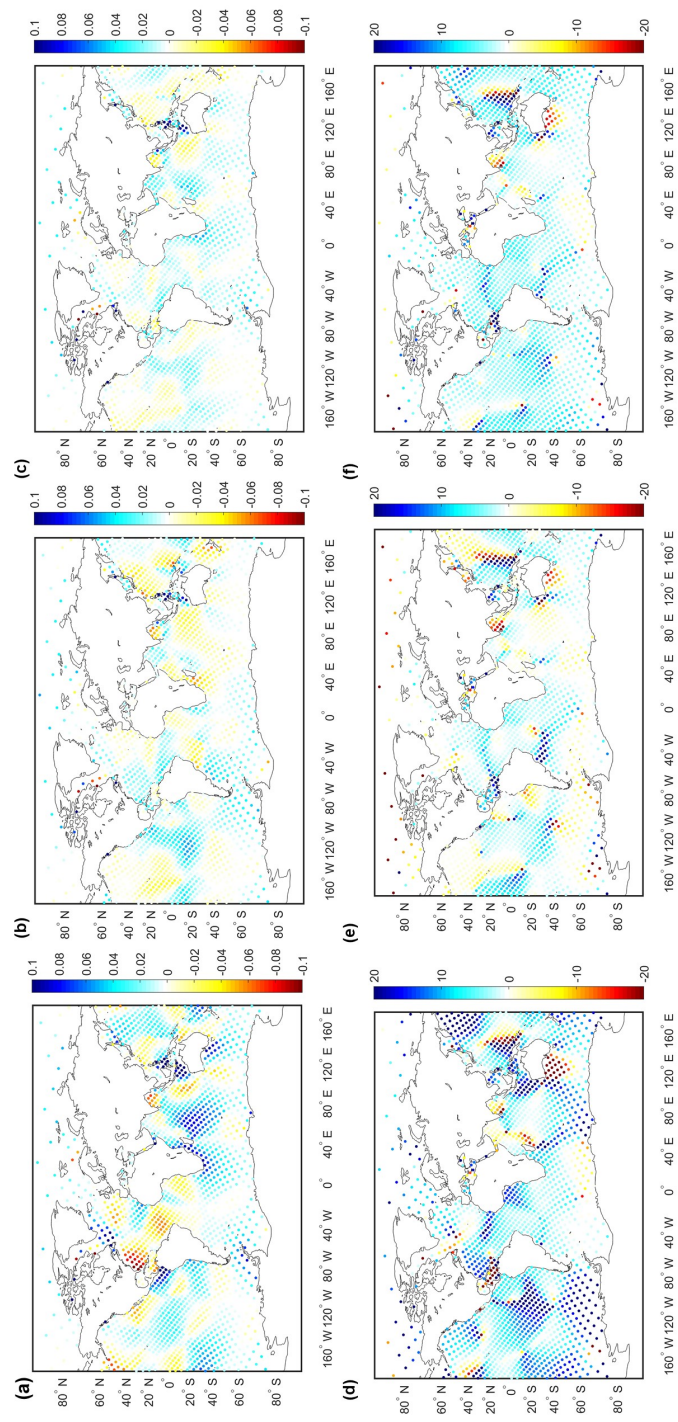

Figure 3.9: Spatial distribution of amplitude and phase difference of M_2 between the model and FES2014 dataset. (a),(b) and (c): Amplitude difference for the initial GTSM, model estimated by Approach 1 and Approach 2, respectively [unit: m]; (d), (e) and (f): Phases difference for the initial GTSM, model estimated by Approach 1 and Approach 2, respectively [unit: degree].

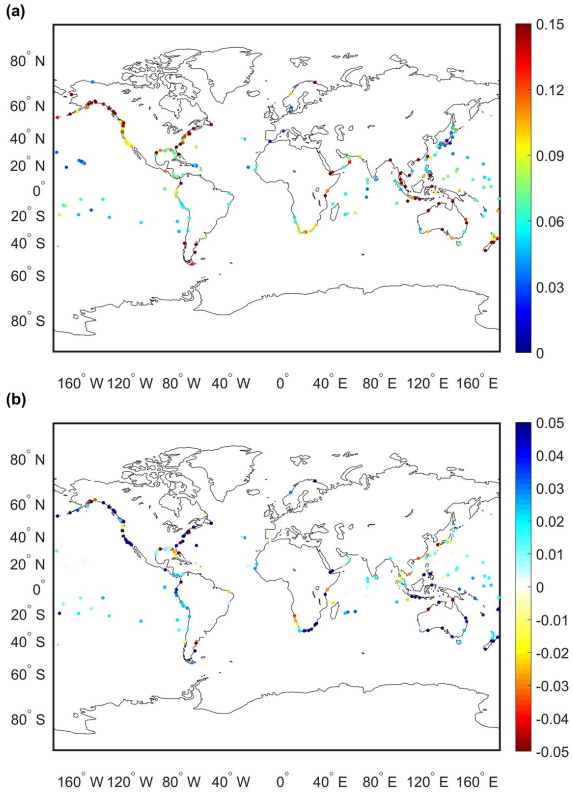

Figure 3.10: Spatial distribution of RMSE with the UHSLC data from 1 to 14 January, 2014: (a) initial RMSE in fine GTSM; (b) RMSE difference in fine GTSM by Approach 2. RMSE differences shown in blue indicate improvement[unit:m].

is analyzed further with a one-year prediction of tide and surge for the full year of 2014. Figure 3.11a shows that the RMSE of the tide has improved significantly for both approaches and all months. Approach 1 performed slightly better than Approach 2. The spatial patterns of the tide RMSE in every month are very similar to the ones shown in Figure 3.10 and therefore not shown. Additional experiments with wind forcing (3.11b-c) show that the surge is much less sensitive to small adjustments of the bathymetry at large scales. The total water level, being the sum of tides and surge, benefits from the improved tides.

As an example, time series of the tide at station Benoa with the coordinate (8.75°S, 115.21°E) from initial simulation and estimated simulation in January and July 2014 are shown in Figure 3.12. The RMSE is decreased by approximately 50% in January and 59% in July for Approach 1, which is marginally better than for Approach 2 (approximately 44% and 52%, respectively).

Similar to the comparison to FES data, also for UHSLC tide gauges, Approach 2 performs best for the calibration period. Also here, the RMSE is higher for other periods

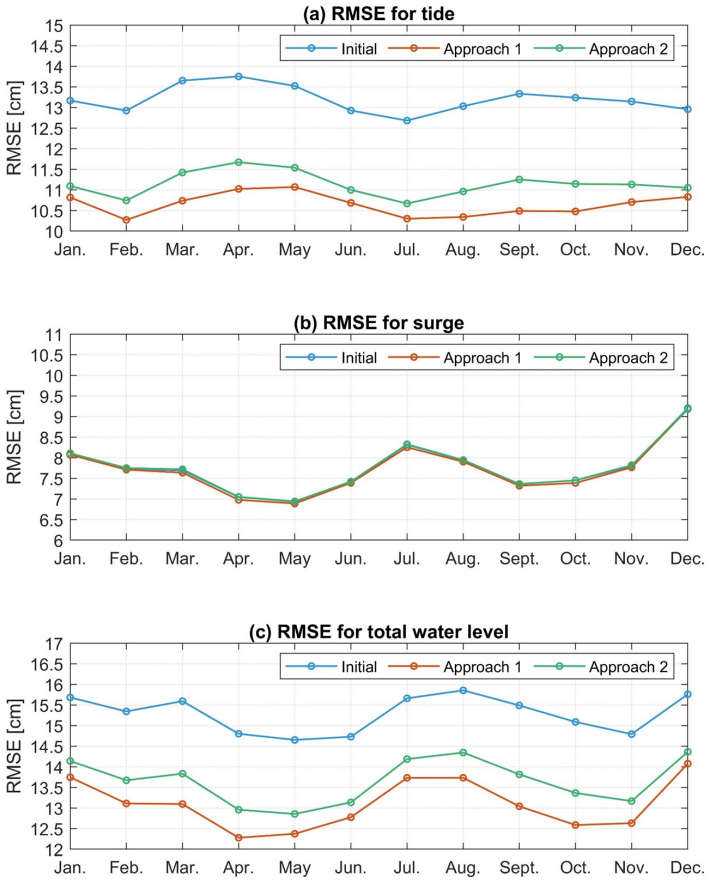

Figure 3.11: RMSE between GTSM with fine grid in two approaches and FES2014 for the whole year 2014 [cm] (a) RMSE for tide; (b) RMSE for surge; (c) RMSE for total waterlevel.

than for the calibration period. This confirms our perception that the fine model generally improves most using Approach 2 during the calibration period, not just for the locations and dataset used for the calibration. In other periods, the tidal constituents interact differently, leading to estimates that over-fit the data to some extent.

This problem can be solved by using a longer simulation time, such as one month, or even longer. However, longer simulation time means higher computational cost and larger storage requirement, which is out of reach for the current computing environment and implementation. Future work will attempt to solve this problem by modifying the algorithm.

We also note that the calibration changes the model performance significantly. However, in the current implementation the difference between the model output between the fine and the coarse models is only computed at the start. This can potentially be improved further. The algorithm in Approach 2 is similar to the inner loop of Incremen-

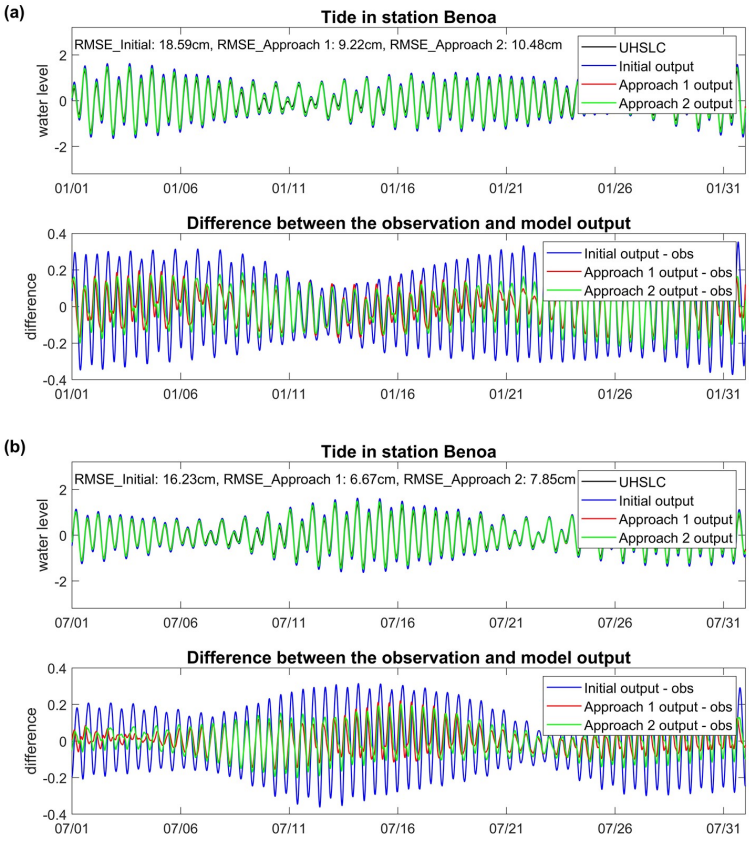

Figure 3.12: Tide elevation and difference comparison between model output and observation at station Benoa during (a) January and (b) July, 2014 [unit:m].

tal 4D-Var (Trémolet, 2007). The cost function in Incremental 4D-var is minimized at a low resolution using an iterative algorithm (inner loop) and the resulting increment is then interpolated back to the high resolution and added to the current first guess (outer loop). A similar outer loop can also be implemented for Approach 2 in the future. The estimated parameters can be used as the new first guess to the inner loop. Because of the large computational cost, we have not performed this experiment yet, but we aim to do so in the future, after the algorithm has been optimized further.

3.5 Conclusions

We have presented a complete application of parameter estimation for the high-resolution global tide and surge model (GTSM), with measurements from the FES2014 dataset. A coarse-to-fine strategy is proposed by using output from the coarse model

to replace the fine model during (parts of) the estimation, which effectively reduces the computational demand to about 33%. Two variants of this approach were tested. Moreover, the computational demand and memory requirements are further reduced by maintaining only the most sensitive parameter dimensions, which were found through sensitivity experiments.

This study focuses on the estimation of bathymetry, which is considered to be the most influential parameter. A major challenge for estimation of bathymetry in a global tide model is the large computational cost. The optimization algorithm performs a large number of model simulations and a single model in high resolution needs an enormous computational cost, even when parallel computing is deployed. In this case, the coarse-to-fine strategy is applied to reduce the single model simulation time and make it computationally affordable for parameter estimation. We tested two approaches here: Coarse Calibration (Approach 1), where all model runs in the calibration are performed with a coarser model, and Coarse Incremental Calibration (Approach 2), where the model differences between initial model output and adjusted model output are replaced by a coarser model, but the observation model differences are computed with the fine model. Coarse Incremental Calibration requires one more fine model simulation than Coarse Calibration for the first guess. In our experiments the computational cost is reduced by a factor of approximately three based on these two approaches.

In addition to reducing the computing time in a single model, the number of model simulations also needs to be reduced, which is done here by reducing the number of parameters, because the initial number of simulations is proportional to the parameter dimension. To reduce the parameter dimension, a sensitivity test is performed by perturbing the bathymetry in a large number of spatial domains. First, the number of domains is reduced to 285 domains using an analysis based on the tide propagation length. Next a uniform correction factor is applied to the bathymetry for one domain at a time. Finally, using the computed sensitivity, we are able to decrease the number of parameters further to 110 domains. This number of 110 parameters is just feasible on the available computer infrastructure, with the existing implementation.

The optimization procedure leads to a significant reduction of the cost function for both approaches and to an improved fit to the FES2014 data for both the coarse and the fine versions of the model. Analysis from the frequency domain illustrates significant improvements, especially for the M_2 component, after the estimation. The estimation results are evaluated further by comparing model simulations for the whole of the year 2014 against the FES2014 dataset and the UHSLC dataset, which shows that although the calibration is performed for 2 weeks, this still results in a more accurate model for other time periods. Comparison to the mostly coastal tide gauges shows that the influence of resolution is more important there. The accuracy of the coarse model improves through calibration, but cannot exceed the accuracy of even the uncalibrated high-resolution model. On the other hand, the fine model benefits from the calibration even at coastal stations. The surge simulation further demonstrated that the estimated bathymetry is reasonable for not only tide perdiction but also the long-term total water level prediction.

Experiments show that the parameter estimation scheme efficiently improves the accuracy of the GTSM modelled tides. Further work will concentrate on: The calibra-

tion algorithms work quite efficiently in terms of computation, but the experiments are now limited by the memory requirement for the inversion step in the DUD algorithm. At the same time, the results indicate that a longer time span for the calibration could be beneficial. A modification of the algorithm or parallelization of this step is necessary to test this. The increments in Approach 2 are now based on the initial fine model simulation. Somewhat similar to the outer loop in the incremental 4D-VAR, one can restart the algorithm with the updated fine model, which can potentially further improve the accuracy of the model. Finally, we have focused on calibration of the bathymetry throughout this paper. Closer to the coast, the uncertainty related to bottom friction is probably important. The model performance may be further improved by the calibration of the more local bathymetry together with bottom friction, as well as using additional local observations. This will also provide an opportunity to verify if the friction can indeed be ignored for the initial calibration at the larger scales.

Bibliography

Caldwell, M. A. M., P. C., & Thompson, P. R. (2015). Sea level measured by tide gauges from global oceans – the joint archive for sea level holdings (ncei accession 0019568), version 5.5. *NOAA National Centers for Environmental Information, Dataset*. https://doi.org/10.7289/V5V40S7W

Courtier, P., Thépaut, J.-N., & Hollingsworth, A. (1994). A strategy for operational implementation of 4d-var, using an incremental approach. *Quarterly Journal of the Royal Meteorological Society*, *120*(519), 1367–1387. https://doi.org/10.1002/qj.49712051912

González, A. (2009). Measurement of areas on a sphere using fibonacci and latitude–longitude lattices. *Mathematical Geosciences*, *42*, 49–64.

Muis, S., Verlaan, M., Winsemius, H., Aerts, J., & Ward, P. (2016). A global reanalysis of storm surges and extreme sea levels. *Nature Communications*, *7*, 1–12. https://doi.org/10.1038/ncomms11969

Openda user documentation. (2016). Daltares.

Ralston, M. L., & Jennrich, R. I. (1978). Dud, A Derivative-Free Algorithm for Nonlinear Least Squares. *Technometrics*, *20*(1), 7–14. https://doi.org/10.1080/00401706.1978.10489610

Ray, R. D. (2013). Precise comparisons of bottom-pressure and altimetric ocean tides. *Journal of Geophysical Research: Oceans*, *118*(9), 4570–4584. https://doi.org/https://doi.org/10.1002/jgrc.20336

Stammer, D., Ray, R. D., Andersen, O. B., Arbic, B. K., Bosch, W., Carrère, L., Cheng, Y., Chinn, D. S., Dushaw, B. D., Egbert, G. D., Erofeeva, S. Y., Fok, H. S., Green, J. A. M., Griffiths, S., King, M. A., Lapin, V., Lemoine, F. G., Luthcke, S. B., Lyard, F., … Yi, Y. (2014). Accuracy assessment of global barotropic ocean tide models. *Reviews of Geophysics*, *52*(3), 243–282. https://doi.org/10.1002/2014RG000450

Trémolet, Y. (2007). Incremental 4d-var convergence study. *Tellus A*, *59*(5), 706–718. https://doi.org/10.1111/j.1600-0870.2007.00271.x

Wang, X., Verlaan, M., Apecechea, M. I., & Lin, H. X. (2021). Computation-efficient parameter estimation for a high-resolution global tide and surge model. *Journal of Geophysical Research: Oceans*, *126*(3), e2020JC016917. https://doi.org/https://doi.org/10.1029/2020JC016917

Chapter 4

Memory-efficient Parameter Estimation with Model Order Reduction

Accurate parameter estimation for the Global Tide and Surge Model (GTSM) benefits from observations with long time-series. However, increasing the number of measurements leads to a large computation demand and increased memory requirements, especially for the ensemble-based methods that assimilate the measurements at one batch. In this study, a memory-efficient parameter estimation scheme using model order reduction in time patterns is developed for a high-resolution global tide model. We propose using projection onto empirical time-patterns to reduce the model output time-series to a much smaller linear subspace. Then, to further improve the estimation accuracy, we introduce an outer-loop, similar to Incremental 4D-VAR, to evaluate model-increments at a lower resolution and subsequently reduce the computational cost. The inner-loop optimizes parameters using the lower-resolution model and an iterative least-squares estimation algorithm called DUD. The outer-loop updates the initial output from the high-resolution model with updated parameters from the converged inner-loop and then restarts the inner-loop. We performed experiments to adjust the bathymetry with observations from the FES2014 dataset. Results show that the time patterns of the tide series can be successfully projected to a lower dimensional subspace, and memory requirements are reduced by a factor of 22 for our experiments. The estimation is converged after three outer iterations in our experiment, and tide representation is significantly improved, achieving a 34.5% *reduction of error. The model's improvement is not only shown for the calibration dataset, but also for several validation datasets consisting of one year of time-series from FES2014 and UHSLC tide gauges.*

Parts of this chapter have been included in a manuscript submitted for publication to Ocean Modelling:

Wang, X., Verlaan, M., Apecechea, M. I., and Lin, H. X. Parameter Estimation for a Global Tide and Surge Model with a Memory-Efficient Order Reduction Approach.

4.1 Introduction

In Chapter 3, we proposed a computation-efficient parameter estimation scheme to estimate bathymetry for a high-resolution Global Tide and Surge Model (GTSM). In the estimation procedure, observations are compared with the model output in the time series formula. Tidal constituents are widely used as model output in estimation applications, such as the estimation of the FES model (Lyard et al., 2021). But tidal constituents cannot be directly computed in GTSM because GTSM is a time-stepping model. The Time-stepping model allows a more accurate representation of non-linear interactions at the coast, which is also recognized by (Lyard et al., 2021). To obtain accurate tidal analysis results, we have to simulate the GTSM for a year based on the Rayleigh criterion to separate diurnal constituent S1 from K1. If one would include seasonal constituents Sa and Ssa, several years would be required since they show large inter-annual variability. In addition, hundreds of model runs would be simulated in the estimation process. Therefore, parameter estimation in tidal constituents is not feasible with the computational facilities available to us. The use of time series for weeks or a month can significantly reduce the simulation time and computational complexity. But the simulation time length of two weeks (one spring-neap cycle) is short and leads to estimates that over-fit the data to some extent (Wang et al., 2021). However, longer time series imply larger memory requirements in the analysis step, which is not feasible for the current implementation and computational cluster. Therefore, an efficient approach has to designed which can reduce the memory requirement and enable a longer simulation time length.

For ensemble-based data assimilation methods (Evensen, 1994), the memory use is proportional to the number of measurements assimilated in one batch multiplied by the number of perturbed model runs, called ensemble members. This also applies to the method used in this paper. Observations are often assimilated in one batch to maintain consistency between the estimated parameters and model output after the estimation (Emerick & Reynolds, 2013; Evensen & van Leeuwen, 2000), which cannot be guaranteed for incremental assimilation in smaller batches. However, this leads to a large size of the linearized model outputs $O(NN_tN_s)$, where N, N_t, N_s are the number of ensembles, number of observation time steps, and number of locations, respectively. When we attempt to include more observations and to estimate more parameters, this can result in a huge memory usage on a single compute-node. There are at least two ways to ease the huge memory usage problem: 1. parallelization of the linear solver; and 2. reducing the size of the problem by approximation. Here we follow the second approach by using model order reduction methods. Note that variational methods have different characteristics in terms of memory usage.

Model Order Reduction (MOR) is a collection of methods that can be used to reduce the computational complexity of mathematical models in numerical simulations with an approximation of the original model (Antoulas et al., 2015). In this paper, we develop a new method time-POD, which aims to reduce the size of the model output, so that the memory needed for data assimilation can be reduced. The method was inspired by the Proper Orthogonal Decomposition (POD) (Chatterjee, 2000), which projects the spatial patterns of the state onto the leading singular vectors. Here we project onto the leading singular vectors of the time patterns instead. POD is one of the MOR techniques first

introduced in fluid dynamics by Lumley (1967). It was already known as the Karhunen-Loève expansion (Kosambi, 1943) in statistics, and also as Principal Component Analysis (PCA) (Jolliffe & Cadima, 2016) or Empirical Orthogonal Functions (EOF) (Monahan et al., 2009) in meteorology. POD methods (Liang et al., 2002), such as the Karhunen-Loève decomposition (KLD), PCA, and Singular Value Decomposition (SVD), have been applied in various fields such as fluid dynamics (Cazemier et al., 1998), pattern recognition (Kopp et al., 1997), and more recently in control theory and inverse problems.

MOR has been applied in both ensemble-based and variational data assimilation systems (Beck & Ehrendorfer, 2005; Cane et al., 1996; Cao et al., 2007; Farrell & Ioannou, 2001). The typical application of MOR is projecting the spatial patterns of model state variables to truncated characteristic vectors. For instance, a dual-weighted proper orthogonal decomposition (DWPOD) is proposed combining with four-dimensional variational method (4DVar) to reduce state space orders in a global shallow-water model (Daescu & Navon, 2008). Lin and McLaughlin (2014) reduced the parameter dimension by POD for an EnKF data assimilation system.

In this study, we proposed a low-storage parameter estimation scheme with MOR for GTSM. The method is based on an iterative least-squares algorithm DUD. With the use of this smoother type estimation algorithm, the memory needed increases linearly with the simulation time length. The total data size is in the order of $O(10^9)$ when the time length is larger than one month in this application, which leads to memory issues. Therefore, we developed a time-POD approach to reduce the dimension of the model output by projecting the time space of the model output onto a smaller subspace. The main advantage of the time-POD is that the simulation required is not restricted by the Rayleigh criterion, which normally requires a year's simulation for accurate estimation of tidal constituents. The projection reduces the memory requirements while still accurately representing the time signal for any simulation length. The required length of the time-span considered then becomes limited by other considerations. In our experiments, a length of two weeks leads to some over-fitting for that time period, while the results for one month are almost equally accurate for an entire year.

Furthermore, parameter estimation accuracy is also affected by the calibration algorithm. The approach of using a lower resolution model in the estimation is similar to Incremental 4D-Var, and an outer loop iteration can further improve the estimation accuracy by updating the reference using a new fine resolution simulation with the updated parameters (Chen & Oliver, 2013; Emerick & Reynolds, 2013). The incremental 4D-Var method consists of nested inner-loops and outer-loops to reduce computational cost for data assimilation. It is applied successfully in the assimilation system at the ECMWF (Courtier et al., 1994; Mahfouf & Rabier, 2000; Trémolet, 2007). In this study, we use a very similar structure. Coarse Incremental Estimation (Wang et al., 2021) uses a coarser grid to represent the model increments between the initial model and model with updated parameters. The outer loop uses the high-resolution model with the updated parameters from the converged inner-loop to restart the estimation process. It is expected that this will result in a better match between the observations and the fine grid model.

Chapter 4.2 describes the parameter estimation scheme, including POD application in temporal patterns and the outer loop implementation. In Chapter 4.3, information

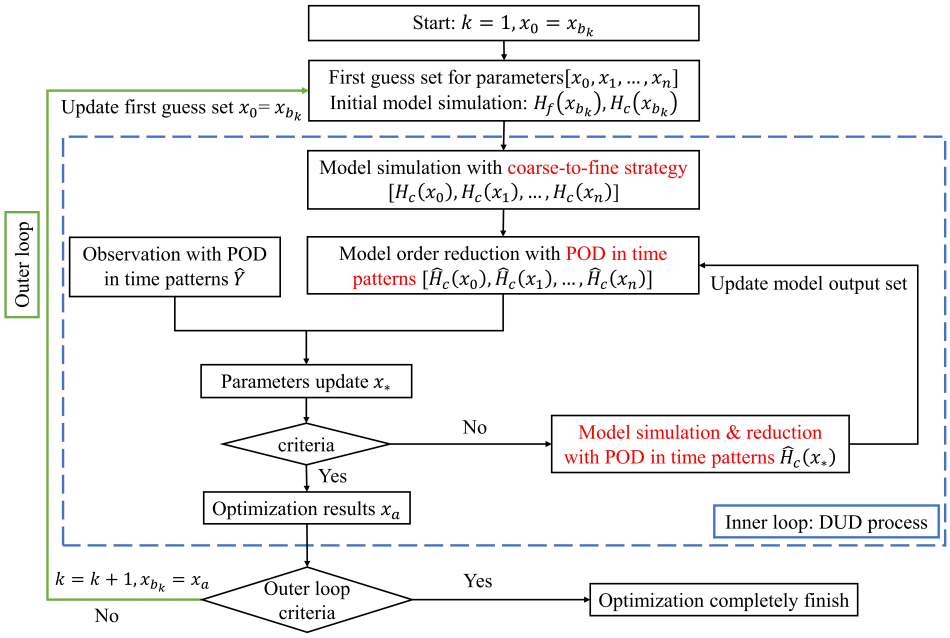

Figure 4.1: Flowchart of the iterative parameter estimation scheme to connect the components: DUD, time-POD and the outer-loop iteration.

about experiment set-up is provides. POD performance is evaluated by firstly analyzing the accuracy of projected and reconstructed model output and observations and secondly, comparing the bathymetry estimation performance with or without the application of MOR. We also perform a parameter estimation experiment with an extended simulation time of one month. Model validation for the year 2014 is presented in Chapter 4.4. Finally, discussions and conclusions follow in Chapter 4.5.

4.2 Parameter Estimation with Model Order Reduction

4.2.1 Parameter Estimation Framework

We designed an efficient and low-memory usage parameter estimation scheme with model order reduction for the high-resolution tide models to reduce parameter uncertainties and improve forecast accuracy. The flowchart of this parameter estimation scheme is shown in Figure 4.1.

The basic estimation algorithm applied here is called DUD (Doesn't use derivatives) in a generic data-assimilation toolbox OpenDA (*OpenDA User Documentation*, 2016; Ralston & Jennrich, 1978). It optimizes the parameters by iteratively minimizing the following cost function:

$$J(x) = \frac{1}{2}(x - x_b)^T B^{-1}(x - x_b) + \frac{1}{2}[Y - H(x)]^T R^{-1}[Y - H(x)] \tag{4.1}$$

where Y is the field observation vector including all time steps in $t \in [t_1, t_{N_t}]$ and all stations $(1, ..., N_s)$. x is the vector of parameters to be estimated, with the dimension of n. $H(x)$ is the model output vector matching observation locations for all time steps. x_b is the initial parameter vector. B and R are the background and observation error covariances, respectively. The dimension of observation Y and model output $H(x)$ in all space points and time steps is as $O(N_s \times N_t)$. The first term in the right hand of the cost function (Eqs. 4.1) is the background term J_b constraining the changes to the initial parameters. The second term is the observation term J_o representing the difference between model output and observations. For the brief introduction of the DUD algorithm and parameter estimation scheme, we only describe the observation term of the cost function in the following chapters.

Figure 4.1 shows the flowchart of the parameter estimation scheme, connecting the components DUD, time-POD and outer-loop. DUD is implemented in the inner loop combining with the coarse-to-fine strategy and time-POD application. DUD is a Gauss-Newton similar algorithm but derivative-free. It started from the model simulation of first guesses for the parameters $x_0 = x_b$ and n simulations with each parameter perturbed as $(x_1 = x_b + \delta e_1, x_2 = x_b + \delta e_2, x_n = x_b + \delta e_n)$. Parameter is updated for an approximate linear model that fits exactly through the model output for $[x_0, x_1, ..., x_n]$. DUD iteratively finds the parameters that minimize the sum of squares between model output and observations.

We propose three methods to improve estimation performance while reducing the computational cost and memory requirement based on the original DUD algorithm. They are the coarse-to-fine strategy, model order reduction in time patterns, and introduction of outer loop iterations.

Firstly, in our previous study (Wang et al., 2021), a coarse-to-fine strategy called Coarse Incremental Calibration is proposed to reduce the computational cost. It is also applied here using a coarser grid model to replace the increments between the output from the initial model and the model with modified parameters. Term $H_f(x)$ and $H_c(x)$ are defined as the model output with the fine and coarse grid, respectively. $H_f(x)$ can be approximated with $H_f(x_b) + (H_c(x) - H_c(x_b))$, thus the cost function is represented as:

$$J_o(x) = [Y - H_f(x_b) + H_c(x_b) - H_c(x)]^T R^{-1} [Y - H_f(x_b) + H_c(x_b) - H_c(x)] \tag{4.2}$$

Therefore, GTSM with the fine grid is only simulated to generate the initial model output $H_f(x_b)$. Other simulations in the inner iterations use GTSM with the coarse grid instead, which reduces the computing time to approximately 36% of the original.

Secondly, we consider reducing the dimension of the model output by MOR. The dimension of model output $[H(x_0), H(x_1), ..., H(x_{n+1})]$ and observations y is huge, which requires a huge memory, especially when the model has a long simulation time length. For example, if the number of observations N_s is $O(10^3)$, and with the number of time steps N_t is $O(10^3)$. Then, the dimension of the model output $H(x)$ and observations y is $O(10^6)$. If we assume the parameter dimension n is in the order of $O(10^2)$. The parameter dimension is the length of the vector with the parameters estimated. In this paper, we define spatial subdomains where a single multiplicative adjustment is applied. Each of these subdomains adds an element to the parameter vector. Thus,the dimension of

the model output in the analysis step is $O(10^8)$, such a huge memory usage is unacceptable in practice. Therefore, we apply POD in the time patterns for model output and observations to reduce memory usage in the estimation procedure (that will be further explained in Section 4.2.2).

Thirdly, we use the DUD process in the inner loop to obtain the updated parameters at a lower resolution (see Figure 4.1). With the Coarse Incremental Calibration approach, high resolution GTSM only plays a role as the initial output $H_f(x_b)$ in Eqs. 4.2 while instead by the coarse grid model $H_c(x)$ for iterative update. Even though our previous experiments demonstrate that coarse-grid increments can well represent the fine-grid increments (Wang et al., 2021), the results after the estimation can still be significantly affected by the model with the coarse grid. Therefore, we introduce the outer loop to take the high-resolution model states into account. The updated parameters obtained from the previous converged DUD process are used as the new first guess to update the initial model output. The new cost function can be rewritten as:

$$J_o(x) = [Y - H_f(x_{b_k}) + H_c(x_{b_k}) - H_c(x)]^T R^{-1} [Y - H_f(x_{b_k}) + H_c(x_{b_k}) - H_c(x)] \tag{4.3}$$

where k is the iteration number of the outer loop, x_{b_k} is set to be the optimized parameters $x_{a_{k-1}}$ from the previous DUD process. The estimation process terminates once the cost function has converged.

Compared to the computation-efficient parameter estimation scheme we proposed in the previous study, the estimation scheme in this paper also contributes to memory reduction with the POD algorithm and estimation accuracy improvement by the outer loop iterations. The combination of these methods gives a computation-efficient and memory-reduced parameter estimation framework.

The parameter estimation process with time-POD application and outer loops as shown in Figure 4.1 can be summarized as follows:

1. Define first guess parameter set $[x_0, x_1, ..., x_n]$.

2. Analyze initial model output $H_f(x_b), H_c(x_b)$, determine the corresponding POD reduced model output $\hat{H}_f(x_b), \hat{H}_c(x_b)$ with the truncated basis matrix U_{N_p} (see below).

3. Convert the original observations to corresponding observation $\hat{Y}$ based on the truncated projection matrix.

4. Simulate the coarse grid model with the first guess parameter set, generate the POD reduced model states $[\hat{H}_c(x_0), \hat{H}_c(x_1), \hat{H}_c(x_2), ..., \hat{H}_c(x_n)]$, and evaluate the cost function.

5. Find the new parameters x_* for an approximate linear model that fits exactly through the model output for $[x_0, x_1, ..., x_n]$.

6. If the DUD stop criteria are not satisfied, then perform a model simulation with updated parameters x_* and do model order reduction for model output $\hat{H}_c(x_*)$, and return to step 5.

7. If model outputs with optimization results do not reach the outer loop stop criteria, then return to step 1 with the optimized parameters as a new first guess for the next iteration of the DUD process.

8. Output: optimal estimation of parameters x_a in the last outer loop.

4.2.2 Proper Orthogonal Decomposition (POD) Application

In this Chapter, we provide more detail on the application of POD to reduce model dimension in time patterns. The POD time pattern reduced model is introduced first. Then, we describe the definition of the corresponding observation term and error covariance. Finally, the complete parameter estimation procedure is summarized.

Time-POD Reduced Model

POD reduces the model order by identifying several modes with the most energies from a high-dimension system and uses these modes as a lower-dimension subspace approximation. Usually, the discrete POD is derived with snapshots to find a smaller subspace for states in spatial patterns. A snapshot is the value of the model state vector at a certain time. However, the vast memory requirement in our application comes from the model output $H_f(x)$, $H_c(x)$ and observation Y, containing the data both in space and time patterns in the order of $O(N_s N_t)$. As the simulation time increases, the dimension in time scale N_t is usually much larger than that in the spatial scale N_s. Thus, reducing the order in the time patterns is crucial. In the brief description of model order reduction below, we use $H(x)$ to represent the model output without considering the model resolution in this chapter.

In Chapter 4.2.1, $H(x)$ is a vector representing output in one model simulation for all observation locations and time steps. To better explain the MOR applied to model output of time patterns, we rewrite the vector $H(x)$ into a two-dimensional array $H_{N_t,N_s}(x) = [h^1(x), h^2(x), ..., h^{N_s}(x)] \in \mathbb{R}^{N_t \times N_s}$ to distinguish the time and space fields. $h^i(x)$ is the vector of model output for all time steps at the i^{th} observation location. Now we want to find a projection matrix $K \in \mathbb{R}^{N_t \times N_t}$ from $\mathbb{R}^{N_t}$ to a smaller subspace which minimizes the error:

$$||H_{N_t,N_s}(x) - KH_{N_t,N_s}(x)||_2^2 = \Sigma_{i=1}^{N_s} ||h^i(x) - Kh^i(x)||_2 \tag{4.4}$$

where an optimal orthonormal projection matrix K is given by:

$$K = U_{N_p} U_{N_p}^T \tag{4.5}$$

$U_{N_p} = [\mathrm{u}_1, \mathrm{u}_2, ...\mathrm{u}_{\mathrm{N_p}}] \in \mathbb{R}^{\mathrm{N_t} \times \mathrm{N_p}}$ is an orthogonal matrix containing the N_p eigenvectors of the correlation matrix $H_{N_t,N_s} H_{N_t,N_s}^T$ corresponding to the N_p largest eigenvalues, starting from the largest eigenvalue corresponding to u_1 in decreasing order. The POD modes are the optimal ordered orthogonal matrix of basis vectors U_{N_p} in the least square sense. The truncated Singular Values Decomposition (SVD) is applied to derive the POD modes.

It is the factorization of the matrix that generalizes the eigen decomposition via an extension of the polar decomposition:

$$H_{N_t,N_s}(x) = U\Sigma V^T \tag{4.6}$$

where, $U = [u_1, u_2, ...u_{N_t}] \in \mathbb{R}^{N_t \times N_t}$ and $V = [v_1, v_2, ...v_{N_s}] \in \mathbb{R}^{N_s \times N_s}$ are the orthogonal matrices, $\Sigma \in \mathbb{R}^{N_t \times N_s}$ is a diagonal matrix with rank r and diagonal value $\sigma_1, \sigma_2, ...\sigma_r$ are the singular values of H_{N_t,N_s}. Therefore, a new matrix $\hat{H}_{N_p,N_s}$ can be defined by projecting the model output onto a smaller subspace using the truncated orthogonal matrices U_{N_p}, it is:

$$\hat{H}_{N_p,N_s}(x) = U_{N_p}^T H_{N_t,N_s}(x) \in \mathbb{R}^{N_p \times N_s} \tag{4.7}$$

We define the truncated orthogonal matrices $U_{N_p} \in \mathbb{R}^{N_t \times N_p}$ by keeping the first N_p columns of the matrix U, which correspond to the N_p modes with the highest energy of the dynamic system. In general, $\hat{H}_{N_p,N_s}(x)$ has a much smaller dimension compared to the model output $H_{N_t,N_s}(x)$, while retains the most important features. After the time-POD application, the two dimensional matrix $\hat{H}_{N_p,N_s}(x)$ is reshaped into the vector $\hat{H}(x)$ with a dimension of $O(N_p N_s)$:

$$\hat{H}(x) = \begin{bmatrix} U_{N_p}^T h^1(x) \\ U_{N_p}^T h^2(x) \\ \vdots \\ U_{N_p}^T h^{N_s}(x) \end{bmatrix} \tag{4.8}$$

$\hat{H}(x)$ is defined as the reduced model output vector used for the parameter estimation process.

Observation Term Definition

In Chapter 4.2.2, the order of model output has been reduced to a corresponding model $\hat{H}_{N_p,N_s}(x)$ with a set of data identified on time patterns instead of the real time-series. To match the model output matrix formula, we denote a two-dimensional array $Y_{N_t,N_s} = [y^1, y^2, ..., y^{N_s}] \in \mathbb{R}^{N_t \times N_s}$ as the observation term that y^i is a vector containing time series in i^{th} location, we have:

$$\hat{Y}_{N_p,N_s} = U_{N_p}^T Y_{N_t,N_s} \tag{4.9}$$

The truncated basis matrix U_{N_p} used here is from the initial model since both the model and observations have a strong resemblance to the tidal constituents in time patterns. The projection and reconstruction accuracy is further analyzed in Section 4.3.2. The reduced observation vector $\hat{Y}$ is:

$$\hat{Y} = \begin{bmatrix} U_{N_p}^T y^1 \\ U_{N_p}^T y^2 \\ \vdots \\ U_{N_p}^T y^{N_s} \end{bmatrix} \tag{4.10}$$

The observation error term has to be identified corresponding to the reduced observation term. We define the covariance of observation error at i^{th} location over all time steps as follows:

$$R^i = E([y^i - E(y^i)][y^i - E(y^i)]^T) \tag{4.11}$$

where $E(y^i) = y_t^i$ is a vector of the except values at all discrete times at location i. The POD based observation error covariance $\hat{R}^i$ is:

$$\begin{aligned} \hat{R}^i &= E([\hat{y}^i - \hat{y}_t^i][\hat{y}^i - \hat{y}_t^i]^T) \\ &= E([U_{N_p}^T y^i - U_{N_p}^T y_t^i][U_{N_p}^T y^i - U_{N_p}^T y_t^i]^T) \\ &= U_{N_p}^T R^i U_{N_p} \end{aligned} \tag{4.12}$$

In this application, we assume observation error is time invariant. The covariance matrix R^j is a diagonal matrix with σ^2 as diagonal values (σ is the observation uncertainty and we set its value as $0.05m$ in this application), so $R^j = \sigma^2 I_{(N_t)}$. Therefore, after the model order reduction, the new observation error covariance for location i is $\hat{R}^j = \sigma^2 I_{(N_p)}$. $\hat{R}$ is the diagonal matrix including observation error covariance at all observation locations. We rewrite the cost function with the order reduced model output and observation terms as follows:

$$J_o(x) = \frac{1}{2}[\hat{Y} - \hat{H}_f(x_{b_k}) + \hat{H}_c(x_{bk}) - \hat{H}_c(x)]^T \hat{R}^{-1}[\hat{Y} - \hat{H}_f(x_{b_k}) + \hat{H}_c(x_{b_k}) - \hat{H}_c(x)] \tag{4.13}$$

4.3 Numerical Experiments and Results

In this chapter, we firstly describe the experiment configuration, including the parameter selection, model setup, observations, and the setup of three experiments. Secondly, to assess the performance of POD, we evaluate the projection and reconstruction accuracy for model output and observations, followed by the comparison of estimation results with two weeks simulation. The final estimation results are also analyzed.

4.3.1 Experiment Set-up

In this study, GTSM has the same model set-up as that we used in Chapter 2 to estimate bathymetry with 110 subdomains. 1973 time-series from the FES2014 dataset is used for calibration and the UHSLC dataset is applied for validation. We use a simulation time of two weeks, between 1 to 14 January 2014, to compare the estimation performance with and without the POD model reduction. After that, the final model estimation covers the simulation of two spring-neap cycles (1 month) with POD and outer loop application. Therefore, the simulation starts from 1 to 31 January 2014 with a two-week spin-up before January 1. The time interval is set as 10 minutes, which results in 4465 time steps.

Three experiments are set up to investigate the performance of the time-POD parameter estimation scheme for GTSM, as Table 4.1 shows. EX1 is the experiment with a short

Table 4.1: Experiments set-up

Name	Simulation Time	Time steps	Outer loop	POD	Truncation size	Data size before POD	Data size after POD
EX1	1 - 14 Jan.	2017	No	No	N/A	3.32GB	N/A
EX2	1 - 14 Jan.	2017	No	Yes	200	3.32GB	0.33GB
EX3	1 - 31 Jan.	4465	Yes	Yes	200	7.35GB	0.33GB

simulation time of two weeks without POD implementation and the outer loop. It is very similar to the experiment in Approach 2 in Chapter 3. The memory needed for the total model output in this scheme to estimate 110 parameters is approximately 3.5GB. EX2 has the same settings as EX1 but with the implementation of POD. It aims to evaluate the influence on the accuracy by applying POD, the memory use is significantly reduced when compared to EX1. Finally, the experiment denoted as EX3 follows the parameter estimation scheme in Figure 4.1, covering a 1-month simulation time length from 1 to 31 January 2014. Without MOR, the data size of $[H_c(x_0), H_c(x_1), ..., H_c(x_n)]$ and observation was about 7.35GB, and the total memory use was more than 20GB for this experiment. With the proposed POD approach, the memory use is sharply reduced to 4.5% after the POD application.

4.3.2 Time-POD Performance Analysis

Reconstruction Accuracy

The accuracy of parameter estimation with MOR depends on the reconstruction accuracy of the model output and observations. The reconstructed model output and observation terms are in the formula of $U_{N_p} U_{N_p}^T H_{N_s,N_t}(x)$ (the term $KH_{N_s,N_t}(x)$ in Eqs.4.4) and $U_{N_p} U_{N_p}^T Y$. The basis matrix U_{N_p} is obtained by truncated SVD from the initial model output or observations. Figure 4.2 shows the Root Mean Square Error (RMSE) between the original and the reconstructed model output (observation) with different number of modes. Time series is from 1 to 31 January 2014.

In general, the RMSE is decreased with the increase of the truncation size. Basis matrix from observation (Figure 4.2c) shows slower downtrends than others (Figure 4.2a, 4.2b). One possible reason is the model has more tidal components that are not included in the observations, there are 32 tidal constituents in observations while 58 tide potential frequencies are in the model. But that will not affect the estimation results because the RMSE for reconstructed model and observations without truncation is less than $5 \times 10^{-4} m$. It means the missing components in observation would lead to at most $5 \times 10^{-4} m$ water level changes while the observation error we defined is $0.05m$, which is 100 times larger. Figure 4.2a shows the excellent accuracy of the reconstructed coarse model. The reconstructed fine model and observations have similar performance when the truncation size varies. Figure 4.2b is opposite to Figure 4.2a for the coarse model. We use the basis matrix from the coarse model with 200 modes for the calibration process because most of the model simulation in the estimation iteration is on the coarse grid.

Reducing the coarse model output with 200 modes sharply reduces the data size, while the high accuracy for the coarse model with RMSE of $2.64 \times 10^{-4} m$ is attained and the reconstructed observation error is also smaller than the observation uncertainty.

Tidal analysis can also be used to reduce the data size, but in comparison, the time-pattern projection has two advantages. Firstly, tidal analysis requires the selection of a set of tidal constituents. These constituents should respect the Rayleigh criterion. The projection method has only one parameter to which is quite insensitive. For example, time-series of reconstructed model output and observations for modes 1 to 3 (Figure 4.3a-4.3c) in an observation location provide similar waves to the harmonic, implying the patterns in the projection method work similarly as the tide analysis does but without the restriction to separating the independent tide components. Secondly, the projection method gives almost identical results to the time-series approach. The reconstructed fine grid model output with projection on the first three modes (Figure 4.3d) is close to the original data. When more modes are included, the reconstruction error would become very small. We also performed a tidal analysis for the time series from the model output for this location and after projection onto modes 1- 3, as shown in Table 4.2. The projection on modes 1 and 2 mainly shows large amplitudes for the semi-diurnal tides (N2, M2, S2, K2). The contributions from N2 and M2 add up to a large part of the N2, M2 signal, while this is a bit less for S2 and K2. Mode 3 mainly shows diurnal constituents, where the P1 and K1 amplitudes are close to the values for the full signal. The time projection thus shows some resemblance to tidal analysis.

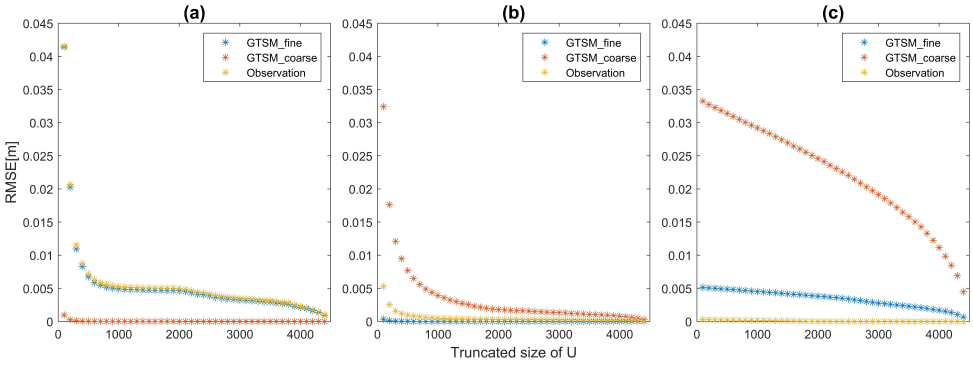

Figure 4.2: RMSE between the initial model output $H(X)$ and reconstructed model output $\hat{H}(x)$ for various truncation sizes (unit: m). With the projection basis vectors derived from (a) initial coarse model; (b) initial fine model; (c) observations.

Experiments with Time-POD Application

Figure 4.4 shows the cost function (Figure 4.4a) and optimized bathymetry correction factors of EX1 (Figure 4.4b) and EX2 (Figure 4.4c). EX2, estimation with time-POD, shows a similar behavior of the cost function in each iteration as EX1 and nearly the same correction factors. The RMSE for both experiments decreases from 5.23cm to 3.49cm in the calibration period, while the required memory in EX2 is reduced by a factor of 10.

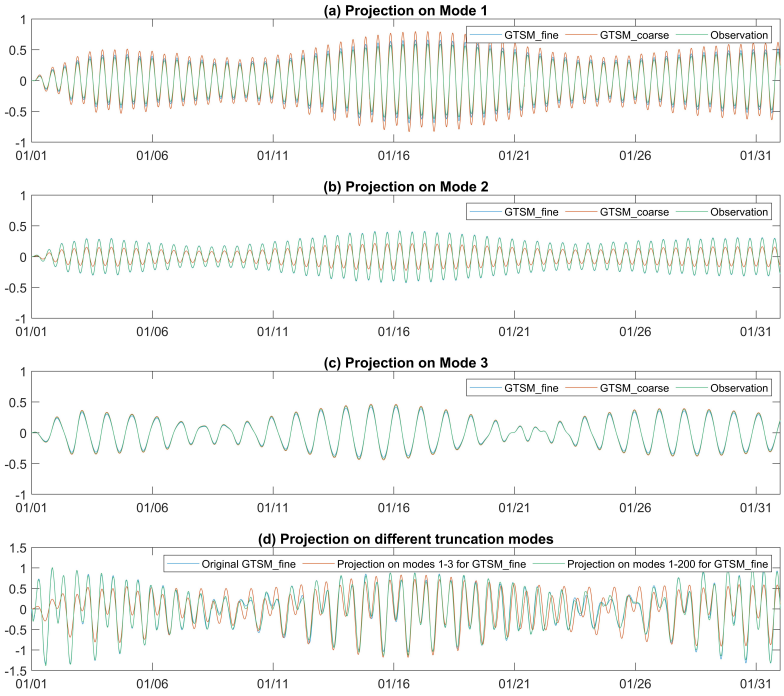

Figure 4.3: Time series of the model output and observation with projection in the observation location (70.1110°S, 23.1397 °W). (a) Projection on Mode 1; (b) Projection on Mode 2; (c) Projection on Mode 3; (d) Projection on different truncation modes.

Figure 4.5 illustrates the the difference of RMSE at different observation locations between the initial model and the estimated model in EX2 (i.e., RMSE between the initial model and observations - RMSE between the estimated model and observations). It reports nearly the same improvement after the estimation as in EX1 (not shown here). Therefore, model order reduction is an efficient approach to reduce memory requirements for parameter estimation without causing any loss of estimation accuracy.

The purpose of parameter estimation is to improve the GTSM long-term forecast accuracy. However, the interaction of tidal constituents varies during different periods. For example, the RMSE between estimated model output and observations is 3.49cm from 1 to 14 January, while the RMSE in the forecast increases to 4.33cm for the period from 15 to 31 January 2014. A short simulation time length would lead to over-fit the data in the estimation period (Wang et al., 2021). After assessing model order reduction performance, we selected a longer simulation time of 1 month and perform experiments in Chapter 4.3.3.

Table 4.2: The amplitude of eight major tide components from tide analysis for the time-series of the original GTSM with fine grid and the projection on mode 1-3 for the arbitrary location in (cm): (70.1110°S, 23.1397 °W).

Components	Q1	O1	P1	K1	N2	M2	S2	K2
GTSM with fine grid	7.2	26.06	7.18	21.89	6.34	46.74	33.73	9.58
Projection on mode 1	0.22	1.73	0.77	2.35	8.54	40.92	12.10	3.44
Projection on mode 2	0.23	0.53	0.30	0.90	5.51	26.10	8.05	2.29
Projection on mode 3	4.89	15.33	6.96	21.21	0.80	2.31	1.92	0.54

4.3.3 Parameter Estimation Results Analysis

EX3 covers a simulation time length of 1 month for GTSM to estimate bathymetry. Figure 4.6a illustrates the changes in the cost function in each simulation in the three outer loop iterations. In every outer loop, the cost functions of the first 111 runs include one initial simulation and 110 independent simulations each corresponding to perturbing one of the 110 parameters. Parameters are iteratively updated after the first 111 simulations. The simulation experiment was run using 200 cores for about 12 days, with a total of approximately 57600h CPU times.

In the first outer loop (color red in Figure 4.6a), the cost function has a sharp reduction from 7.21×10^6 to 3.17×10^6 and then slowly reduced to 3.00×10^6 at the end of the second outer loop (color blue). Compared with the first outer loop, the cost function in the second outer loop only reduces slightly. It looks that the estimation results are converged. In the third out loop, the difference of cost functions in each simulation is very slight, making the DUD process difficult to continue, leading to a stop after several iterations with a value of 2.95×10^6. It is in the same magnitude as that in the second outer loop. GTSM parameter estimation system converged in the third outer loop iteration. Moreover, sensitivity for each parameter can be observed from the variability of the cost function for the initial 111 perturbation runs in each outer loop. This is strongly decreased in the third outer loop, indicating that the estimated parameters are close to the minimum. The final relative change to the bathymetry, which is the correction factor $[x]$ in Eqs. 3.8 is shown in Figure 4.6b. The value varies between -0.1 to 0.1 within the range of hard constraints.

Estimation performance is analyzed by comparing the model output with the FES2014 dataset. For the comparison of the model performance in EX3 and EX1, RMSE of two time periods is summarized in Table 4.3. RMSE is used to represent the difference between model output and observations to access model performance. The bias difference between model and observations is negligible (not shown here). As expected, GTSM with the fine grid has better performance than that with the coarse grid. Comparing the coarse grid GTSM, EX3 works better than EX1 in all outer loops and time periods. In the fine grid GTSM, EX1 performs slightly better than EX3 in the period 1 to 14 January but worse in 15 to 31 January 2014. This can be explained that EX1 estimates with a two-week simulation time (1 to 14 January 2014) resulting in an over-fitting of data in the calibration period. The RMSE is reduced from 5.23cm to 3.49cm in the period 1 to 14 January, while the reduction in the period 15 to 31 January is clearly less, from 5.84cm to

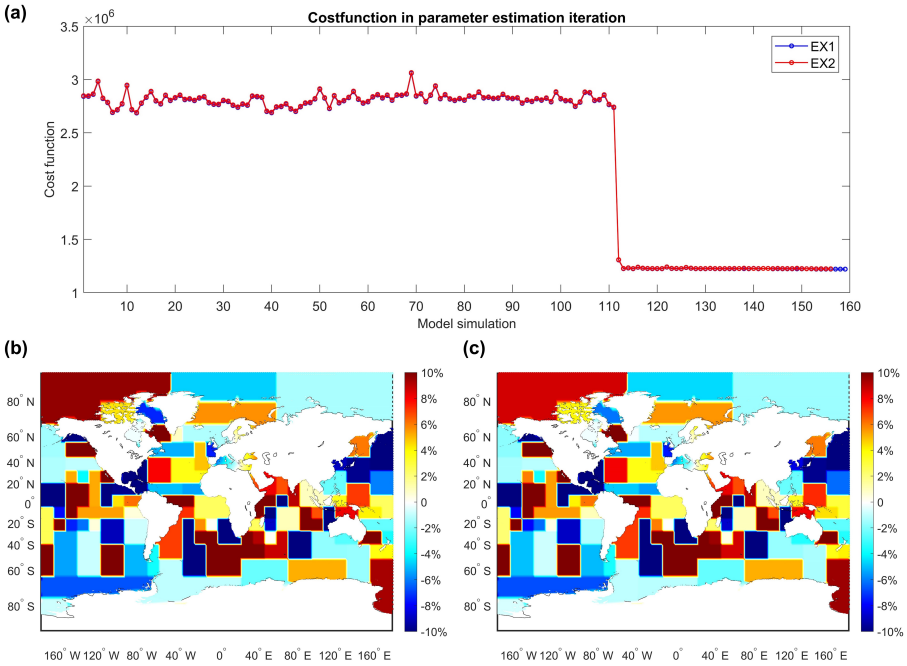

Figure 4.4: (a) Cost function in EX1 and EX2. Relative adjustments of Bathymetry as estimated in EX1 (b) and EX2 (c). Positive values show a deepening.

4.33cm in the 15 to 31 January. With a longer simulation time length of 1 month in EX3, the RMSE of the estimated fine model in these two periods is close to each other, namely 3.62cm and 3.66cm, implying the overfitting is reduced.

The spatial distribution of RMSE for the fine GTSM in January is shown in Figure 4.7. Figure 4.7a is the RMSE between the estimated fine grid model output in EX3 and FES2014 observations. The differences of RMSE between the model before and after the estimation are shown in Figure 4.7b. It can be observed that the estimated model has been significantly improved in most regions. A few areas that are not improved or a bit worse than the initial model, see the areas with yellow colors (negative values of RMSE difference) in Figure 4.7b. Possibly, not only bathymetry but also other effects such as the lack of resolution, play a role here. The regions getting worse only takes up a small part of the ocean. In addition, estimation by EX3 outperforms EX1 in most ocean sea, as Figure 4.7c shows. Generally, the estimated model significantly overperforms the initial model.

In summary, the calibrated model in EX3 is in better agreement with the measurements than EX1. Model order reduction reduces the memory requirement by a factor of 22 while keeping the same estimation accuracy as without model order reduction. Long simulation time is beneficial for parameter estimation in GTSM, and the implementa-

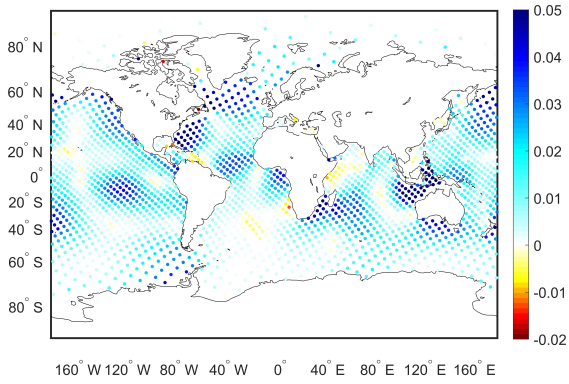

Figure 4.5: RMSE difference between the initial model and estimated model in EX2 in the period from 1 to 14 January 2014, color blue shows the improvement. [unit:m]

Table 4.3: RMSE between GTSM and FE2014 datasets in difference time periods [cm]

Model	Time period	Initial	EX1	EX3_1[a]	EX3_2[a]	EX3_3[a]
GTSM	January 1-14	6.47	4.19	4.08	4.02	4.06
(coarse)	January 15-31	7.14	5.20	4.53	4.39	4.41
GTSM	January 1-14	5.23	3.49	3.67	3.62	3.62
(fine)	January 15-31	5.84	4.33	3.80	3.66	3.66

[a] EX3_1, EX3_2, and EX3_3 represent the $1^{st}, 2^{nd}, 3^{rd}$ outer loop in EX3.

tion of the outer loop further improves the tide forecast accuracy.

4.4 Model Validation

Model validation is necessary to ensure the model is independent from the simulation period and data we used in the estimation procedure. We analyzed the tide components from GTSM and compared them against the FES2014 dataset in the frequency domain. The tide forecast of GTSM for the whole year of 2014 is also compared with observations from the FES2014 and UHSLC datasets.

4.4.1 Tide Analysis Comparison against FES2014 Dataset for 2014

Model performance is evaluated in the frequency domain. Tide forecast from GTSM in the year 2014 for 1973 observation locations is analyzed with TIDEGUI software. We use the Root-mean-square (RMS) to assess the difference between model output and observations for major tide components. Detailed results for 8 major tide components

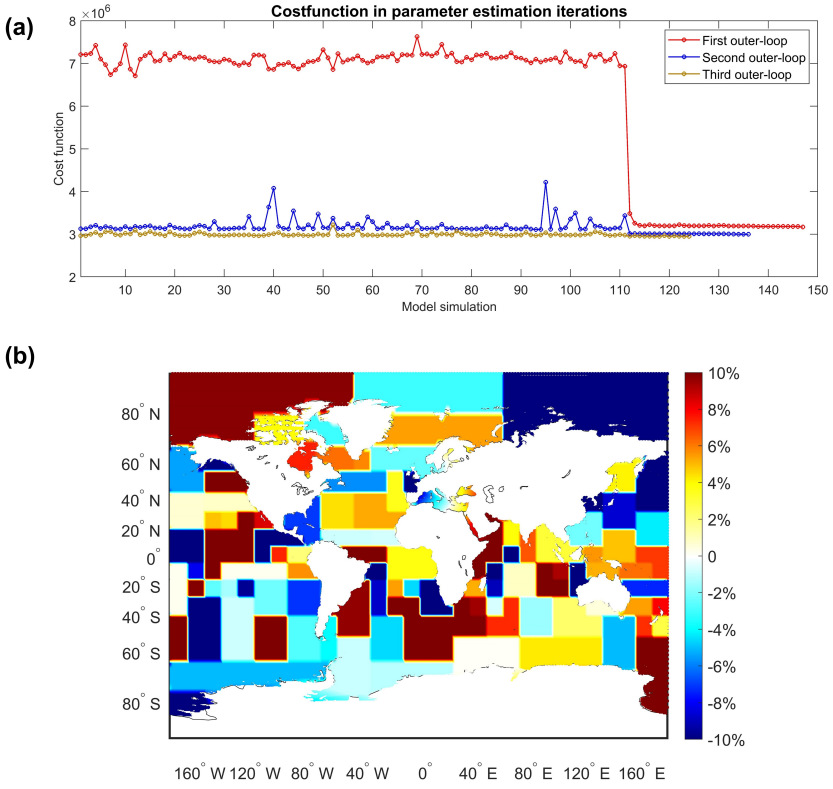

Figure 4.6: (a) Changes of the cost function values in the three outer loop iterations of EX3; (b) Relative adjustments of the bathymetry as estimated in EX3; Positive values show a deepening.

are summarized in Table 4.4. Root-sum-square (RSS) for these 8 constituents is also analyzed.

It can be observed that RSS and RMS for all 8 major components are reduced after the estimation in EX1 and three outer loop iterations of EX3 when comparing with the initial model. After the estimation, M2 is the component that significantly improved in EX3 reduced from 4.50cm to 1.89cm whereas it is 2.54cm in EX1. The other 7 components in EX3 are nearly the same or slightly better than in EX1. The RSS over these eight components in EX3 is reduced from 6.05cm to 3.52cm.

The differences in the amplitude and phase between the model output and FES2014 dataset for M2 component is shown in Figure 4.8. The difference in amplitudes and phases compared to FES2014 dataset is much smaller for the estimated models in EX1 and EX3 than for the initial model. EX3 has a better agreement with FES2014 dataset than EX1, especially in the phase domain (Figure 4.8e, 4.8f), consequently EX3 has a smaller RMS than EX1.

Initial GTSM performs better in deep ocean comparing with Deep-Ocean Bottom

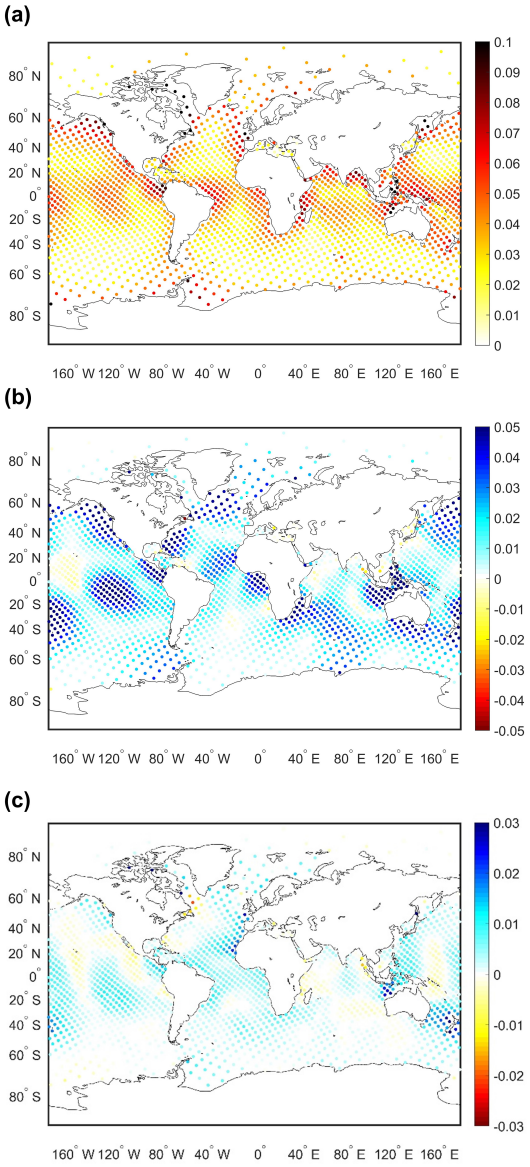

Figure 4.7: (a) RMSE between estimated fine grid GTSM in EX3 and FES2014 dataset in January 2014; (b) Difference of RMSE between the initial model and the estimated model, color blue shows the improvement; (c) Difference of RMSE between model after estimation in EX1 and EX3, color blue shows EX3 outperforms EX1. [unit: m]

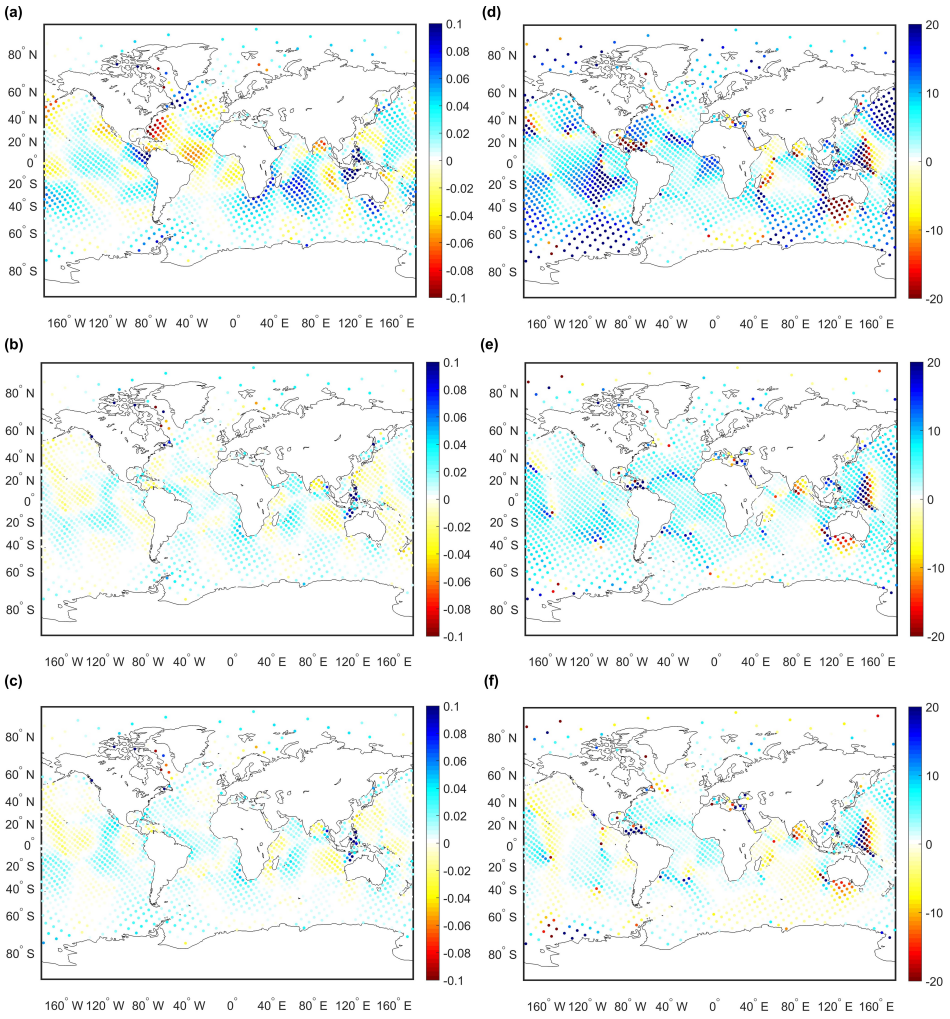

Figure 4.8: Spatial distribution of amplitudes and phase difference of M2 between model and FES2014 dataset. (a) (b) (c): Amplitudes difference for initial GTSM, model estimated in EX1 and EX3, respectively [unit: m]. (d) (e) (f): Phases difference for initial GTSM, model estimated in EX1 and EX3, respectively [unit: degree].

Table 4.4: RSS and RMS of eight major tide components between the fine GTSM and FES2014 dataset in (cm)

	RMS for all locations								RSS
Components	Q1	O1	P1	K1	N2	M2	S2	K2	
Initial	0.48	1.12	0.55	1.62	1.01	4.50	2.79	1.76	6.05
EX1	0.44	0.96	0.41	1.18	0.66	2.54	1.91	1.46	3.92
EX3_1	0.46	1.00	0.45	1.31	0.62	2.02	2.00	1.42	3.68
EX3_2	0.46	0.99	0.43	1.25	0.61	1.91	1.90	1.39	3.53
EX3_3	0.46	1.00	0.43	1.25	0.62	1.89	1.89	1.38	3.52

Pressure Recorder (BPR) observation than most of the purely hydrodynamic models described in Table 3 of Stammer et al. (2014), but not as accurate as the assimilative tide models (Wang et al., 2021). In this study, GTSM is significantly improved after our parameter estimation to bathymetry in the deep ocean. It outperforms the purely hydrodynamic models, especially in the M2 constituent, but still not better than the assimilative tide models. This result is expected because firstly observation locations are limited in the estimation process, and secondly not only bathymetry but other effects such as resolutions, other parameters like bottom friction would also affect the model performance. However, compared to other tide models, GTSM after parameter estimation has the advantage to access the effect of sea level rise and climate changes because it can include surge simulation when meteorological forcing wind and air pressure additions are added. Therefore, the high accuracy tide representations also benefit the complete water level forecast.

4.4.2 Monthly Comparison against FES2014 Time Series for 2014

GTSM is also validated through long-term tide forecasts, showing the model performance in different time periods. Model forecast in the whole year of 2014 is firstly analyzed with the FES2014 dataset. Figure 4.9 shows the regional RMSE of the fine GTSM after the estimation in EX1 and EX3 for each month of year 2014. The regional RMSE between GTSM with the fine grid and FES2014 dataset are shown in Figure 4.9a-g. The global average of RMSE in 1973 locations is shown in Figure 4.9h.

Compared to the initial model, the RMSE for all the regions is significantly reduced in EX1 and EX3. RMSE in EX1 is larger than that in EX3 in the year 2014, except for some months in the Indian Ocean. Forecast results also report that estimation with a longer simulation length works better than that with a short time window When comparing the RMSE in EX1 and the first outer loop of EX3. As the number of outer loop iterations increases, the model performs better throughout 2014. The 1-year forecast comparison with the FES2014 dataset demonstrates the estimated model can be used for the high-accuracy long-term forecast.

One can also observe a seasonal pattern in the RMSE in Figure 4.9, both before and after the calibration. A possible reason is that tide constituents interact differently for

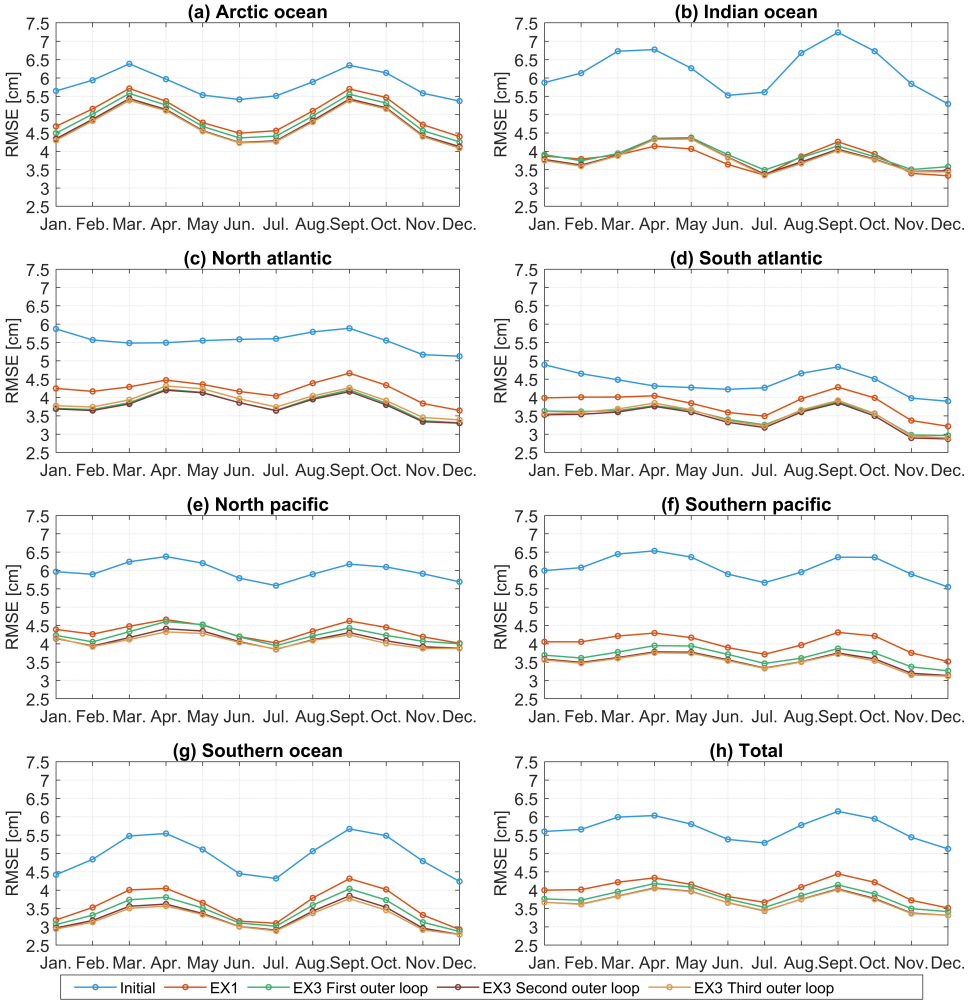

Figure 4.9: RMSE between model output and FES2014 dataset in 2014.

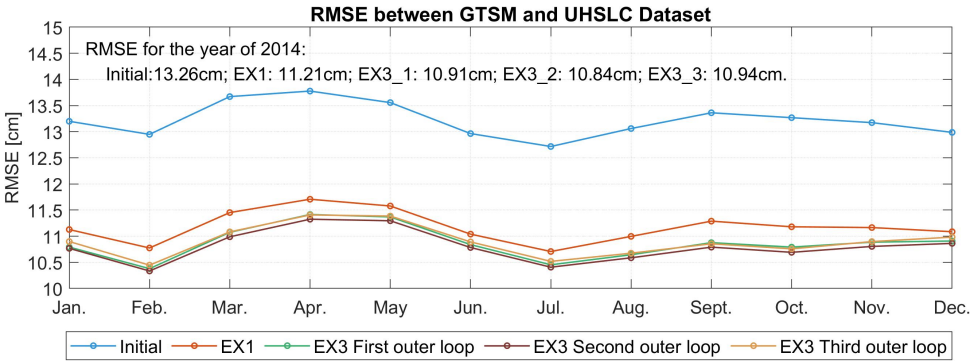

Figure 4.10: RMSE between model output and UHSLC dataset in 2014

different periods, leading to a large or small difference between the data and the model for each month. After calibration, this seasonal pattern is smaller in EX3 than EX1, indicating long simulation time length can weaken it and result in a better agreement to model and observations. However, it remains challenging to verify whether using a more extended time period such as one year can further improve the model accuracy and eliminate over-fitting due to the excessive computational demand. But we see no clear signals of over-fitting problem in EX3, and the 1-month calibration provides sufficient calibration accuracy.

4.4.3 Monthly Comparison against UHSLC Time Series for 2014

In the following, the performance of GTSM is assessed using a dataset that is not used in the estimation stage. Model performance in the coastal areas is evaluated by comparing with the UHSLC dataset in 2014.

Figure 4.10 shows the monthly averaged RMSE in 2014 between model output and the UHSLC measurement. The RMSE before the estimation is approximately 12.5-14 cm in each month and it is reduced to about 10-11.5cm after the estimation in both EX1 and EX3. It indicates the bathymetry estimation for the deep ocean can improve the accuracy in the nearshore. As expected, the results in EX3 are better than in EX1. The difference between the three outer loops is not significant, but the second outer loop is slightly better than the third outer loop. It can also be observed from the mean RMSE of the whole year of 2014 (Figure 4.10), the second loop has a value of 10.84cm smaller than the third outer loop with 10.94cm. One possible reason is the bathymetry estimation mainly works on the deep ocean and some other parameters, such as bottom friction coefficient, play an important role in the coastal regions. After three outer loop iterations, the parameter estimation overfits a bit the deep water observation used in the calibration process. Also, some other effects, such as bottom friction, play a role in shallow waters, but they are left out of consideration in this study. Future works can continue on the parameter estimation for shallow waters.

Figure 4.11 shows the spatial distribution of RMSE between the initial fine model and UHSLC dataset in the year of 2014 (Figure 4.11a) and the RMSE difference between the

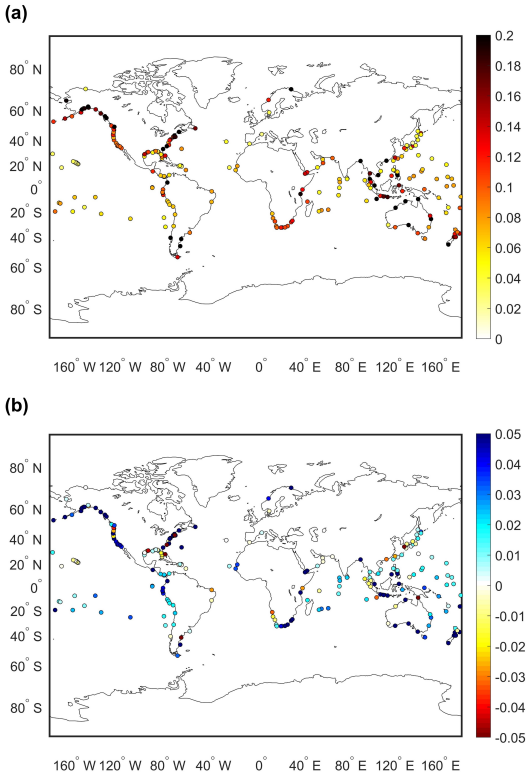

Figure 4.11: (a): RMSE between initial fine GTSM and UHSLC dataset in year 2014; (b): RMSE Difference between initial model and estimated model in EX3, color blue shows improvement.[unit:m]

model before and after estimation in EX3 (Figure 4.11b). Results in EX1 reported similar distribution as EX3 but with a slightly higher RMSE (not shown here). Most of the tide gauges are located in coastal areas with larger RMSE than deep oceans. After the global calibration, model performance near the coast is improved even though the calibration mainly focuses on the deep water.

To further have a closer look at the tide representation in one location, the time series of station Wellington Harbour in New Zealand is used as an example. Figure 4.12a shows the tide representation from the UHSLC dataset, the model output of the initial, EX1, and EX3. The difference between model output and observation is depicted in Figure 4.12b. The RMSE for the initial model is 15.25cm, and after the estimation in EX1, it is decreased by approximately 44.2% to 8.51cm. EX3, with the RMSE reduction of approximately 59.21%, is marginally better than in EX1.

The model validation for the whole year of 2014 shows excellent agreement with the FES2014 and UHSLC datasets in frequency and time domains after applying the memory-efficient estimation. It illustrates that GTSM with the adjusted bathymetry can

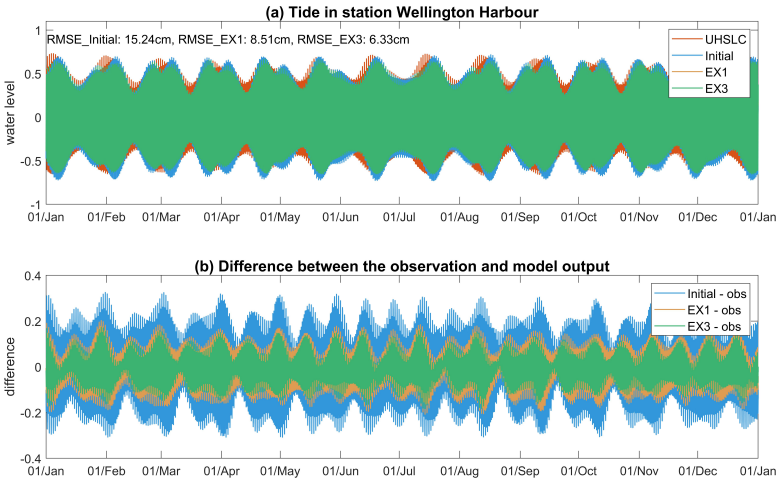

Figure 4.12: (a): Tide representation for station Wellington Harbour in year 2014; (b): Difference between different GTSM models with the fine grid and observation. Wellington Harbour is a location with coordinate of (41.28°S,174.78°E) in the New Zealand.

provide high accuracy long-term tide forecast.

4.5 Conclusions

This study presented a memory-efficient parameter estimation approach for the high-resolution global tide model over a long time length. To resolve the memory constraint of the long period model simulation, time-POD model order reduction is developed to project the model output time patterns onto a smaller subspace. To further improve the model estimation accuracy with affordable computational cost, we implemented inner-outer loop iterations, similar to Incremental 4D-var, using an iterative parameter estimation algorithm called DUD in the inner loop with the lower-resolution model simulation. The outer loop uses optimized parameters from the previous inner DUD process as a new reference run with the initial high-resolution model. This parameter estimation scheme is implemented for the Global Tide and Surge Model (GTSM) to correct bathymetry and substantially improve the model performance.

Our previous investigation showed that the accuracy of the calibrated model would probably benefit from a calibration period longer than the two weeks (one spring-neap cycle) used there, but the huge memory required was limiting an extension in practice. Here, we use time-POD model order reduction to project the GTSM output onto a limited number of time patterns. This projection reduces the memory usage by more than an order of magnitude in our experiments, while our experiments for GTSM show that parameter estimation with MOR achieves the same model accuracy as without MOR. This approach has the advantage of keeping the reduced model output size small when extending the simulation time length.

Finally, a parameter estimation experiment for GTSM with the implementation of

MOR and inner-outer loop iterations is performed. It covers a simulation time of 1 month while memory demand is reduced by a factor of 22 due to model order reduction for time fields. Experiment results show that the ocean tide is better represented in the calibration period. The cost function is converged within three outer loop iterations in this study. Model validation from the frequency domains illustrates the M2 component is significantly better estimated with the set-up of 1-month simulation length and the outer loop implementation. Model tide forecast in the whole year of 2014 is compared with the FES2014 and UHSLC datasets. It demonstrates that a long simulation period in the estimation procedure improves the performance for long-term tide forecasting. The outer loop iterations contribute to further improvement of the model forecast but can lead to a bit of overfitting to the data in the third outer loop.

In summary, parameter estimation leads to significant performance improvements for GTSM. The memory requirements are significantly reduced, which allowed us to extend the time span used for calibration. This resulted in a more accurate reproduction of tides in GTSM. Bathymetry calibration contributes more to the deep ocean but also benefits a bit for shallow waters. In addition, this parameter estimation scheme can also be used to calibrate different parameters simultaneously (e.g., bathymetry, internal tide friction and bottom friction combined), in particular, to estimate the bottom friction in shallow water with more tide gauge data.

Bibliography

Antoulas, A., Ionutiu, R., Martins, N., Maten, ter, E., Mohaghegh, K., Pulch, R., Rommes, J., Saadvandi, M., & Striebel, M. (2015). *Model order reduction : Methods, concepts and properties*. Technische Universiteit Eindhoven.

Beck, A., & Ehrendorfer, M. (2005). Singular-vector-based covariance propagation in a quasigeostrophic assimilation system. *Monthly Weather Review*, *133*(5), 1295–1310. https://doi.org/10.1175/MWR2909.1

Cane, M. A., Kaplan, A., Miller, R. N., Tang, B., Hackert, E. C., & Busalacchi, A. J. (1996). Mapping tropical pacific sea level: Data assimilation via a reduced state space kalman filter. *Journal of Geophysical Research: Oceans*, *101*(C10), 22599–22617. https://doi.org/10.1029/96JC01684

Cao, Y., Zhu, J., Navon, I. M., & Luo, Z. (2007). A reduced-order approach to four- dimensional variational data assimilation using proper orthogonal decomposition. *International Journal for Numerical Methods in Fluids*, *53*(10), 1571–1583. https://doi.org/10.1002/fld.1365

Cazemier, W., Verstappen, R. W. C. P., & Veldman, A. E. P. (1998). Proper orthogonal decomposition and low-dimensional models for driven cavity flows. *Physics of Fluids*, *10*(7), 1685–1699. https://doi.org/10.1063/1.869686

Chatterjee, A. (2000). An introduction to the proper orthogonal decomposition. *Current Science*, *78*(7), 808–817. http://www.jstor.org/stable/24103957

Chen, Y., & Oliver, D. S. (2013). Levenberg–marquardt forms of the iterative ensemble smoother for efficient history matching and uncertainty quantification. *Computational Geosciences*, *17*, 689–703.

Courtier, P., Thépaut, J.-N., & Hollingsworth, A. (1994). A strategy for operational implementation of 4d-var, using an incremental approach. *Quarterly Journal of the Royal Meteorological Society*, *120*(519), 1367–1387. https://doi.org/10.1002/qj.49712051912

Daescu, D. N., & Navon, I. M. (2008). A dual-weighted approach to order reduction in 4dvar data assimilation. *Monthly Weather Review*, *136*(3), 1026–1041. https://doi.org/10.1175/2007MWR2102.1

Emerick, A. A., & Reynolds, A. C. (2013). Ensemble smoother with multiple data assimilation [Ensemble Kalman filter for data assimilation]. *Computers Geosciences*, *55*, 3–15. https://doi.org/https://doi.org/10.1016/j.cageo.2012.03.011

Evensen, G. (1994). Sequential data assimilation with a nonlinear quasi-geostrophic model using monte carlo methods to forecast error statistics. *Journal of Geophysical Research: Oceans*, *99*(C5), 10143–10162. https://doi.org/10.1029/94JC00572

Evensen, G., & van Leeuwen, P. J. (2000). An Ensemble Kalman Smoother for Nonlinear Dynamics. *Monthly Weather Review*, *128*(6), 1852–1867. https://doi.org/10.1175/1520-0493(2000)128<1852:AEKSFN>2.0.CO;2

Farrell, B. F., & Ioannou, P. J. (2001). State estimation using a reduced-order kalman filter. *Journal of the Atmospheric Sciences*, *58*(23), 3666–3680. https://doi.org/10.1175/1520-0469(2001)058<3666:SEUARO>2.0.CO;2

Jolliffe, I., & Cadima, J. (2016). Principal component analysis: A review and recent developments. *Philosophical Transactions of the Royal Society A: Mathematical, Physical and Engineering Sciences*, *374*, 20150202. https://doi.org/10.1098/rsta.2015.0202

Kopp, G. A., FerreÂ´, J. A., & Giralt, F. (1997). The Use of Pattern Recognition and Proper Orthogonal Decomposition in Identifying the Structure of Fully-Developed Free Turbulence. *Journal of Fluids Engineering*, *119*(2), 289–296. https://doi.org/10.1115/1.2819133

Kosambi, D. D. (1943). Statistics in function space. *Journal of the Indian Mathematical Society*, *7*, 76–88.

Liang, Y., Lee, H., Lim, S., Lin, W., Lee, K., & Wu, C. (2002). Proper orthogonal decomposition and its applications part i: Theory. *Journal of Sound and Vibration*, *252*(3), 527–544. https://doi.org/https://doi.org/10.1006/jsvi.2001.4041

Lin, B., & McLaughlin, D. (2014). Efficient characterization of uncertain model parameters with a reduced-order ensemble kalman filter. *SIAM Journal on Scientific Computing*, *36*(2), B198–B224. https://doi.org/10.1137/130910415

Lumley, J. L. (1967). The structure of inhomogeneous turbulence. *Atmospheric turbulence and radio propagation*, 166–178.

Lyard, F. H., Allain, D. J., Cancet, M., Carrère, L., & Picot, N. (2021). Fes2014 global ocean tide atlas: Design and performance. *Ocean Science*, *17*(3), 615–649. https://doi.org/10.5194/os-17-615-2021

Mahfouf, J.-F., & Rabier, F. (2000). The ecmwf operational implementation of four- dimensional variational assimilation. ii: Experimental results with improved physics. *Quarterly Journal of the Royal Meteorological Society*, *126*(564), 1171–1190. https://doi.org/https://doi.org/10.1002/qj.49712656416

Monahan, A. H., Fyfe, J. C., Ambaum, M. H. P., Stephenson, D. B., & North, G. R. (2009). Empirical orthogonal functions: The medium is the message. *Journal of Climate*, *22*(24), 6501–6514. https://doi.org/10.1175/2009JCLI3062.1

Openda user documentation. (2016). Daltares.

Ralston, M. L., & Jennrich, R. I. (1978). Dud, A Derivative-Free Algorithm for Nonlinear Least Squares. *Technometrics*, *20*(1), 7–14. https://doi.org/10.1080/00401706.1978.10489610

Stammer, D., Ray, R. D., Andersen, O. B., Arbic, B. K., Bosch, W., Carrère, L., Cheng, Y., Chinn, D. S., Dushaw, B. D., Egbert, G. D., Erofeeva, S. Y., Fok, H. S., Green, J. A. M., Griffiths, S., King, M. A., Lapin, V., Lemoine, F. G., Luthcke, S. B., Lyard,

F., … Yi, Y. (2014). Accuracy assessment of global barotropic ocean tide models. *Reviews of Geophysics*, *52*(3), 243–282. https://doi.org/10.1002/2014RG000450

Trémolet, Y. (2007). Incremental 4d-var convergence study. *Tellus A*, *59*(5), 706–718. https://doi.org/10.1111/j.1600-0870.2007.00271.x

Wang, X., Verlaan, M., Apecechea, M. I., & Lin, H. X. (2021). Computation-efficient parameter estimation for a high-resolution global tide and surge model. *Journal of Geophysical Research: Oceans*, *126*(3), e2020JC016917. https://doi.org/https://doi.org/10.1029/2020JC016917

Chapter 5

Parameter Estimation to Improve Coastal Accuracy

Global tide and surge models play a major role in forecasting coastal flooding due to extreme events or climate change. Model performance is strongly affected by parameters such as bathymetry and bottom friction. In this study, we propose to implement an estimation of bathymetry globally and the bottom friction coefficient in the shallow waters where energy dissipation is largest for a Global Tide and Surge Model (GTSMv4.1). However, the estimation effect is limited by the scarcity of observations. We propose to combine the FES2014 dataset (gridded distributed globally) with tide gauge data (distributed unevenly along the coasts) to offset the impact of scarce observations. The FES2014 dataset outperforms GTSM in most areas and is used as observations for the deep ocean and some coastal areas, such as Hudson bay/Labrador, where tide gauges are scarce but energy dissipation is large. The experiment is performed with a computation and memory efficient iterative parameter estimation scheme for a Global Tide and Surge Model (GTSMv4.1). Estimation results show that model performance is significantly improved for deep ocean and shallow waters, especially in the European Shelf using the CMEMS tide gauge data in the estimation. GTSM is also validated by comparing to FES2014 dataset and tide gauges from UHSLC, CMEMS dataset and some Arctic stations in the year 2014.

Parts of this chapter have been included in a manuscript submitted for publication to Ocean Science:

Wang, X., Verlaan, M., Veenstra, J, and Lin, H. X. Parameter Estimation to Improve Coastal Accuracy in a Global Tide Model.

5.1 Introduction

Data assimilation or parameter estimation technique optimizes parameters by minimizing the difference between model runs and observations (Heemink et al., 2002; Mayo et al., 2014; Zijl et al., 2013). Stammer et al. (2014) reported that assimilated tide models have higher accuracy than non-assimilative models. For example, in chapters 3 and 4 we developed an efficient iterative parameter estimation scheme to estimate bathymetry globally for a high-resolution GTSMv3.0 and significantly improved model performance in the deep ocean but only improved slightly in the shallow water. To further improve the model accuracy near the coast, we propose to combine the estimation of bathymetry and bottom friction coefficient together with more tide gauge data included in this study. Bottom friction plays an essential role at the coasts accounting for a significant proportion of tide energy dissipation (Egbert & Ray, 2001). The total amount of global tidal energy dissipation is approximate 3.7TW, and two-thirds is generated by the bed stress. The bottom friction term in the quadratic bed stress formula with the coefficient defined by the of Chézy, Manning or White-Colebrook method (Colebrook et al., 1937; Manning et al., 1890), and the coefficient is empirically defined. Some model tests are performed to adjust the coefficient by calculating the difference between model and measurements. This value is difficult to set accurately but strongly related to the water level representation in the shallow water. Moreover, the bottom friction coefficient can vary strongly between regions.

In regional tide models, data assimilation is applied predominantly to estimate bottom friction bathymetry, and boundary variables (Edwards et al., 2015; Navon, 1998) with ensemble (Siripatana et al., 2018; Slivinski et al., 2017) or adjoint methods (Zhang et al., 2020). Ullman and Wilson (1998) estimated a drag coefficient by assimilating Acoustic Doppler Current Profiler (ADCP) data into a tidal model of the lower Hudson estuary with the adjoint method. Zijl et al. (2013) improved the water level forecasts for the Northwest European Shelf and the North Sea through directly modeling and assimilating altimeter and tide gauge data to adjust bathymetry and Manning's roughness coefficient. Mayo et al. (2014) estimated a spatially varying Manning coefficient of an Advanced Circulation (ADCIRC) model of Galveston Bay with a square root ensemble Kalman filter. The estimation of bottom friction using data-assimilation has been applied successfully to the European Continental Shelf (Heemink et al., 2002), Bohai, Yellow, and East China Seas (Wang et al., 2021). We found only one application at a global scale (Lyard et al., 2021), where altimetry derived tides and tides derived from tide gauges are assimilated into a combination of a time-stepping and a spectral tide model. The uncertainty for the model, is partly based on parameter uncertainty, such as bed friction, but the result is in the form of a tide dataset, called FES2014 as we discussed in Chapter 1. The application focuses on tides only. We follow a different approach using time series as the basis for the cost function and also study the sensitivity of parameters and observations.

There are considerable differences between data-assimilation for tides in deep water and near the coast. In the deep ocean, bathymetry is reported as the parameter that has most influence on the tide representation. The sensitivity to bottom friction is very small in deep water, but is often the most sensitive parameter in shallow water. The main reason for this is that the effects of both parameters interact.

In this study, we combined the estimation of bathymetry and bottom friction together. Bathymetry directly controls the tide propagation speed, which is proportional to the square root of the local water depth (Pugh & Woodworth, 2014). On the other hand, bottom friction controls the dissipation of tide energy (Egbert & Ray, 2001). But bottom friction also decreases with depth, which results in a non-linear interaction. Moreover, due to the quadratic velocity in the friction term, the effect of friction is enhanced when the different tidal constituents propagate along the shallow water with the complex topography (Cai et al., 2018). Thus, water level is influenced by the co-action of bathymetry and bottom friction. This also creates an interaction between the deep ocean and the shelf. The bathymetry in the deep ocean not only affects the tidal propagation there but also in adjacent coasts. And though the dissipation by bottom friction predominantly occurs in shallow water, this will also change the tides in the adjacent deep ocean. To our knowledge, this is the first study with a global model that combined the estimation of bathymetry and bottom friction. With this approach, we aim to improve modeled tides, both in the deep ocean as well as along the coasts.

We use the computation and memory efficient parameter estimation schemes proposed in Chapter 4. Bathymetry is estimated in all ocean basins, and regions with significant tidal energy dissipation are selected for the bottom friction coefficient estimation. The areas with most tidal energy dissipation are the European Shelf and Hudson Bay region (Egbert & Ray, 2001). FES2014 time-series are used as observations for the deep ocean. This dataset has higher accuracy for tides than our initial model (Stammer et al., 2014) and with FES2014 tide time-series are generated easily for arbitrary locations and periods. In the coastal areas, tide gauge data is included in the estimation and validation processes to increase coverage for the coastal regions. Tide gauge data was collected from the UHSLC (global coverage), CMEMS (Europe). For one comparison in the Arctic, we made use of the tide dataset by Kowalik and Proshutinsky (1994), the contains four major constituents for a relatively large number of Arctic tide gauges. Since tide gauge data are scarce in some areas, we investigate the use of FES2014 also in some coastal regions. The bottom friction is estimated in the Hudson Bay region, European Shelf and often other regions with large energy dissipation using a combination of FES2014 and tide gauge data as observations. Together, these datasets form a reliable joined parameter estimation application to correct the bathymetry globally and bottom friction coefficient in the coastal and shelf seas.

In Chapter 5.2 and 5.3, the Global Tide and Surge Model (GTSM) in a updated version 4.1 and multiple-parameters to estimate are introduced. Chapter 5.4 describes the detailed methods for the bottom friction coefficient subdomain generation and observation selection. Chapter 5.5 presents the parameter estimation experiment set-up and results analysis. The estimated model is evaluated with a one-year analysis comparison with the FES2014 dataset and tide gauge data in the time and frequency domains in Section 5.5. Finally, the discussion and conclusions follow in Section 5.6.

5.2 GTSMv4.1 Configure

GTSM is updated in the version 4.1. In comparison to GTSMv3.0 with the updated bathymetry (same bathymetry as GTSMv4.1) that described in Chapter 2 and used in

Chapter 3 and 4, the internal tide forcing term is corrected for the layer thickness in the salinity/temperature datasets in GTSMv4.1. GTSMv4.1 is retweaked for the bottom friction and internal tides friction drag coefficients. We use a full set of 484 tide potential frequencies in version 4.1 replacing 60 constituents in GTSMv3.0. These changes result in a more accurate initial model with the RMSE reduced by 1cm compared with the FES2014 dataset. The bias difference is corrected before the RMSE calculation in this paper. In our estimation experiments, GTSMv4.1 is simulated for tide representation only and the long-term tide constituents (SA and SSA) are excluded to avoid the seasonal changes to the time series because long-term constituents show large variation between years.

5.3 Multiple-Parameters Estimation

5.3.1 Parameters to Estimate

In Chapter 2, we tested the sensitivity of bathymetry and internal tide friction term for the deep ocean by comparing the relative changes of the cost function when perturbing a specific parameter. It shows that bathymetry perturbation results in larger changes to water level than the internal tide friction term. Therefore, we only optimized the global bathymetry for the deep ocean.

In shallow water, bottom friction is also a main energy dissipative process. Figure 5.1a illustrates the global tide energy dissipation distribution by the bottom friction term. The regions in Figure 5.1b are defined the same as in Egbert and Ray (2001). The total tide energy dissipation in the initial GTSM is 3.77TW, 2.39TW from bottom friction, and 1.37TW from the internal tide friction. The top values are for the Hudson Bay, the North West Australian Shelf and the European Shelf, as Figure 5.1b shows. We propose to estimate bottom friction only in the shallow water regions with large bottom friction energy dissipation.

It is impractical to estimate the bathymetry and the bottom friction coefficient for all the grid cells because of the limited observations and it would also result in huge computational demand, and memory requirement. To reduce the parameter dimension, we divide the global ocean into 110 subdomains for bathymetry estimation and define the correction factor for each subdomain to adjust the parameters in Chapter 3. The estimation subdomains for the bottom friction term are located in areas with high dissipation based on Figure 5.1b and sufficient coastal observations, as explained in more detail in Section 5.4.

5.3.2 Parameter Estimation Scheme

The parameter estimation application for GTSM uses the estimation scheme developed in Chapter 4, which has three methods to ensure the estimation feasible, including the computational cost reduction by coarse-to-fine strategy, the memory requirement reduction by POD based time pattern order reduction, and the contribution on estimation accuracy with implementation of outer-loop iterations. It results in a computation-efficient and low-memory usage parameter estimation scheme.

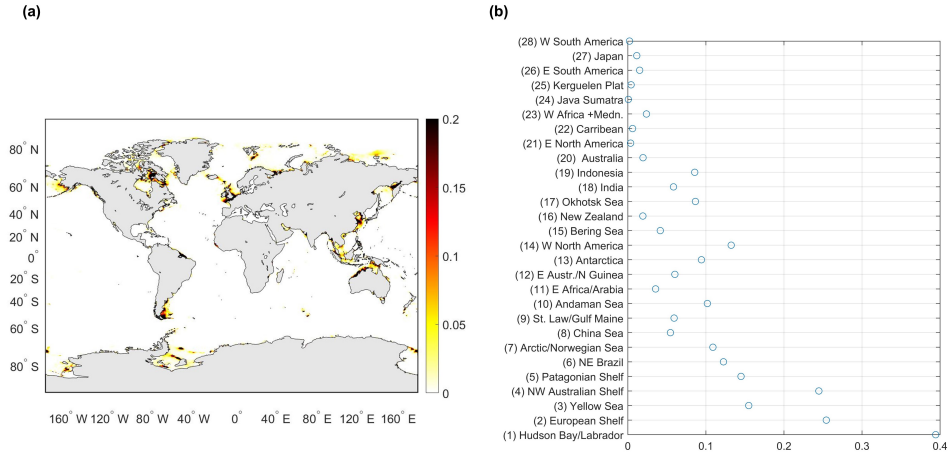

Figure 5.1: Bottom friction energy dissipation in initial GTSMv4.1 (a) Global distribution [Unit:W/m^2]; (b) Area-integrated energy dissipation [Unit:TW].

5

5.3.3 Observation

We investigated tide observations at the global scale. What we can collect and use for the calibration are the FES2014 dataset and several global or regional tide gauge datasets, as we discussed in Chapter 1.

For efficiency, we calibrated tides separately. Firstly, we generate about 4000 time series from the FES2014 dataset to ensure enough observations for estimating bathymetry in the year of 2014. These observations are evenly distributed and located in the deep ocean with a depth larger than 200m. Moreover, tide analysis is performed in the CMEMS and UHSLC dataset tide gauge data with the TIDEGUI software, a matlab implementation of approach proposed by Schureman (1958) and following by the visual inspection of tide and surge representations. After the tidal analysis and quality control, we obtained 237 locations from the UHSLC dataset and 297 locations from the CMEMS dataset.

5.4 Estimation of Bottom Friction Coefficient

Even though we obtained three collections of tide gauges, the observations are still quite sparse in some coastal seas. Therefore, we first investigate how to make use of the available data with the consideration of the model performance and parameter sensitivity.

5.4.1 Model and Observation Accuracy Analysis

FES2014 dataset is very accurate in the deep ocean (Stammer et al., 2014) while along the coast, tide gauge data can be more trustworthy. However, tide gauges data are dis-

tributed irregularly. We propose to use a combination of the FES2014 dataset and tide gauge data in the shallow water. The first step is to analyze the accuracy of the FES2014 dataset and the initial GTSMv4.1 comparing with the tide gauge data.

Tide analysis is performed with the TIDEGUI software for the water level representation from GTSM in the year 2014. Root-mean-square (RMS) describing the difference between model output and observations for tidal components is applied with the formula:

$$RMS = \sqrt{\overline{(A_m cos(\omega t - \phi_m) - A_o cos(\omega t - \phi_o)]^2}} \tag{5.1}$$

A_m and A_o are model output and observation amplitudes, ϕ_m, ϕ_o are for the phase lag. ω is the tide frequency. The overbar shows the averaging over one full cycle of the constituent (ωt varying from 0 to 2π) in all locations. We also use Root-Sum-Square (RSS) to describe the Root Square Sum of RMS for the listed major tidal constituents. To facilitate comparison, we use the same formulas for RSS and RMS as in Stammer et al. (2014).

Table 5.1 illustrated the Root-sum-square(RSS) and RMS of eight major tide components between FES2014 and initial GTSM with the tide gauge data. The RSS is calculated for all the eight components in all locations. Comparing with the UHSLC dataset at the globe, FES2014 is more accurate than GTSM for all of the eight components, implying generally FES2014 dataset can provide better tide representation in the shallow water than GTSM. This conclusion is also supported by the comparison with the stations in the arctic ocean. Figure 5.2 shows the spatial distribution of RSS for each location, which shows that with a few exceptions FES2014 is more accurate.

In the European Shelf, GTSM has the RSS of 19.15cm when comparing with CMEMS dataset, which is even smaller than the FES2014 dataset with the RSS of 20.42cm. This also can be observed from the RMS of the N2,M2,S2 and K2 constituents. However, from the spatial distribution of RSS for each stations shown in Figure 5.2c,5.2d, FES2014 outperforms most of the stations from CMEMS dataset but provides poor results in a few stations. These result in a larger RSS for FES2014 than GTSM. A possible reason is these tide components obtained from FES2014 is calculated by interpolating the gridded FES2014 dataset to the observation locations, resulting in some errors. GTSM has a higher resolution in the European Shelf, contributing to better results in those locations with complex bathymetry.

In general, FES2014 outperforms GTSMv4.1 in the shallow waters before calibration. Therefore, we will select FES2014 for calibration in the those areas where tide gauge stations are sparse. In the following, we use the FES2014 dataset in the deep ocean and CMEMS data in the shallow waters for the calibration. In addition, FES2014 is also included to support the shallow waters where without tide gauges. UHSLC and arctic stations are used for model validation.

5.4.2 Subdomains of Constant Bottom Friction Coefficient

The bottom friction coefficients in the regions with large tide energy dissipation (see Figure 5.1b) have to be estimated. We define multiple subdomains for the European

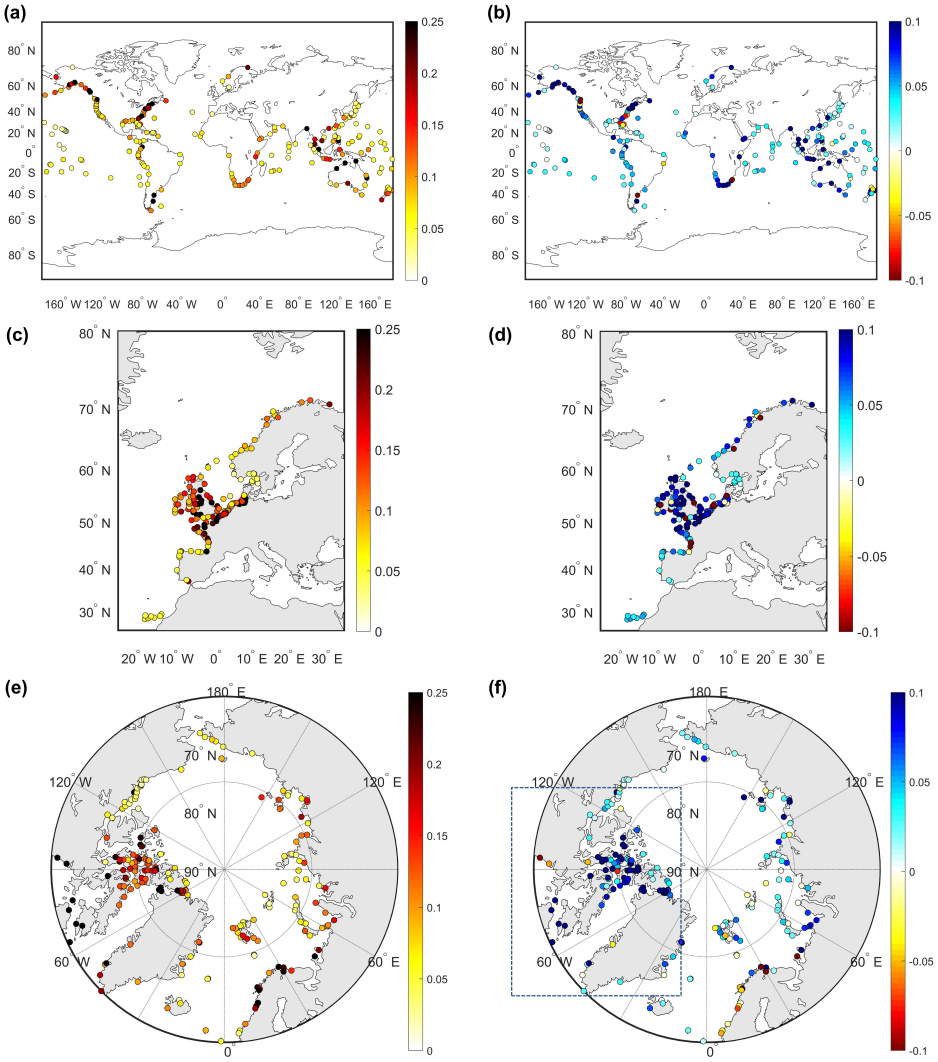

Figure 5.2: Left column: RSS between initial GTSMv4.1 and tide gauge data. Right column: RSS difference between initial GTSMv4.1 and FES2014 dataset (RSS of GTSM minus RSS of FES2014). Color blue shows better performance in FES2014 than GTSM. (a),(b) UHSLC dataset; (c),(d) CMEMS dataset; (e),(f) Arctic stations.[unit: m]

Table 5.1: RSS and RMS of eight major tide components between FES2014 dataset, initial GTSM and tide gauge data in (cm)

	RMS of all the locations								RSS
	Q1	O1	P1	K1	N2	M2	S2	K2	
UHSLC dataset									
FES2014	0.37	1.79	0.83	2.49	2.66	11.75	3.49	0.97	12.98
Initial GTSM	0.53	2.43	1.17	3.51	3.17	15.12	5.37	1.59	17.03
CMEMS dataset									
FES2014	0.45	1.05	0.62	1.14	3.96	18.55	6.99	2.28	20.42
Initial GTSM	0.68	2.17	0.68	1.55	3.22	17.99	4.66	1.70	19.15
Arctic Stations									
FES2014	-	1.26	-	2.37	-	20.24	7.67	-	21.81
Initial GTSM	-	3.03	-	5.47	-	25.27	8.63	-	27.42

Shelf and Hudson Bay/Labrador regions and single subdomains for other coastal areas shown in Figure 5.1b.

Case Region 1: Hudson Bay/Labrador Region

The Hudson Bay/Labrador region, in the top one of the list 5.1b, generates about 0.39TW energy dissipation, about 16% of the global sum. Most of the dissipation is concentrated in the Canadian archipelago, Hudson Bay, Foxe Basin, Hudson Strait, and Ungava Bat in Figure 5.3a. We defined three subdomains that firstly separate the Canadian archipelago outside the other areas. Secondly, Foxe Basin, Hudson Strait, and Ungava Bay are combined as one subdomain. The last subdomain is for Hudson Bay. Subdomains are shown in the red boxes of Figure 5.3.

The available observations are from the arctic stations but only include four major tidal components. In theory, harmonic tide analysis can be performed for the model output and it is possible to estimate parameters with the model output in the form of tide components, but accurate tide analysis needs a time series of a year, which would increase the computation time needed for estimation by more than 10 times. In Chapter 4, we showed that an accurate estimation can be performed with a full time series of 1 month, so this would increase run times by a factor of 12. This is not feasible for us at the moment. Therefore, we select to use the model output of time series, and these arctic stations can be utilized for the model validation.

To obtain sufficient observations, we propose to generate more observations from the FES2014 dataset because FES2014 dataset outperforms GTSM. Figure 5.2e illustrates the RSS (Root Sum Square) of four major tidal constituents between tide gauge data in the Arctic Ocean and the FES2014 dataset. The RSS difference between GTSM and FES2014 dataset (RSS between GTSM and tide gauge data - RSS between FES2014 and tide gauge data) varies for each location and FES2014 has smaller RSS than GTSM in most of the locations, especially in the Canadian archipelago regions (Figure 5.2f). The RSS of four major tidal constituents for all the locations in the FES2014 dataset is 21.81cm, while it is 27.82cm for GTSM. Errors are typically larger near the coast. Performance of

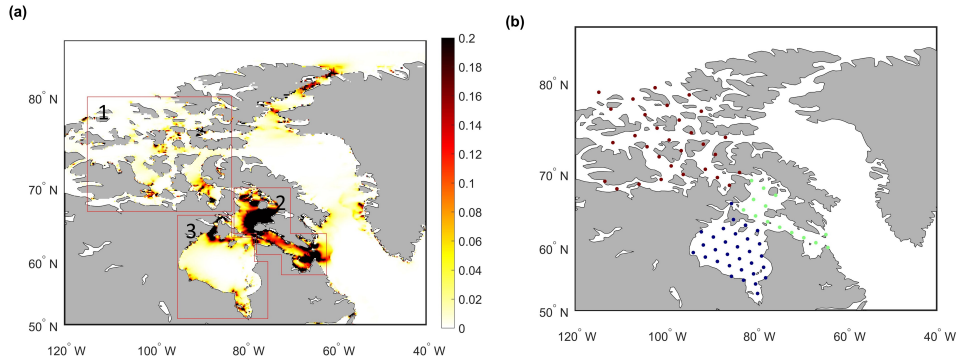

Figure 5.3: (a) Bottom friction energy dissipation per square meter of the Hudson Bay/Labrador in GTSMv4.1 [unit: W/m^2] and bottom friction coefficient subdomains (red boxes). (b) FES2014 observation distribution: Points with different colors means in different subdomain.

FES2014 at the arctic stations is better than GTSM before the calibration. We expect the accuracy of FES in open water to be even better. Therefore, we propose to use the FES2014 dataset to as the observations in the Hudson Bay region. As a result, 61 equally distributed time series are generated as on the locations in Figure 5.3b. The tidal components from arctic stations can be used for the validation.

Case Region 2: European Shelf

Bottom friction energy dissipation in the European Shelf is about 0.25TW which is approximate 11% of the global total value shown in Figure 5.4. Considering the dissipation distribution, we define 5 subdomains to estimate the bottom friction coefficient. Firstly, we define subdomains for the areas in and outside the North Sea and separate the Western and Eastern part of the North Sea. Secondly,The region of Scotland, the Faro Islands and Shetland have mountainous ocean bathymetry, where expect to a higher bottom friction coefficient. Therefore, five subdomains are generated for the European Shelf for calibration.

The estimation for European Shelf takes advantage of a large amount of local tide gauge data (Figure 5.4b). About 297 tide gauge stations from CMEMS dataset are available for the year 2014, which will directly be used for parameter estimation. 132 tide gauge data stations in the Mediterranean Sea and Baltic Sea (blue points in Figure 5.4b) are removed because they are only weakly connected to the open ocean. The remaining stations are divided into two subsets, 70 locations for calibration (red points in Figure 5.4b) and 95 points for validation (green points in Figure 5.4b).

Other Coastal Areas with Large Energy Dissipation

There are many other coastal regions that have a significant share of the total large tide energy dissipation (Figure 5.1b), like the North West of the Australian Shelf and the Yellow Sea. Therefore, 11 additional subdomains were defined globally. They are in

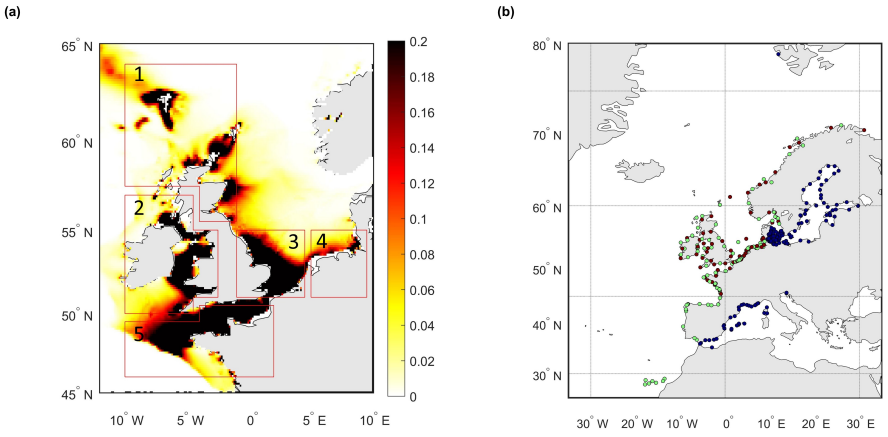

Figure 5.4: (a) Bottom friction energy dissipation per square meter across the European Shelf in GTSMv4.1 [unit: W/m^2] and bottom friction coefficient subdomains (red boxes). (b) CMEMS observation distribution: points in red are data used for calibration, points in green are used for validation and points in blue not used.

the North West Australian Shelf, Yellow Sea, Patagonian Shelf, Okhotsk Sea, North East of Brazil, Arctic/Norwegian Sea, Antarctica, Andaman Sea, China Sea, Bering Sea, and Indonesia. Because of the limited tide gauge availability in the shallow water and limited computational resources, it is not feasible to do a detailed subdomain analysis for each of these regions. The detailed subdomain distribution is shown in the Section 5.5.

Time-series from the UHSLC dataset are collected at the global scale, but these measurements are not evenly distributed and lacks data in some areas, such as the North West of Brazil and the Okhotsk Sea. To make the research on these areas feasible, we propose to use more FES2014 data in these regions for estimation and use the UHSLC dataset for validation only. Therefore, additional distance-equal distributed time series were generated from FES2014 in the location with bathymetry between 50 to 200m.

In summary, we defined 110 subdomains for bathymetry and 19 subdomains for bottom friction coefficient estimation (five in the European Shelf, three in the Hudson Bay/Labrador region and 11 for other coastal areas). In total, 4061 time series from the FES2014 dataset and 70 time series from the CMEMS dataset are included in the estimation procedure. GTSM after the estimation will be validated by comparing with time-series from the FES2014 dataset in the deep ocean and tide gauge data from the CMEMS, UHSLC and Arctic stations.

5.5 Numerical Experiment and Results

5.5.1 Parameter Estimation

Experiment Design

The experiment is set up to investigate the performance of GTSM after the estimation of bathymetry and bottom friction. GTSM is simulated with tide only because no surge data is available in the deep ocean. In addition, the surge is not sensitive to the bathymetry (see Chapter 3) and it has to be adjusted with the additional meteorological conditions. The improvement of tide representation in this study can also benefit the accuracy of the total water level. For the estimation runs, we selected a period of one month, September 2014, which we believe is sufficient for tide calibration when using high-frequency time series with 10 minutes sampling. To make this possible, meteorological and long-period signals have to be removed as much as possible. We made model runs without atmospheric forcing and removed the SA and SSA tidal potential. These constituents were also removed from the FES2014 and tide gauge tide series to keep the comparison consistent.

The time step for the model output and observation is 10 minutes, leading to the time number in a one-month simulation equal to $N_t = 4321$. The number of observation locations from FES2014 and CMEMS together is $N_s = 4131$. Moreover, parameters are corrected for the 110 bathymetry subdomains and 19 bottom friction subdomains. In this case, the data size refers to observation, and model output for all the ensembles (perturbed parameters) in the estimated process is about 17.3GB. With the implementation of POD-based time pattern order reduction, a truncation size of 200 represents the model output and observation in a smaller subspace of time patterns. The memory requirement is reduced by a factor of 22 after the POD application.

We defined several constraints in the optimization process to ensure that the adjusted parameters are realistic. The uncertainty for bathymetry correction factor is set to 5 % and for bottom friction coefficient to 20 %. Initially, each parameter is perturbed one by one with the uncertainty value. The same values are also used for a weak constraint adding to the cost function as the background term. It defines the difference between the initial and adjusted parameters. The background term can avoid changes to the parameter far away from the initial values than only achieve an insignificant improvement. In addition, hard constraints are also defined as the upper and lower boundary for the parameters. They are twice the uncertainty with the value of [-10%, 10%] to bathymetry and [-40%, 40%] to the bottom friction coefficient. Finally, there is a transition zone between each subdomain to avoid a sudden change in the correction factor from one subdomain to another. The correction factor in the transition zone is generated by automatic linear interpolation.

Parameter Estimation Results

The subdomains for bathymetry and bottom friction and their sensitivity are illustrated in Figure 5.5. Bathymetry and bottom friction have comparable sensitivities. The sensitivity values of bathymetry vary between -0.06 to 0.02 (Figure 5.5a). The sensitiv-

ity of the bottom friction coefficient changes between -0.01 to 0.05 (Figure 5.5b), with the largest value up to approximate 0.05 in the North West of the Australian Shelf. As we discussed in the Introduction, bottom friction impacts the model performance not only in the local shallow waters but also in the nearby deep ocean. It can be observed in the Figure 5.5c-5.5f when perturbing the bottom friction in the subdomains of European Shelf and Hudson bay. RMSE is large in the nearby oceans around the perturbing subdomain and smaller when the location is far away, and the largest RMSE values are located around the Coastline (Figure 5.5d). Bottom friction in Hudson bay subdomain has a larger effect on the surrounding deep oceans (Figure 5.5c) than the European Shelf (Figure 5.5e). It is consistent with that the largest tide energy dissipation is in Hudson Bay.

Figure 5.6a illustrates the cost function changes for each iteration in these four outer loops. The first 130 iterations in each loop perturb parameter one by one; parameters are iteratively updated after that until reaching the stop criteria. Optimized parameters in this outer loop will be used as the initial parameters to start the next loop. The estimation experiment was performed with 200 cores, 9 cluster nodes, running for about 16 days, with a total cost of approximately 76800 CPU core hours.

The cost function in the experiment started from the value of 1.96×10^7. It is sharply reduced in the first outer loop to the value of 6.40×10^6, resulting in a reduction of 67.3%. The decrease of the cost function in the second to fourth outer loop is slight and converged in the fourth loop with the value of 5.58×10^6. Finally, the cost function is reduced to 28.5% of the original. The relative changes of bathymetry and bottom friction coefficient is shown in Figure 5.6b, 5.6c. After the estimation, the total tide energy dissipation is reasonable with a value of 3.77TW.

The average spatial RMSE between model output and observation in September 2014 is summarised in Table 5.2. Compared with the FES2014 dataset, the spatial average RMSE is sharply reduced to 48% after the estimation, from 5.19cm to 2.47cm. The total reduction is significant in the first outer loop and slight in the second to fourth outer loops. It is observed that in the Arctic Ocean, the initial RMSE with the value of 11.03cm is larger than other regions. It is expected because we added more observation points in the Hudson Bay/Labrador. This area is more shallow with large tide amplitudes, resulting in larger RMSE than other regions. Therefore, the comparison here includes the observations located in the deep ocean and shallow water together.

The outer loop iterations provide more improvement in the Arctic Ocean than in other regions. A possible explanation is that parameter estimation impacts areas with large disagreement against observations most because they still have room to improve, and non-linear effects become more likely. Compared with the CMEMS tide gauge data in Europe, GTSM shows significant improvement in the calibration and validation processes, reduced to 64% and 69%, respectively. The difference between model and UHSLC data is significantly reduced in the first outer loop and finally decreased to 76%. This decline is smaller than that in CMEMS data for two reasons. One is we do not include the UHSLC data in the estimation process. Secondly, bottom friction coefficients are only estimated in the 19 subdomains with large tide energy dissipation, but some UHSLC tide gauges are located outside the subdomains. For example, only two tide gauges are available in the Arctic Ocean, and no stations are in the Hudson Bay area.

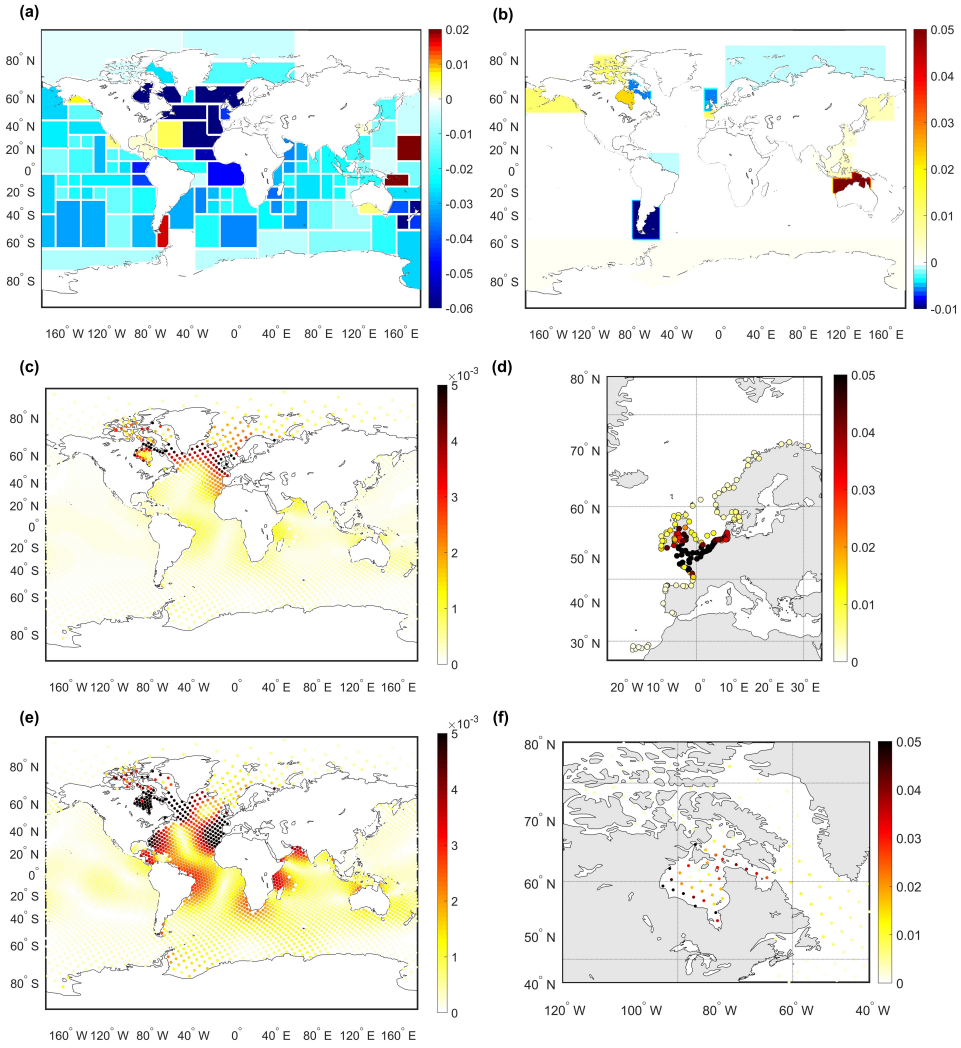

Figure 5.5: (a) Sensitivity for bathymetry. Sensitivity is the relative changes of the cost function, describing the difference between the model output and the observations when perturbing each parameter; (b) Sensitivity for bottom friction coefficient; (c-f) RMSE between initial model output and model output with perturbed bottom friction coefficient [unit: m]. (c)(d) illustrate the RMSE with the perturbation of the subdomain 5 of the European Shelf in Figure 4a; (e)(f) show the perturbation of the subdomain 3 of Hudson Bay in Figure 3a. (c)(e) show the 4061 evenly distributed locations, which are the same locations as the FES2014 dataset used in the parameter estimation. (d) shows the RMSE in the tide gauge locations around the EU. (f) shows the observation points from FES2014 dataset in detail in the Hudson Bay.

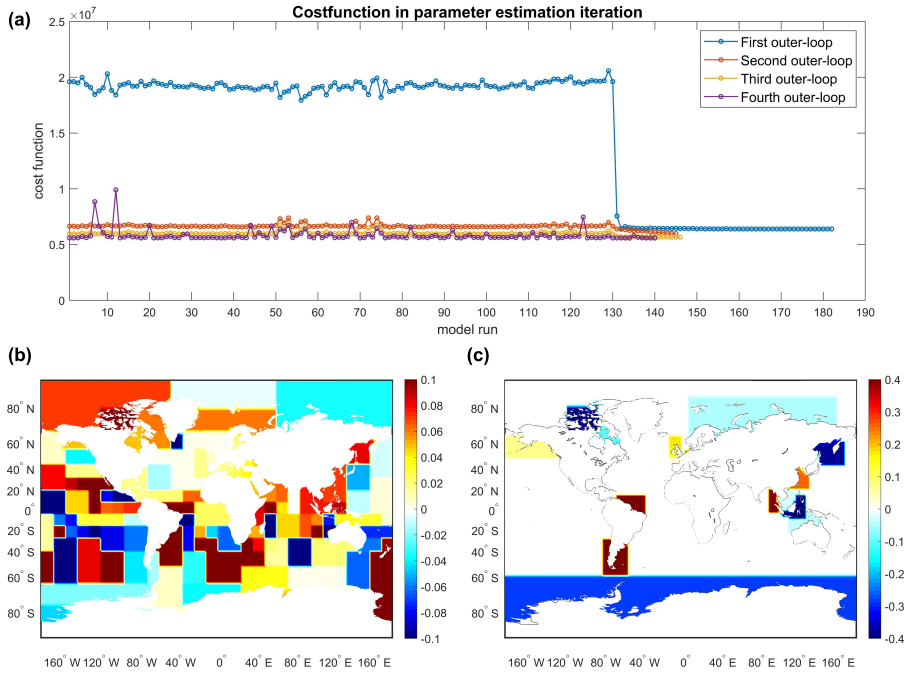

Figure 5.6: (a) Value of the cost function for each model run during the estimation; (b) Relative changes of bathymetry (bathymetry correction factor) after the estimation; (c) Relative changes of bottom friction coefficient (bottom friction coefficient correction factor) after estimation.

The spatial distribution of RMSE for estimated GTSM and the RMSE difference between the initial and estimated model in September 2014 is shown in Figure 5.7. RMSE between estimated model and FES2014 dataset is larger in the shallow water, such as the North West of the Australian Shelf, Hudson Bay/Labrador, than in the deep ocean (Figure 5.7a). It can be observed that the estimated model is significantly improved with the RMSE reduced by about 2cm for most of the regions in the deep ocean (Figure 5.7b).Using more time series from the FES2014 dataset in the Hudson Bay/Labrador plays a role in the estimation process since the model after estimation is better agreed with the FES2014 dataset for most observation points except several locations in the in the middle area of Hudson Bay. The comparison with Arctic stations in the Hudson Bay region will be illustrated in Section 5.5.2.

Compared with the CMEMS dataset in Figure 5.7g and 5.7h, the parameter estimation brings a large improvement to the European Shelf, with the RMSE reduced from 17.60 cm to 11.25cm. This demonstrates that the direct use of tide gauge data in the estimation can improve model performance in shallow waters. Figure 5.7c and 5.7d also illustrates that RMSE between the model and the UHSLC dataset is decreased by a small amount from 11.98cm to 9.07cm. Figure 5.7e and 5.7f reports the comparison with the

Table 5.2: Average RMSE between GTSM and observations in the period of September, 2014 [unit: cm]

Data		Size	Initial	Es_1[a]	Es_2	Es_3	Es_4
FES2014	Arctic Ocean	196	11.03	6.85	6.09	5.61	5.61
	Indian Ocean	784	5.31	2.45	2.38	2.39	2.38
	North Atlantic	437	4.89	2.46	2.40	2.34	2.38
	South Atlantic	472	3.75	2.49	2.33	2.17	2.16
	North Pacific	923	5.05	2.74	2.61	2.55	2.53
	South Pacific	1008	4.96	2.18	2.06	2.01	2.01
	Southern Ocean	241	4.96	3.05	2.87	2.72	2.65
	Total	4061	5.19	2.70	2.56	2.48	2.47
CMEMS for calibration		70	17.60	12.77	12.15	11.36	11.25
CMEMS for validation		90	16.06	12.47	11.89	11.21	11.15
UHSLC dataset	Arctic Ocean	2	13.18	9.19	8.34	6.92	6.63
	Indian Ocean	37	13.94	10.56	10.45	10.54	10.53
	North Atlantic	52	13.96	11.71	11.64	11.76	11.68
	South Atlantic	15	12.22	9.00	8.73	8.62	8.67
	North Pacific	85	10.52	8.42	8.33	8.27	8.22
	South Pacific	43	8.67	5.80	5.67	5.62	5.62
	Southern Ocean	-	-	-	-	-	-
	total	234	11.98	9.16	9.07	9.10	9.07

[a] Es_1, Es_2, Es_3, Es_4 means estimated GTSM in the $1^{st}, 2^{nd}, 3^{rd}, 4^{th}$ outer loop.

UHSLC dataset for the Australian shelf, where we defined several subdomains for bottom friction estimation. Even though the subdomains here are not as detailed as in the Hudson Bay and the European Shelf, the RMSE is also greatly reduced after the calibration in most of the tide gauges.

In general, GTSM after the parameter estimation shows significant improvement in September 2014. The estimation of bottom friction gives much larger improvements than for estimation of bathymetry only. GTSM benefits from estimating the bottom friction coefficient, especially in the Hudson Bay/Labrador and the European Shelf. The combination use of FES2014 and tide gauge data for the bottom friction coefficient optimization offsets the scarce supplies of observations in the shallow water and improve model skills after the parameter estimation. The direct use of tide gauge data provides excellent agreements between the observation and model output after the estimation. And the including of FES2014 dataset in shallow waters (50-200m) can partly make up for the lack of tide gauges.

5.5.2 Model Validation in the Year of 2014

In this section, we validate the GTSM with the FES2014 dataset and tide gauge data for the whole year of 2014, both in the time and frequency fields.

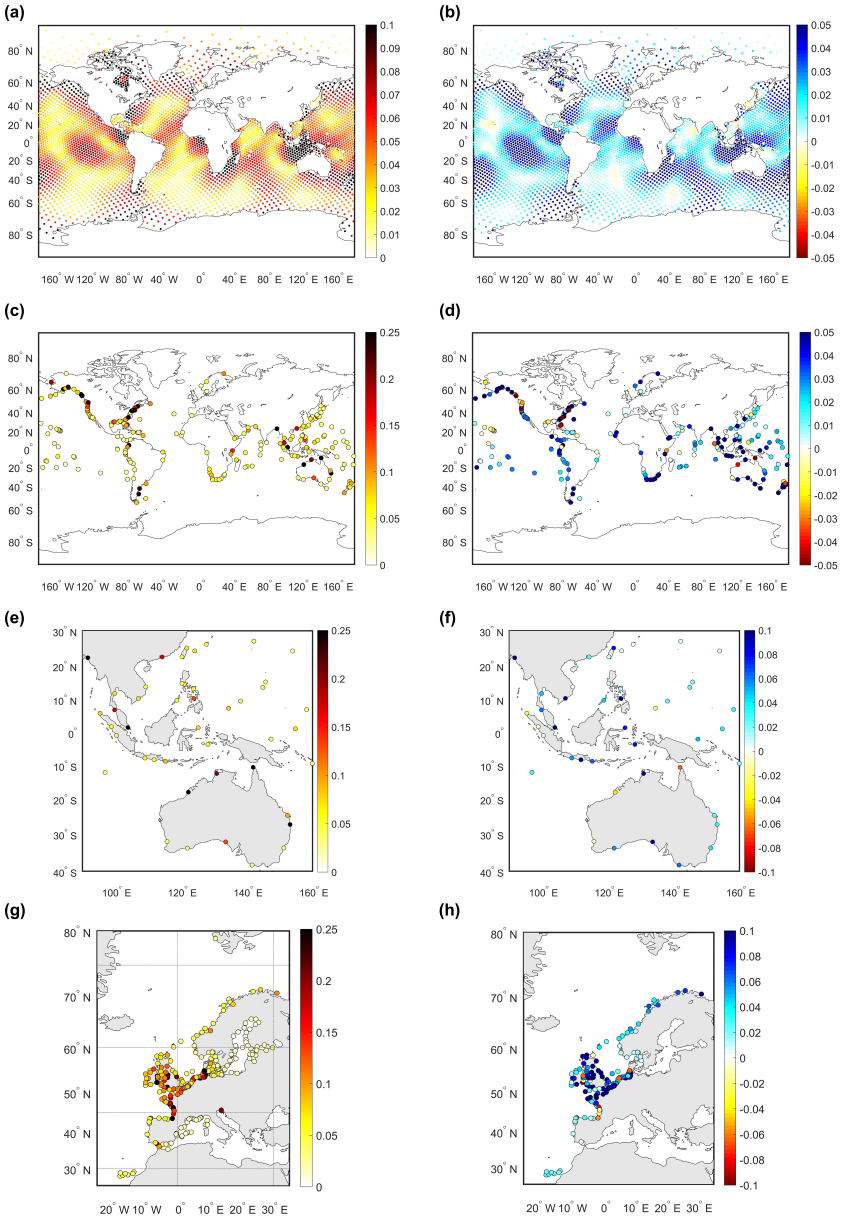

Figure 5.7: Left column: spatial distribution of RMSE of estimated GTSM. Right column: The RMSE difference between initial model and estimated model from September 1 to 30 2014. RMSE difference is defined as the RMSE of initial model minus RMSE of estimated GTSMv4.1. Color blue in Right column shows improvements in the estimated model [unit: m]. Observation dataset used to compare with GTSMv4.1:(a) (b) FES2014 dataset; (c)(d) UHSLC dataset; (e)(f) UHSLC dataset around the Australian Shelf; (g)(h) CMEMS dataset.

Monthly Time-series Comparison

First, we evaluate GTSM by comparing the tide representation of the year 2014 with observations (FES2014 and tide gauge data) in the deep ocean and shallow waters. Figure 5.8 shows the average RMSE between the GTSM and FES2014 time-series for each month of year 2014 in seven ocean regions (5.8a-5.8g). Most of the observations are located in the deep ocean. Compared to the initial GTSM, results in the calibration period and the other month of 2014 have reached similar accuracy, implying that the estimation is not over-fitting the observations we used. RMSE in the Arctic Ocean is larger than other regions, which coincides with the results in Table 5.2.

Model performance in the shallow water is compared with the CMEMS and UHSLC tide gauge data in Figure 5.9. CMEMS data in Figure 5.9a includes all the stations for calibration and validation. The average spatial RMSE for the year 2014 in the initial model is 16.7cm. After the first outer loop estimation, a large reduction is achieved to a value of 12.38cm. Accuracy is further improved due to the outer loop iteration. Finally, the RMSE is reduced to 66.5%. The direct use of CMEMS tide gauge data for calibration of bottom friction coefficient effectively reduces the model error that came from parameter uncertainty and results in high accuracy tide representation in the shallow waters.

In this study, UHSLC tide gauge dataset is only used for validation (Figure 5.9b). Most improvements are achieved in the first outer loop and small changes in later outer loop iterations. It shows that the calibration also has better agreements in shallow waters outside Europe. But because many of the stations are not in the estimation subdomains we defined, the improvement is limited.

Comparison of Tidal Constituents

To further analyze the model performance of GTSM before and after the estimation, we perform a harmonic analysis for the year of 2014.

Table 5.3 compares the tidal analysis results of GTSM and FES2014 before and after the estimation. Estimated GTSM has higher accuracy for all eight major tide components, with the RSS reduced to 52.3% of the original. The largest RMS is in the M2 tidal constituent. RMS of tidal constituents M2, S2, K1, and O1 in the Arctic Ocean are greatly larger than other regions before and after the estimation. This can also be observed from the spatial distribution of the amplitude and phase of the M2 tide component in Figure 5.10. We observed large tide amplitudes in the shallow waters, such as in the Hudson Bay, European Shelf, and the Australian Shelf, and small in the deep ocean (Figure 5.10a). It results in large amplitude differences between the GTSM and observations in the Hudson Bay/Labrador regions (Figure 5.10b), as well as the higher RMSE for the Arctic Ocean. After the estimation, amplitude and phase differences are reduced in most regions (Figure 5.10c, 5.10f). The largest amplitude differences in Figure 5.10c are still in the areas around the Hudson Bay, Foxe Basin, Hudson Strait, and Ungava Bay, even though the difference is significantly reduced compared with the initial model.

We compared the tide components with the Deep-Ocean Bottom Pressure Recorder (BPR) data in the deep ocean to assess the model performance with other tide models described by Stammer et al. (2014). BPR data is available from the Supplement of Ray (2013). Compared with the non-assimilative tide models, Initial GTSM has the RMS of

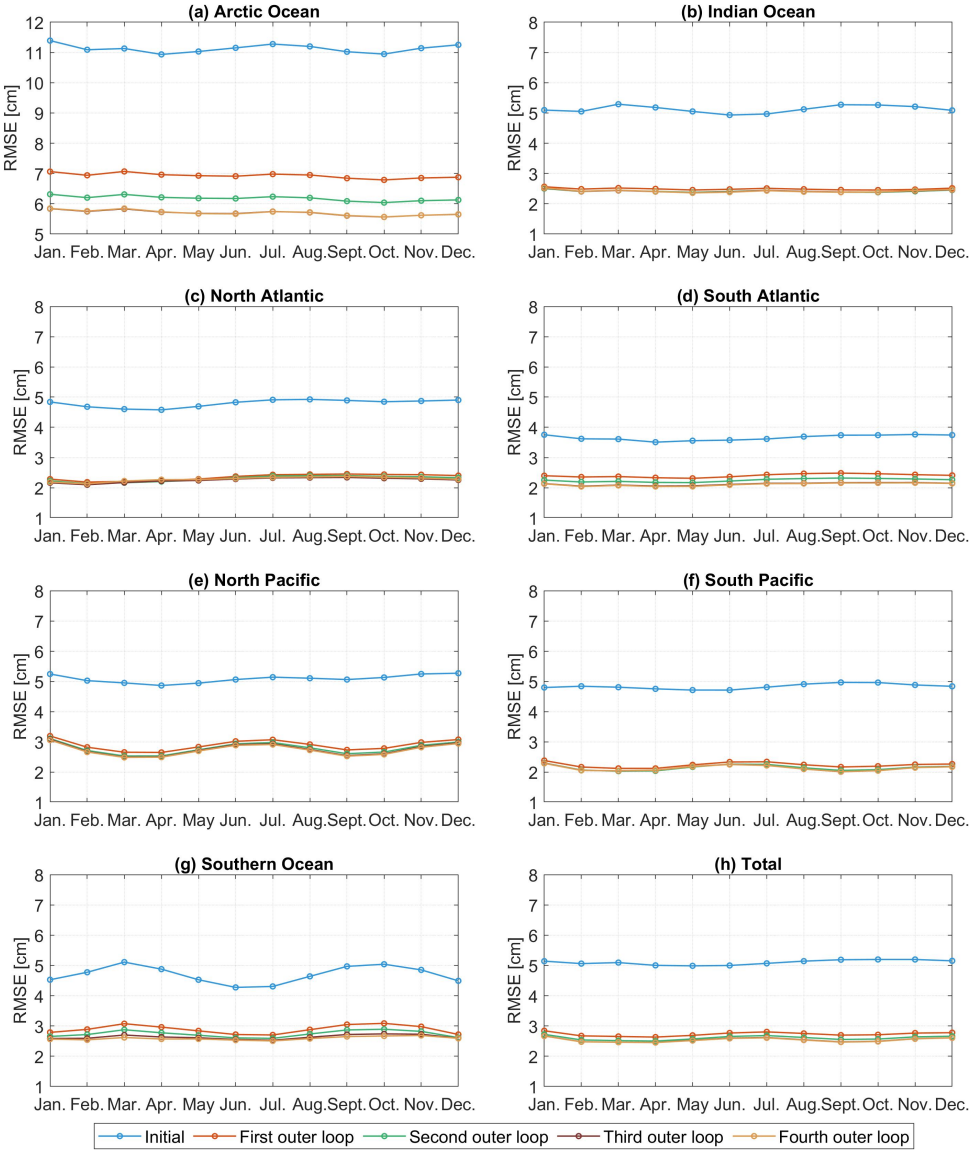

Figure 5.8: Regional RMSE between GTSM with the fine grid and FES2014 dataset in 2014

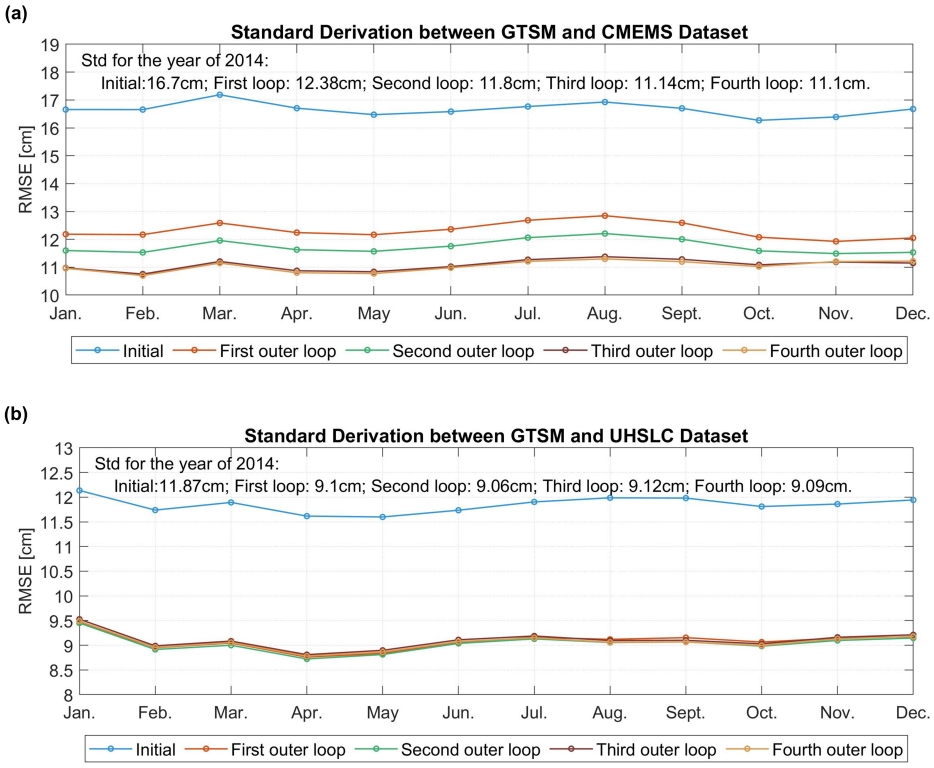

Figure 5.9: Spatial average RMSE between GTSM with the fine grid and tide gauges in 2014; (a) CMEMS dataset; (b) UHSLC dataset.

Table 5.3: RSS and RMS of eight major tide components between GTSM and FES2014 dataset in (cm). The first and second row of each region are the results before and after estimation.

	RMS of all the locations								RSS
	Q1	O1	P1	K1	N2	M2	S2	K2	
Arctic Ocean	0.34	2.88	1.54	5.00	2.78	15.37	4.29	1.50	17.33
	0.27	1.46	0.72	2.40	1.69	8.18	2.67	0.76	9.27
Indian Ocean	0.24	0.88	0.62	1.02	1.16	5.14	2.32	0.86	6.01
	0.17	0.65	0.54	0.89	0.42	1.76	1.62	0.31	2.75
North Atlantic	0.25	0.97	0.40	1.14	0.81	4.92	1.45	0.28	5.44
	0.17	0.40	0.25	0.77	0.39	2.56	1.39	0.21	3.08
South Atlantic	0.26	0.84	0.42	1.01	0.84	3.71	1.72	0.52	4.44
	0.20	0.42	0.22	0.67	0.51	1.66	1.06	0.28	2.22
North Pacific	0.36	1.96	1.00	2.94	0.95	4.66	2.18	0.50	6.42
	0.29	1.21	0.76	2.12	0.52	1.79	1.34	0.28	3.46
South Pacific	0.29	1.16	0.50	1.27	0.96	4.22	2.44	0.57	5.32
	0.29	1.06	0.46	1.21	0.58	1.71	1.05	0.27	2.70
Southern Ocean	0.27	1.09	0.55	1.54	1.28	3.01	3.40	1.17	5.25
	0.24	0.99	0.48	1.44	0.95	1.88	1.13	0.61	3.07
Total	0.29	1.42	0.73	2.04	1.15	5.53	2.39	0.72	6.71
	0.25	0.94	0.54	1.44	0.64	2.55	1.40	0.35	3.51

4.77cm in the M2 component that outperforms the purely hydrodynamic tide models described in Table 12 of Stammer et al. (2014). In the estimation process, we select the FES2014 dataset as observations for the deep ocean with a smaller RSS than the initial GTSM. After the estimation, the RSS of GTSM is reduced to 2.83cm. Even though it is still not as accurate as FES2014 or other assimilative tide models (Table 3 in Stammer et al. (2014)), but it is excellent compared to the non-assimilative models.

To analyze GTSM performance in shallow waters, we summarized the RMS of major tide components with the comparison of tide gauge data in Table 5.5. Tidal components from the FES2014 dataset have been evaluated in the tide gauge locations in Table 5.1. After the estimation, the RSS of GTSM is reduced by 16% of the initial GTSM, from 17.03cm to 14.36cm. However, the error is still larger than in the FES2014 dataset with the value of 12.98cm in Table 5.1. It is expected because we use the FES2014 dataset as the observation for some coastal regions, and the observation error limits the estimation accuracy to some extent.

Compared with the CMEMS dataset (all locations in the calibration and validation subsets), the RSS of all eight components is reduced from 19.15cm to 12.74cm. Moreover, after the estimation, model errors have the largest reduction in the European Shelf compared with CMEMS than other regions compared with the UHSLC dataset and arctic stations. These results also demonstrate directly assimilating tide gauge data can significantly improve the accuracy of tide representation in models.

In the Arctic Ocean, we analyze the four major tide components from arctic stations and GTSM. When comparing with the FES2014 dataset in the Arctic Ocean (Figure 5.8a),

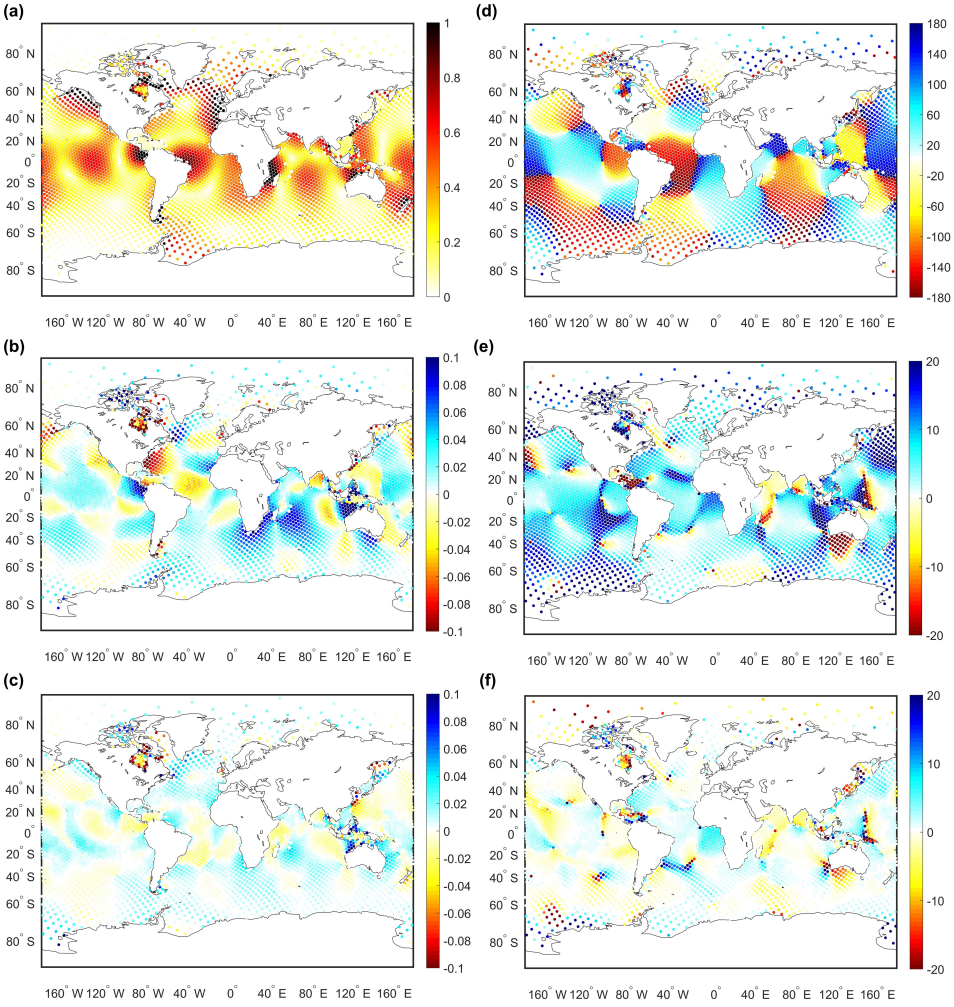

Figure 5.10: Spatial distribution of M2 amplitudes and phases from GTSMv4.1 and FES2014 dataset. (a) Amplitudes of M2 for FES2014 dataset; (b) (c): Amplitudes difference between FES2014 and initial GTSM, estimated model, respectively [unit: m]. (d) Phases of M2 for FES2014 dataset; (e) (f): Phases difference between FES2014 and initial GTSM, estimated model, respectively [unit: degree].

Table 5.4: RSS and RMS of eight major tide components between GTSM and Deep-Ocean Bottom Pressure Recorder (BPR) data[a] in (cm)

	RMS of all the locations								RSS
	Q1	O1	P1	K1	N2	M2	S2	K2	
FES2012 [b]	0.22	0.31	0.36	0.47	0.34	0.66	0.41	0.22	1.12
NSWC	0.29	0.87	0.64	1.29	1.15	4.27	1.78	0.66	5.11
FES2014	0.14	0.18	0.14	0.23	0.19	0.30	0.27	0.15	0.58
Initial	0.29	1.20	0.55	1.71	0.98	4.77	1.97	0.53	5.71
Estimated GTSM	0.25	0.68	0.41	1.41	0.54	1.79	1.33	0.24	2.83

[a] BPR data is available from the Supplement of Ray (2013).

[b] Results of NSWC and FES2012 are from Stammer et al. (2014) Table 3.

5

model error is significantly decreased in every outer-loop iteration. To assess the model performance in each iteration, we reported results with the comparison of arctic stations in four outer-loops in Table 5.5. RMS is reduced after the first outer loop, especially for the M2 component, resulting in the value of 22.24cm. It is close to the accuracy of the FES2014 shown in Table 5.1. However, the total accuracy in the second to fourth outer loop is not further improved. M2 constituent becomes a bit worse, but other tide frequencies are improved. This is contrasted with we observed from the Table 5.2 and Figure 5.8a of the comparison with FES2014 data in Arctic Ocean. In Table 5.2, the RMSE of 196 time series in the Arctic Ocean derived from the FES2014 dataset is reduced step by step with the implementation of outer-loop iterations. Model output is continuously close to the FES2014 dataset in this process, but there are no significant improvements to the Arctic stations from the outer-loop iteration. This is because, firstly, most of the arctic stations are located in the Canadian archipelago, not the Hudson Bay. In addition, there are still observation errors in FES2014 even though FES2014 provides higher accuracy than the initial GTSM. Estimation leads the results closer to the FES2014 but does not mean constantly closer to the Arctic Stations because of the observation error in FES2014 and the uncertainties with the arctic stations. The spatial distribution of RSS for each station is illustrated in Figure 5.11. We can observe that error of GTSM after estimation is smaller than before (Figure 5.11a-c). However, the estimated GTSM does not surpass the accuracy of the FES2014 dataset (Figure 5.11d), which we also did not expect. Therefore, it is concluded that the observation error significantly influences the estimation accuracy. In addition, stations in Norway seem to get worse (Figure 5.11c), which is inconsistent with CMEMS data.

In summary, model assessments from the time and frequency fields demonstrate that the parameter estimation of bathymetry and bottom friction coefficient combined with the FES2014 and tide gauge data as observation can significantly improve the tide representation in the deep ocean and shallow waters.

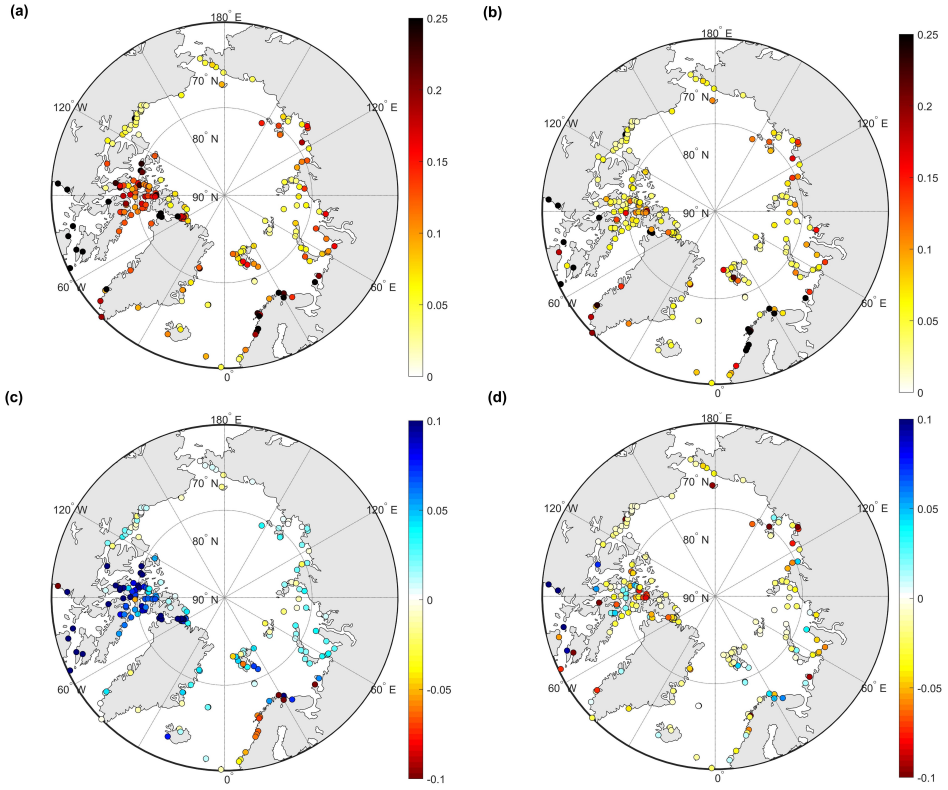

Figure 5.11: RSS of four major tide components between the Arctic station and initial GTSMv4.1 (a), estimated GTSMv4.1 (b); (c) RSS difference between initial model and estimated model (RSS of initial model minus RSS of estimated model); (d) RSS of estimated model minus RSS between FES2014 and Arctic Stations [unit: m]. (color blue shows better performance in estimated GTSM than initial model (c) or FES2014 dataset (d).

Table 5.5: RSS and RMS of eight major tide components between GTSM and CMEMS, UHSLC and Arctic Stations in (cm)

	RMS of all the locations								RSS
	Q1	O1	P1	K1	N2	M2	S2	K2	
UHSLC dataset									
Initial	0.53	2.43	1.17	3.51	3.17	15.12	5.37	1.59	17.03
Estimated GTSM[a]	0.51	2.21	1.05	3.24	2.71	12.63	4.56	1.29	14.36
CMEMS dataset									
Initial	0.68	2.17	0.68	1.55	3.22	17.99	4.66	1.70	19.15
Estimated GTSM	0.51	0.85	0.57	1.48	2.45	11.19	5.12	1.23	12.74
Arctic Stations									
Initial	-	3.03	-	5.47	-	25.27	8.63	-	27.42
Es_1[b]	-	2.22	-	3.74	-	20.39	7.73	-	22.24
Es_2	-	2.11	-	3.51	-	20.68	7.52	-	22.38
Es_3	-	1.98	-	3.24	-	20.65	7.27	-	22.22
Es_4	-	1.95	-	3.24	-	20.46	7.21	-	22.02

[a] Estimated GTSM is the estimated GTSM in the fourth outer loop.

[b] Es_1, Es_2, Es_3, Es_4 means estiamted GTSM in the 1^{st},2^{nd},3^{rd},4^{th} outer loop.

5.6 Conclusions

This study presents a study about the joint estimation of bathymetry and bottom friction coefficient, for a Global Tide and Surge Model (GTSM), which effectively improves the global tide representation, especially in shallow waters. Bathymetry is the main parameter affecting model performance at the worldwide scale, and the bottom friction term influences the tide representation in areas with significant tide energy dissipation (shallow/coastal areas). The FES2014 dataset, with higher accuracy than the initial GTSM in the deep ocean, is used for calibration in this paper. It plays a vital role in correcting the bathymetry factor in the oceans domain we defined. To ensure that the estimation for bottom friction coefficient is feasible, we propose a combination of FES2014 and tide gauge data for the estimation of bottom friction in shallower coastal waters. Applying this parameter estimation significantly improves the tide representation of GTSM almost everywhere around the globe.

The Hudson Bay/Labrador Sea and European Shelf are the regions with the largest tide energy dissipation. The bottom friction coefficient in the European Shelf is optimized with the tide gauge data from the CMEMS dataset. This results in the largest improvements of tide accuracy for shallow waters. We refined the observation locations from the FES2014 dataset in the Hudson Bay and Labrador sea. This approach is based on the condition that data of Arctic stations only have four major tide components that cannot be used for calibration, and FES2014 has higher accuracy than initial GTSM when comparing against these stations. After estimation the accuracy of GTSM is close to that of FES here. Moreover, some other coastal areas with large energy dissipation are estimated by including more observation located in the depth between 50-200m from

FES2014 dataset because the numbered UHSLC tide gauges are too few to be used for calibration directly in many regions. After calibration, GTSM has smaller disagreements than initial model but not as accurate as the FES2014 dataset when comparing with UHSLC dataset. RSS of eight tide components between FES2014 and UHSLC tide gauge data is 12.98cm, which is smaller than the estimated GTSM with the value of 14.36cm.

In summary, the accuracy of GTSM is significantly improved with the combined parameter estimation of bathymetry and bottom friction coefficient. Tide representation in shallow waters benefits from the optimization of bottom friction coefficient, contributing to a more accurate water level forecast when including wind and air pressure conditions for surge simulation. Accurate parameter estimation for global tide models needs sufficient observations and a proper determination of parameter subdomains. Direct utilization of tide gauge data provides the most significant reduction of model error. Some areas such as the Hudson Bay with insufficient tide gauge measurements, the use of other data with higher accuracy than the model can also improve the model performance to a certain extent. The one-year model validation demonstrates the estimated GTSM can provide long-term high accuracy tide forecasts. Thanks to the efforts of communities like GLOSS, UHSLC, CMEMS, EMODnet and GESLA, more and more tide gauge data is becoming available. However, the spatial scales in shallow coastal waters are much smaller than in deep water, so that the number of available tide gauge is not yet sufficient for calibration of tide models at the moment. Satellite altimetry has the potential to add much more information about tides in shallow waters. However, compound tides, overtides and tide-surge interaction will make this more complicated than in deeper waters.

Bibliography

Cai, H., Toffolon, M., Savenije, H. H. G., Yang, Q., & Garel, E. (2018). Frictional interactions between tidal constituents in tide-dominated estuaries. *Ocean Science*, *14*(4), 769–782. https://doi.org/10.5194/os-14-769-2018

Colebrook, C. F., White, C. M., & Taylor, G. I. (1937). Experiments with fluid friction in roughened pipes. *Proceedings of the Royal Society of London. Series A - Mathematical and Physical Sciences*, *161*(906), 367–381. https://doi.org/10.1098/rspa.1937.0150

Edwards, C. A., Moore, A. M., Hoteit, I., & Cornuelle, B. D. (2015). Regional ocean data assimilation [PMID: 25103331]. *Annual Review of Marine Science*, *7*(1), 21–42. https://doi.org/10.1146/annurev-marine-010814-015821

Egbert, G. D., & Ray, R. D. (2001). Estimates of m2 tidal energy dissipation from topex/ poseidon altimeter data. *Journal of Geophysical Research: Oceans*, *106*(C10), 22475–22502. https://doi.org/https://doi.org/10.1029/2000JC000699

Heemink, A., Mouthaan, E., Roest, M., Vollebregt, E., Robaczewska, K., & Verlaan, M. (2002). Inverse 3d shallow water flow modelling of the continental shelf. *Continental Shelf Research*, *22*(3), 465–484. https://doi.org/https://doi.org/10.1016/S0278-4343(01)00071-1

Kowalik, Z., & Proshutinsky, A. Y. (1994). The arctic ocean tides. *The polar oceans and their role in shaping the global environment* (pp. 137–158). American Geophysical Union (AGU). https://doi.org/https://doi.org/10.1029/GM085p0137

Lyard, F. H., Allain, D. J., Cancet, M., Carrère, L., & Picot, N. (2021). Fes2014 global ocean tide atlas: Design and performance. *Ocean Science*, *17*(3), 615–649. https://doi.org/10.5194/os-17-615-2021

Manning, R., Griffith, J. P., Pigot, T., & Vernon-Harcourt, L. F. (1890). *On the flow of water in open channels and pipes*.

Mayo, T., Butler, T., Dawson, C. N., & Hoteit, I. (2014). Data assimilation within the advanced circulation (adcirc) modeling framework for the estimation of manning's friction coefficient. *Ocean Modelling*. http://hdl.handle.net/10754/563473

Navon, I. (1998). Practical and theoretical aspects of adjoint parameter estimation and identifiability in meteorology and oceanography. *Dynamics of Atmospheres and Oceans*, *27*(1), 55–79. https://doi.org/https://doi.org/10.1016/S0377-0265(97)00032-8

Pugh, D., & Woodworth, P. (2014). *Sea-level science: Understanding tides, surges, tsunamis and mean sea-level changes*. Cambridge University Press.

Ray, R. D. (2013). Precise comparisons of bottom-pressure and altimetric ocean tides. *Journal of Geophysical Research: Oceans*, *118*(9), 4570–4584. https://doi.org/https://doi.org/10.1002/jgrc.20336

Schureman, P. (1958). Manual of harmonic analysis and prediction of tides.

Siripatana, A., Mayo, T., Knio, O., Dawson, C., Maître, O. L., & Hoteit, I. (2018). Ensemble kalman filter inference of spatially-varying manning's n coefficients in the coastal ocean. *Journal of Hydrology*, *562*, 664–684. https://doi.org/https://doi.org/10.1016/j.jhydrol.2018.05.021

Slivinski, L., Pratt, L., Rypina, I., Orescanin, M., Raubenheimer, B., MacMahan, J., & Elgar, S. (2017). Assimilating lagrangian data for parameter estimation in a multiple-inlet system. *Ocean Modelling*, *113*, 131–144. https://doi.org/https://doi.org/10.1016/j.ocemod.2017.04.001

Stammer, D., Ray, R. D., Andersen, O. B., Arbic, B. K., Bosch, W., Carrère, L., Cheng, Y., Chinn, D. S., Dushaw, B. D., Egbert, G. D., Erofeeva, S. Y., Fok, H. S., Green, J. A. M., Griffiths, S., King, M. A., Lapin, V., Lemoine, F. G., Luthcke, S. B., Lyard, F., … Yi, Y. (2014). Accuracy assessment of global barotropic ocean tide models. *Reviews of Geophysics*, *52*(3), 243–282. https://doi.org/10.1002/2014RG000450

Ullman, D. S., & Wilson, R. E. (1998). Model parameter estimation from data assimilation modeling: Temporal and spatial variability of the bottom drag coefficient. *Journal of Geophysical Research: Oceans*, *103*(C3), 5531–5549. https://doi.org/https://doi.org/10.1029/97JC03178

Wang, D., Zhang, J., & Wang, Y. P. (2021). Estimation of bottom friction coefficient in multi-constituent tidal models using the adjoint method: Temporal variations and spatial distributions [e2020JC016949 2020JC016949]. *Journal of Geophysical Research: Oceans*, *126*(5), e2020JC016949. https://doi.org/https://doi.org/10.1029/2020JC016949

Zhang, S., Liu, Z., Zhang, X., Wu, X., Han, G., Zhao, Y., Yu, X., Liu, C., Liu, Y., Wu, S., Lu, F., Li, M., & Deng, X. (2020). Coupled data assimilation and parameter estimation in coupled ocean–atmosphere models: A review. *Climate Dynamics*, *54*, 5127–5144.

Zijl, F., Verlaan, M., & Gerritsen, H. (2013). Improved water-level forecasting for the northwest european shelf and north sea through direct modelling of tide, surge and non-linear interaction. *Ocean Dynamics*, *63*(7), 823–847. https://doi.org/10.1007/s10236-013-0624-2

Chapter 6

Discussion and Conclusions

6.1 Discussion

To accurately assess the flood risks in coastal areas, we have designed and implemented the parameter estimation of bathymetry and bottom friction for the global tide and surge model (GTSM) in chapters 3, 4 and 5. We have mainly focused on the accurate estimation with computationally-efficient and low memory usage approaches and on the optimal use of sparse observations. Significant improvement of the tide accuracy is achieved globally. In Chapter 1, we have formulated several research questions, and in the following chapters we look back and summarize the contributions and the answers to these questions.

Rq 1:Which uncertain parameters and other uncertainties determine the accuracy of hydrodynamic global tide and surge models? And which measurements are needed to estimate them?

In Chapter 2, the relevant physical processes for global tide surge modelling are described. The model errors come mainly from uncertain parameters, such as bathymetry, bottom friction coefficient and the internal tide friction term. The model bathymetry is mainly based on GEBCO, which is a worldwide collection of bathymetric surveys augmented with satellite altimeters, but in large regions the bathymetry remains unsurveyed. Bottom friction and internal tide friction significantly impact where the tide energy dissipates, indirectly affecting the water level representation. The relative importance of these parameters is evaluated here using a sensitivity analysis. In the deep ocean, sensitivity analysis shows that the changes in tide caused by the perturbation of bathymetry are more significant than the internal tide friction coefficient. For shallow waters, the bottom friction coefficient becomes even more important, especially in the Hudson Bay/Labrador and European Shelf. Therefore, we focus on reducing the uncertainty of bathymetry in the deep ocean and the bottom friction coefficient in shallow waters to improve the model's forecast skills.

Parameter estimation accuracy also depends on the proper selection of observations.

A challenge for global tide model estimation is to obtain well-distributed water level measurements, that correlate well with the parameters. In the deep ocean, the FES2014 dataset is used as observations because it has higher accuracy than the initial tides from the GTSM and can be generated everywhere. To some extent, it can be viewed as a more convenient representation of tides from the satellite altimetry. In addition, we use tide gauges that are mainly located along the coast but while some coasts have many gauges, some have none at all. For example, the CMEMS dataset has a relatively dense coverage at the European Shelf. Some areas covered by the UHSLC dataset have only a limited number of gauges.

Based on the selection of parameters and measurements, we designed a two-stage parameter estimation scheme. In the first stage, we estimate the bathymetry in the deep ocean because the tide propagation scale is larger in the deep ocean than along the coast. We assume that once the large scales for the deep ocean are properly calibrated, the finer details for coastal regions can be adjusted in a second stage. The approach for the first stage is developed and applied in chapters 3 and 4, and significant improvements for the model-derived tide representation are achieved. After this, we originally planned to estimate bottom friction in coastal water using additional measurements. However, experiments showed that the effects of changes to the bottom friction and bathymetry interact more than we had anticipated. Also, bottom friction changes have a wider than local impact on the tide models, not only in the coastal zones but also in the deep oceans nearby. Therefore, we adjusted our plan and performed a combined estimation of bathymetry and bottom friction in Chapter 5. As measurements we used a combination of well-distributed time series in the deep ocean from the FES2014 dataset and tide gauge data in shallow waters. Chapter 5 also reports that estimation of more parameters (bathymetry and bottom friction coefficient together) with more observations gives better results than only estimating the bathymetry (as in chapters 3 and 4).

Rq 2: How to define a cost function for the parameter estimation problem that gives a good fit between the model and observations and that can be optimized with a feasible computational cost?

To estimate tides, it is common to define the cost function in terms of tidal constituents, but here we use time-series as model output because this works with shorter simulations than the Rayleigh criterion that tidal constituents would allow. This makes our approach much more efficient, since simulation times are reduced from a year to a month.

Only tide representation is simulated for the estimation because, firstly, surge is less sensitive to the bathymetry and bottom friction coefficient. Secondly, surges show an irregular variability. With the long sampling interval of satellite altimeters estimation would require simulations over a very long time period. The long-term constituents SA and SSA are excluded from the experiment, because seasonal variations show a strong inter-annual variability. Experiments show that the use of time-series can reduce the computational cost while providing good updates of parameters.

To make the estimation feasible, we have to ensure that the total number of simulations remains acceptable. This number is proportional to the parameter dimension x in the cost function since the estimation algorithm starts with a perturbation to each pa-

rameter. A generally applicable method for reducing parameter dimensions is to define one correction factor per subdomain instead of estimating the parameter in every grid cell. In Chapter 3 we analyzed the global tide propagation length and selected 110 subdomains, each with a correction factor for the bathymetry. 19 subdomains for bottom friction were used in several regions with large tidal energy dissipation in Chapter 5. In total, the parameter dimension is sharply reduced from $O(10^6)$ to $O(10^2)$.

The computation time for the cost function is also affected by the number of observations used. To balance the estimation accuracy and computational complexity, we generate evenly distributed deep ocean data from the FES2014 dataset to estimate bathymetry in chapters 3 and 4. In Chapter 5, more tide gauge data are included for the shallow waters such that the bottom friction coefficient can also be effectively estimated. The observation dimension is kept within an acceptable size with the development of model order reduction in the estimation process, which will be discussed in detail in Rq3. In addition, we added some constraints to make the estimation more robust, such as defining lower and upper boundaries to constrain the changes of the parameters.

Rq 3: How can we minimize the cost function in a way that is sufficiently efficient to make the computations feasible?

In this thesis, the parameter estimation system we designed is applied to the Global Tide and Surge Model (GTSM) using an iterative least-squares estimation algorithm called DUD. The advantages of this algorithm are that it is derivative-free and it is easy to implement. For large-scale estimation, we focused on three aspects: the computational cost, memory requirement, and the estimation accuracy.

First, we developed a computational-efficient parameter estimation system in Chapter 3; The computational demands are mainly determined by two factors. One is the computational time of a single model simulation, and the other is the number of model simulations. To reduce the single model simulation time, a strategy using a coarse grid model to replace the high-resolution model is designed. We tested two variants, Coarse Calibration and Coarse Incremental Calibration. The former completely replaces the fine model with a coarser grid during the parameter estimation procedure. The latter replaces the output increments between the initial model and model with modified parameters by coarser grid model simulations. The CPU time using the coarse-to-fine approach is reduced to one-third. As an example, bathymetry is estimated with this computation-efficient system in Chapter 3, resulting in significant improvements for the model-derived tide forecast. The number of model simulations is reduced by parameter dimension reduction, which is described in Rq2.

To reduce the memory use and enable the use of more observations and longer simulation times, an estimation scheme with the Proper Orthogonal Decomposition (POD) time pattern-based model order reduction is designed in Chapter 4. Like most of the parameter estimation algorithms, DUD assimilates the measurements in one batch. The memory requirement to assimilate these measurements is proportional to the product of the number of measurement locations, the number of time steps, and the ensemble size. This can lead to a huge memory usage that is larger than that available. Therefore, to allow for longer simulation times, a memory reduction method was developed, that

is inspired by model order reduction. Traditionally, model order reduction is applied to spatial patterns of the state variables, mainly to lower the model computational complexity. In this study, we have applied a projection onto to the time patterns of the model output and observations with a truncated singular value decomposition (SVD). Experiments show that the number of measurements can be reduced from $O(10^4)$ to $O(10^2)$, i.e. by a factor of 22. The experimental results in Chapter 4 show that the memory usage can be significantly reduced with a negligible accuracy loss.

Lastly, we have designed an outer-loop iteration in Chapter 4 to improve the parameter estimation accuracy, similar to the Incremental 4D-Var. The inner-loop consists of the DUD algorithm, applied to the GTSM with a lower resolution (Approach 2 in Chapter 3). The outer-loop iteration uses the optimized parameters obtained from the inner loop to update the initial output. The initial model is simulated using the fine grid to restart the next inner-loop process. This approach provides a better agreement between the observation and GTSM with the fine grid.

These three combined developments form a feasible and computational-efficient and memory-efficient parameter estimation scheme for global tide models.

6.2 Outlook

In order to further improve the accuracy of global water-level forecasts, one can consider the refinement or improvement of the physical modeling, parameter estimation, and state variable assimilation. Here we list a few potential research topics for further investigation:

1. From the hydrodynamic modeling perspective, the influence of sea ice on the tide is currently not yet included into the model. However, the seasonal modulation from sea ice can affect the model performance (Kagan & Sofina, 2010; Müller et al., 2014). For example, Bij de Vaate et al. (2021) report that seasonal modulation of the M2 tide is observed across the Arctic with amplitude changes up to 0.25m in Hudson Bay and on the Russian shelf. Moreover, the tide dissipation rate may strongly be affected by the sea ice cover (Kagan & Sofina, 2010).

   Since the sea ice term is currently not included in GTSM, the water level representation in the arctic ocean is relatively crude because sea ice exerts additional frictional stress on the surface. In our parameter estimation experiment, we observed that in the Canadian archipelago, higher bottom friction coefficients are estimated. This is probably caused by a lack of dissipation by sea ice. However, the estimated bottom friction coefficients do not result in the proper behavior through the different seasons. A possible solution is to include the sea ice modeling in the GTSM, and the sea ice coefficient will also become an uncertain source to estimate. This will also require measurements that properly represent modulation of the tides over the seasons. Preliminary products of this type are starting to appear (Bij de Vaate et al., 2021).

2. In our parameter estimation experiment, we estimated the bottom friction coefficient in 19 subdomains. Bottom friction contributing to the European Shelf and

the Hudson Bay/Labrador areas is analyzed in detail. However, other regions, such as the North West Australian Shelf, are calibrated crudely with only 1 subdomain due to the limited number of tide gauges available and limited computational resources. In our experience, a detailed analysis of the distribution of energy dissipation and a large number of subdomains can lead to more accurate estimates. For instance, Zijl et al. (2013) generated 100 subdomains to estimate the bathymetry and bottom friction term in the European Shelf with the regional tide model DCSMv6.0, resulting in excellent improvements for water level forecasts. Besides, the bottom friction coefficient is assumed to be temporally constant for the initial model in this study but can vary continuously in space and even in temporal patterns (Wang et al., 2021). Moreover, subdomains for bathymetry can be generated in detail for shallow waters to be consistent with the bottom friction subdomains.

In addition, the limited availability of observations in coastal waters also limits the estimation accuracy. Further research can be focused on the detailed study and estimation of bottom friction near the coast and collection of more local observations.

3. Water level, the elevation of the free surface of the ocean, can be seen as the sum of the tide, surge and their interactions. In this study, the accuracy of the water level is improved because of the parameter estimation for the tide representation. This is due to the surge not being very sensitive to bathymetry, and to bottom friction. In addition, including surge in the parameter estimation is difficult.

   The main source of error in surge simulation is the meteorological forcing, including the wind and air pressure conditions varying in spatial and temporal fields. The wind stress drag coefficient is empirically defined (Charnock, 1955). Data assimilation for joint parameter and state estimation (Evensen, 2009) can be a possible research topic to improve surge simulations. One of the challenges for this large-scale assimilation system is lack of observations. Tide gauge data is not well-distributed. Satellite altimeter measurements may be able to be utilized but requires a new approach for the complex preprocessing.

Bibliography

Bij de Vaate, I., Vasulkar, A. N., Slobbe, D. C., & Verlaan, M. (2021). The influence of arctic landfast ice on seasonal modulation of the m2 tide [e2020JC016630 2020JC016630]. *Journal of Geophysical Research: Oceans*, *126*(5), e2020JC016630. https://doi.org/https://doi.org/10.1029/2020JC016630

Charnock, H. (1955). Wind-stress on a water surface. *Quarterly Journal of the Royal Meteorological Society*, *81*(350), 639–640. https://doi.org/10.1002/qj.49708135027

Evensen, G. (2009). The ensemble kalman filter for combined state and parameter estimation. *IEEE Control Systems Magazine*, *29*(3), 83–104. https://doi.org/10.1109/MCS.2009.932223

Kagan, B., & Sofina, E. (2010). Ice-induced seasonal variability of tidal constants in the arctic ocean [Tides in Marginal Seas - A special issue in memory of Prof Alexei Nekrasov]. *Continental Shelf Research*, *30*(6), 643–647. https://doi.org/https://doi.org/10.1016/j.csr.2009.05.010

Müller, M., Cherniawsky, J. Y., Foreman, M. G. G., & von Storch, J.-S. (2014). Seasonal variation of the m 2 tide. *Ocean Dynamics*, *64*(2), 159–177. https://doi.org/10.1007/s10236-013-0679-0

Wang, D., Zhang, J., & Wang, Y. P. (2021). Estimation of bottom friction coefficient in multi-constituent tidal models using the adjoint method: Temporal variations and spatial distributions [e2020JC016949 2020JC016949]. *Journal of Geophysical Research: Oceans*, *126*(5), e2020JC016949. https://doi.org/https://doi.org/10.1029/2020JC016949

Zijl, F., Verlaan, M., & Gerritsen, H. (2013). Improved water-level forecasting for the northwest european shelf and north sea through direct modelling of tide, surge and non-linear interaction. *Ocean Dynamics*, *63*(7), 823–847. https://doi.org/10.1007/s10236-013-0624-2

Acknowledgements

Now, it is time for me to say goodbye to this four-year journey at the Delft University of Technology. I sincerely thank those who have offered me encouragement and support during my PhD program.

First of all, I would like to express my sincere appreciation to my promotors Prof. Hai Xiang Lin and Prof. Martin Verlaan. Thank you, Hai Xiang, for giving me an opportunity to start my PhD in the Netherlands and for providing me with your strong support from the research and daily life in the four-year study. Many thanks to my promotor Prof. Martin Verlaan for his consistent guidance, immense knowledge, and patience. He works not only as a promotor but also as my daily supervisor.

I would like to give my most sincere thanks to Prof. A.W. Heemink, Prof.-Ing. habil R. Klees, Prof. J.D. Pietrzak, Prof. A.H. Weerts and Prof. habil.T. Janjic Pfander to be my committee members and provide me invaluable suggestions and comments.

I am particularly grateful to my colleagues currently or formerly working in the Mathematical Physics group: Jianbin Jin, Cong Xiao, Senlei Wang, Guangliang Fu, Sha Lu, Xiangrong Wang, Tuo Deng, Xiao Li, Andres Yarce Botero et al. I want to thank Evelyn Sharabi and Dorothee Engering for helping me to get out of life-related matters. I would like to thank all my colleagues in the ocean water-level data assimilation and modeling group. It was a great pleasure to work them: Cornelis Slobbe, Amey Vasulkar, Henrique Guarneri, Inger Bij de vaate, Yosra Afrasteh and Frithjof Ehlers. Many thanks to Jelmer Veenstra and Maialen Irazoqui Apecechea in Deltares for supporting me with the model development. I want to thank Avelon Gerritsma for translating my thesis summary into Dutch.

I really appreciate spending time with my Chinese friends in the Netherlands. Special thanks must go to Sihang, Hai, Yujie, Hanqing, Baozhou, Hè, Qiaochu and Naqi.

I would like to thank my supervisors when I was studying in China: Prof. Weimin Zhang and Prof. Jun Yang. Thank you for leading me to start scientific research and encouraging me to go further.

Finally, I would like to express my deepest gratitude to my family. Thanks to my parents for their never-ending love, encouragement and support throughout my life. Thanks to my pet kitten for her company in the coronavirus lockdown time.

Xiaohui Wang
October, 2021
Delft, The Netherlands

Curriculum Vitæ

Xiaohui WANG

Xiaohui Wang is a PhD student at the Mathematical Physics group of the Faculty of Electrical Engineering, Mathematics and Computer Science, Delft University of Technology, supervised by Martin Verlaan, Hai Xiang Lin. Her PhD work focuses on the improvement of global tide and storm surge forecasts with parameter estimation.

Xiaohui Wang was born in Jiangsu, China on April 28, 1993. She obtained her Bachelor degree and Master degree from National University of Defense Technology in 2015 and 2017 respectively.

List of Publications

Journals

3. **Wang, X.**, *Verlaan, M., Apecechea, M. I., and Lin, H. X (2021): Computation-efficient Parameter Estimation for a High-Resolution Global Tide and Surge Model (GTSM).*, Journal of Geophysical Research: Oceans, 126, e2020JC016917.

2. **Wang, X.**, *Verlaan, M., Apecechea, M. I., and Lin, H. X (2021): Parameter Estimation for a Global Tide and Surge Model with a Memory-efficient Order Reduction Approach.*, Ocean Modelling (revised).

1. **Wang, X.**, *Verlaan, M., Apecechea, M. I., and Lin, H. X: Parameter Estimation to Improve Coastal Accuracy in a Global Tide Model*, Ocean Sci. Discuss. https://doi.org/10.5194/os-2021-112, in review, 2021.

Conferences

4. **Xiaohui Wang**, *Martin Verlaan, and Hai Xiang Lin: Accurate parameter estimation for a Global Tide and Surge Model with Model Order Reduction*, Presented at Joint ECMWF/ OceanPredict workshop on Advances in Ocean Data Assimilation, online, 17-20 May, 2021.

3. **Wang, X.**, *Verlaan, M., and Lin, H. X: Efficient Calibration of a Global Tide and Surge Model*, EGU General Assembly 2020, Online, 4–8 May 2020, EGU2020-5446, .

2. *Verlaan, M.*, **Wang, X.**, *and Lin, H. X.: Reducing the memory requirements of parameter estimation using model order reduction*, EGU General Assembly 2020, Online, 4–8 May 2020, EGU2020-5717.

1. **Xiaohui Wang**, *Martin Verlaan, and Hai Xiang Lin: Parameter Estimation for a Global Tide and Surge Model*, Proceedings of the 8th International Conference on Water Resources and Environment Research, 14–18 June 2019, Nanjing, China.